


AN ABSTRACT OF THE THESIS OF

Sean W. Fleming for the degree of Master of Science in Geology presented on October 27, 1998.

Title: Single and Multiple Rates of Nonequilibrium Diffusive Mass Transfer at the Laboratory, Field, and Regional Scales in the Culebra Member of the Rustler Formation, New Mexico.


Redacted for Privacy

Abstract Approved: _____



Roy Haggerty

In the first phase of this study, data from eight laboratory-scale diffusion experiments performed on five samples of the Culebra (dolomite) Member of the Rustler Formation, New Mexico, are examined for evidence of variability in effective diffusion coefficients. Modeling is performed under the assumption of a lognormal distribution of D_e . The estimated standard deviation (σ_d) of $\ln(D_e)$ within each sample is found to range from 0 to 1, with most values lying between 0.5 and 1. The variability over all samples leads to a combined σ_d in the range of 0.9 to 1.2. Formation factors measured on Culebra samples are found to be well-described by a lognormal distribution with a standard deviation of approximately 0.7. As formation factor is linearly related to D_e , this implies: (1) the assumption of a lognormal distribution of D_e is appropriate; (2) our estimates of σ_d are reasonable; and (3) formation factors may provide an inexpensive means of characterizing variability in D_e . A comparison of our estimation results to other rock properties suggests that, at the lab-scale, the geometric mean of D_e increases with bulk porosity and the quantity of macroscopic features such as vugs and fractures. However, σ_d appears to be determined by variability within such macroscopic features and/or by micropore-scale heterogeneity. In addition, comparison of experiments at several spatial scales suggests that increasing sample volume results in an increase in σ_d .

In the second phase of the study, deterministic and stochastic simulations of one-dimensional advective-dispersive transport in the Culebra dolomite are performed at the field- and regional-scales using a variety of diffusive mass transfer models. Single-rate nonequilibrium mass transfer is found to result in increases in tailing and dispersion, a decrease in maximum plume concentration, and faster initial solute arrival relative to equilibrium processes. A distribution of diffusion rates greatly accentuates these phenomena, and results in nonequilibrium mass transfer under conditions for which single-rate diffusion would approach equilibrium. These effects are generally present at greatly differing time- and space-scales and under uncertainty in mass transfer and flow parameters, although for narrow distributions of D , the multirate model behaves similarly to a single-rate model at the regional-scale, attaining LEA. Scaling of mean diffusion rate coefficients with experimental time-scale may result in both extreme tailing and initial solute arrival times approaching those found for nonreactive transport, with significant implications for remediation design and waste repository risk assessment.

©Copyright by Sean W. Fleming
October 27, 1998
All Rights Reserved

Single and Multiple Rates of Nonequilibrium Diffusive Mass Transfer at the Laboratory, Field, and
Regional Scales in the Culebra Member of the Rustler Formation, New Mexico

by

Sean W. Fleming

A THESIS

submitted to

Oregon State University

in partial fulfillment of
the requirements for the
degree of

Master of Science

Presented October 27, 1998
Commencement June, 1999

Master of Science thesis of Sean W. Fleming presented on October 27, 1998

APPROVED:

Redacted for Privacy

Major Professor, representing Geology

Redacted for Privacy

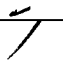
Chair of the Department of Geosciences

Redacted for Privacy

Dean of Graduate School

I understand that my thesis will become part of the permanent collection of Oregon State University libraries. My signature below authorizes release of my thesis to any reader upon request.

Redacted for Privacy

 Sean W. Fleming, Author

ACKNOWLEDGEMENTS

I wish first to thank my advisor, Roy Haggerty, for his understanding, support, and ability to explain difficult things in a way that makes them seem simple (the mark of a great educator). I would also like to express my appreciation to my professors both in Geosciences and in other departments; they have, without exception, been superb teachers. A particular thanks goes out to Goran Jovanovic, for his enthusiasm and for taking the time to explain a little about mass transfer to a geologist (a challenging task, presumably). In addition, this section would be woefully incomplete without acknowledging the very significant help provided by Lucy Meigs and Sean McKenna. Particular mention goes out to those who took the time and effort to serve on my committee: Roy Haggerty, Jack Istok, Sherm Bloomer, Lucy Meigs, and Arne Skaugset. I'd also like to thank my fellow grad students for their contributions to my mental health, particularly Mike Kelley with his vodka-blackberry smoothies (no hydrogeology group should be without a former professional bartender!).

The greatest debts of gratitude, of course, go to my mother, Alice Fleming, and to my girlfriend, Kristine Penn. And to the Big Guy in the Sky, for giving me these people and these opportunities.

And finally, like the PBS voiceover says, this program has been made possible by a grant from... the American taxpayer. This work was funded by Sandia Corporation, a Lockheed Martin company, for the United States Department of Energy under Contract DE-ACO4-94AL85000.

TABLE OF CONTENTS

	<u>Page</u>
1. INTRODUCTION	1
2. GEOLOGIC BACKGROUND	4
2.1 Mass Transfer	4
2.2 The Waste Isolation Pilot Plant (WIPP)	8
2.2.1 General	8
2.2.2 Geologic History	9
2.2.2.1 The Delaware Basin	9
2.2.2.2 The Culebra Dolomite	13
2.2.3 Multirate Mass Transfer in the Culebra Dolomite	14
3. MODELING OF STATIC DIFFUSION DATA	17
3.1 Experiment and Data	17
3.2 Mathematical and Code Development	22
3.3 Results	37
3.3.1 Parameter Estimation Statistics	37
3.3.2 Sources of Error	47
3.3.2.1 Experimental Error	47
3.3.2.2 Concentration-Dependent Diffusion	49
3.3.2.3 Multicomponent Diffusion	50
3.3.3 Single-Rate Versus Multirate Models	52
3.3.4 Comparison to Other Culebra Modeling Results	55
3.4 Discussion	61
3.4.1 Correlation of Modeling Results to Observable Geology	61
3.4.2 Development of Spatial Scaling Relationships	74
3.4.3 Suggestions for Future Laboratory-Scale Diffusion Work	81
4. REGIONAL-SCALE SIMULATIONS	83
4.1 General	83
4.2 Model Parameterization	84
4.2.1 Monte Carlo Input Distributions	84
4.2.2 Deterministic Simulations	93
4.3 Code Development	94

TABLE OF CONTENTS, CONTINUED

	<u>Page</u>
4.4 Results	98
4.5 Discussion	109
4.5.1 Deterministic Simulations	109
4.5.2 Monte Carlo Simulations	114
5. CONCLUSIONS	120
BIBLIOGRAPHY	122
APPENDICES	127
APPENDIX 1: FORTRAN77 code MRSD	128
APPENDIX 2: FORTRAN77 code STAMMT-LMC	140

LIST OF FIGURES

<u>Figure</u>	<u>Page</u>
1. Stratigraphic chart for the WIPP site	11
2. Location map and cross section	12
3. Scales and types of Culebra matrix porosity	15
4. Out-diffusion x-ray images for sample B33-H	19
5. Mass uptake and recovery data	20
6. Boundary conditions for the static diffusion experiments	23
7. Schematic illustration of pore-scale heterogeneity	26
8. Hypothetical distribution of effective diffusion coefficients	30
9. Empirical and best-fit CDFs of formation factor	33
10. Mass ratio data and model responses for B33-H	38
11. Mass ratio data and model responses for RC1-A	39
12. Mass ratio data and model responses for RC2-B	40
13. Mass ratio data and model responses for RC4-D	41
14. Mass ratio data and model responses for RC6-G	42
15. Mass ratio data and model responses for bulk diffusion	43
16. CDFs from lab- and field-scale experiments	57
17. Correlation of μ_d to degree of vugginess	62
18. Correlation of μ_d to degree of gypsum-filling	63
19. Correlation of μ_d to bulk porosity	64
20. Correlation of μ_d to degree of fracturing	65
21. Correlation of σ_d to degree of vugginess	66
22. Correlation of σ_d to degree of gypsum-filling	67

LIST OF FIGURES, CONTINUED

<u>Figure</u>	<u>Page</u>
23. Correlation of σ_d to bulk porosity	68
24. Correlation of σ_d to degree of fracturing	69
25. Correlation of σ_d to number of types of features observed	71
26. Correlations between porosity and macroscopic features	72
27. Correlation between mass transfer parameters and spatial scale of experiment	75
28. Indirectly utilized input distributions	85
29. Flow parameter input distributions	86
30. Mass transfer parameter input distributions	89
31. Flowchart delineating steps in performing Monte Carlo simulations	95
32. Arithmetic-space plots of concentration BTCs	99
33. Log-space plots of concentration BTCs	100
34. Arithmetic-space plots of mass BTCs	101
35. Log-space plots of mass BTCs	102
36. Output CDFs of C_{max} and $T_{M1\%}$, 1 m column	103
37. Output CDFs of $T_{M90\%}$ and T_{MSA} , 1 m column	104
38. Output CDFs of σ_{BTC} and S_{BTC} , 1 m column	105
39. Output CDFs of C_{max} and $T_{M1\%}$, 3000 m column	106
40. Output CDFs of $T_{M90\%}$ and T_{MSA} , 3000 m column	107
41. Output CDFs of σ_{BTC} and S_{BTC} , 3000 m column	108

LIST OF TABLES

<u>Table</u>	<u>Page</u>
1. In-diffusion results for single-rate and multirate parameter estimations	44
2. Out-diffusion results for single-rate and multirate parameter estimations	45

Single and Multiple Rates of Nonequilibrium Diffusive Mass Transfer at the Laboratory, Field, and Regional Scales in the Culebra Member of the Rustler Formation, New Mexico

1. INTRODUCTION

Accurate description of rate-limited transfer of mass from regions of advective porosity to regions dominated by diffusion and/or sorption is critical to making reliable predictions of solute transport in geologic media. Instantaneous diffusion and sorption and single rates of nonequilibrium mass transfer are well-accepted concepts in research and industry. However, recent work (e.g., *Haggerty et al., 1998; Haggerty et al., in preparation; Cunningham and Roberts, 1998*) has demonstrated that multiple mass transfer rates due to pore-scale heterogeneity may play a significant role in solute transport, particularly when longer time scales are considered or if results obtained at one time scale are applied to a longer time scale. These multirate mass transfer processes may have strong implications for aquifer remediation design and assessment of the risk associated with hazardous waste repositories.

The purpose of this study is to further our understanding of single-rate and, in particular, multirate diffusive mass transfer in the Culebra dolomite Member of the Permian Rustler Formation, the primary transport pathway of radionuclides from the Waste Isolation Pilot Plant (WIPP), a proposed nuclear waste repository in New Mexico (*Holt, 1997*). Detailed analysis of core clearly shows a multitude of scales of heterogeneity in the Culebra, interpreted to yield multiple rates of diffusive mass transfer (*Holt, 1997*). In addition, the presence of multirate mass transfer in the Culebra has been confirmed by analysis of field-scale tracer tests (*Meigs and Beauheim, in preparation; Haggerty et al., in preparation; McKenna et al., in preparation*). However, a comprehensive understanding of the linkages between observable geology at the WIPP site and mathematical descriptions of single-

rate and multirate matrix diffusion has not yet been developed, and fundamental questions regarding the scaling of mass transfer parameters across time- and space-scales remain unanswered.

Key questions addressed in this study are as follows:

- 1) How do single-rate and multirate mass transfer parameters correlate to the observable geology of the Culebra dolomite?
- 2) How do multirate mass transfer parameters scale from the laboratory-scale to the field-scale?
- 3) What might be the regional-scale effects of single-rate and multirate mass transfer as parameterized by laboratory- and field-scale studies?

These questions are addressed by:

- 1) inverse modeling of laboratory static diffusion data acquired by Sandia National Laboratories, using single-rate and multirate techniques;
- 2) interpretation of the static diffusion modeling results in terms of the observable geology of the hand specimens used in these experiments;
- 3) comparison of the static diffusion modeling results to multirate mass transfer parameters obtained at the field-scale;

4) use of one-dimensional, deterministic contaminant transport simulations to investigate the effects of a number of mass transfer regimes at the field- and regional-scales, and of temporal scaling of multirate mass transfer parameters;

5) use of one-dimensional Monte Carlo simulation techniques to investigate the effects of single-rate and multirate mass transfer at the field- and regional-scales in the presence of both spatial scaling of, and statistically described uncertainty in, mass transfer parameters.

2. GEOLOGIC BACKGROUND

2.1 Mass Transfer

Mass transfer refers to the movement of a constituent from one phase or region to another along a concentration gradient (e.g., *Welby et al., 1984*). In the context of contaminant hydrogeology, this involves transfer of solute mass from zones of advective (kinematic) porosity into diffusive porosity within the rock matrix or onto sorption sites on the surface of the matrix during advective-dispersive transport. This phenomenon has two well-recognized and significant implications for contaminant transport. First, transport of solute away from its source is continuously slowed through time as mass is removed from advective pathways (e.g., *Roberts et al., 1986; Quinodoz and Vallochi, 1993*). This effect partly determines how far and how fast a solute may be transported from its source, and is particularly important to evaluation of the environmental risk incurred in the event of a breaching of a nuclear waste repository. Secondly, remediation of a contaminated aquifer by pump-and-treat, soil vapor extraction, and bioremediation techniques is slowed if transfer of mass back from immobile zones to advective porosity is rate-limited (*Steinberg et al., 1987; Goltz and Oxley, 1991; Gierke et al., 1992; Armstrong et al., 1994; Fry and Istok, 1994; Harmsen et al., 1994; Harvey et al., 1994; Rabideau and Miller, 1994; Haggerty and Gorelick, 1995*). The process manifests itself as tailing and rebound effects in observed concentrations at the pumping well. Diffusive mass transfer processes in geologic media also have implications to petroleum migration (e.g., *Mann, 1994*), evaluation of residual oil saturation in hydrocarbon reservoir studies (e.g., *Tomich et al., 1973; Deans and Carlisle, 1986*), determination of $^{40}\text{Ar}/^{39}\text{Ar}$ cooling histories in geochronology studies (*Lovera et al., 1989; Lovera et al., 1993*), and evaluation of the relationship between fluid and melt inclusions and magma chemistry (*Qin et al., 1992*).

Instantaneous or equilibrium mass transfer refers to mass transfer that is very fast relative to the observation time-scale (e.g., the duration of a column experiment or tracer test). This condition

is known as the local equilibrium assumption (LEA). The Damkohler Type I number (DaI), a measure of the time-scale of exposure of a rock matrix to solute relative to the time-scale at which sorption or matrix diffusion occurs, is commonly used to assess the importance of mass transfer (see *Bahr and Rubin, 1987; Goltz and Roberts, 1987; Haggerty and Gorelick, 1995; and McKenna et al., in preparation*):

$$DaI = 3 \frac{D_e}{a^2} (\beta + 1) \frac{L}{V_{pw}} \quad (\text{Eqn. 1})$$

for the case of no sorption within the advective flowpaths and layered geometry. The capacity coefficient, β , is equal to the ratio of diffusive porosity to advective porosity [-]; L is the length scale of the experiment [L]; and V_{pw} is the pore water velocity within the advective porosity [L/T]. D_e/a^2 is the diffusion rate coefficient [1/T], where a is the length of the diffusion pathway [L] and D_e is the effective or pore diffusion coefficient [L²/T], which is some fraction of the aqueous diffusion coefficient of the solute in water, D_{aq} [L²/T]. A simple expression for the effective diffusion coefficient is (e.g, *Bear, 1972*):

$$D_e = \tau D_{aq} \quad (\text{Eqn. 2})$$

where τ , the tortuosity [-], is defined as l/l_s , where l is the straight-line distance from one end of the pore to the other [L] and l_s is the actual length along the winding pore [L]; $l/l_s < 1$. D_e may be reduced if sorption occurs within the pore, or if restrictivity is significant (i.e., if the pore radius is similar to the ionic or molecular radius of the solute; e.g., *Satterfield et al., 1973*).

For DaI greater than about 100, the rate of mass transfer is sufficiently high that it may be considered instantaneous. An upper limit on the observable rate of matrix diffusion is therefore:

$$\left(\frac{D_e}{a^2}\right)_{\max} = \frac{100V_{pw}}{3L(\beta + 1)} \sim \frac{100}{3T(\beta + 1)} \quad (\text{Eqn. 3})$$

where T is the time-scale of the experiment. The effects of mass transfer may then be described by a retardation factor which simply scales down the advective velocity of solute transport.

If DaI is less than approximately 0.01, the characteristic time-scale of mass transfer is sufficiently slow relative to the time scale of the experiment that it cannot be observed. A lower limit on the measurable rate of matrix diffusion is:

$$\left(\frac{D_e}{a^2}\right)_{\min} = \frac{0.01V_{pw}}{3L(\beta + 1)} \sim \frac{0.01}{3T(\beta + 1)} \quad (\text{Eqn. 4})$$

Rate-limited or nonequilibrium mass transfer is non-negligible for $0.01 < DaI < 100$. In this case, the time-scale of mass transfer is comparable to the time-scale of the experiment. Its effects, therefore, are significant but cannot be simplified through the use of a retardation factor, and the detailed physics of the mass transfer process must be incorporated into the model of contaminant transport. This requires a coupled system of differential equations and (in general) additional physical parameters, complicating computation and interpretation significantly.

A simplifying assumption made in most treatments of nonequilibrium mass transfer to date is that a single rate of sorption or diffusion is present. The physical meaning of this assumption is that the rock matrix is homogeneous. However, a natural rock matrix (and even many manufactured materials) is not homogenous at the microscopic scales at which mass transfer processes operate. This pore-scale heterogeneity in aquifer characteristics may, in general, be due to: (1) spatial variation in mineralogy (*Pignatello, 1990; Wood et al., 1990; Ball and Roberts, 1991a,b; Barber et al., 1992*); (2) the geometry and chemistry of coatings on the surfaces of aquifer particles (*Weber et al., 1991; Barber et al.,*

1992); (3) the volume, size, and geometry of macroporosity or microporosity in aquifer particles and aggregates of particles (Rao *et al.*, 1980; Pignatello, 1990; Wood *et al.*, 1990; Ball and Roberts, 1991a,b; Harmon *et al.*, 1992; Harmon and Roberts, 1994); (4) the external and internal geometry of small clay lenses or other low-permeability material, and the proportions of this material (Shackelford, 1991; Wilson, 1995); (5) the quantity and distribution of organic material (Karickhoff, 1984; Grathwohl, 1990; Barber *et al.*, 1992); and (6) the chemistry of the water and solute (Curtis *et al.*, 1986; Brusseau and Rao, 1989a; Weber *et al.*, 1991). As these factors control rates of sorption and matrix diffusion, and as they are heterogeneous at the pore scale, mass transfer rates should also be heterogeneous at the pore scale. That is, in a given volume of rock, many rates of mass transfer are generally present, and multirate mass transfer should thus be invoked to adequately describe solute transport within that medium (see Wu and Gschwend, 1988; Haggerty and Gorelick, 1995). Haggerty and Gorelick (1995) show how the conventional one-dimensional advection-dispersion equation may be re-written to incorporate multirate mass transfer.

The effects of multirate mass transfer have been observed in column experiments (e.g., Haggerty and Gorelick, 1998) and in integrated and comprehensive studies of the transport properties of the Culebra dolomite at the WIPP site, the study area of this thesis. Detailed analysis of core clearly shows a multitude of scales of heterogeneity in the Culebra, interpreted to yield multiple rates of diffusive mass transfer (Holt, 1997). Analysis of single-well injection-withdrawal (SWIW) and two-well tracer tests in the Culebra with long pumping durations (up to ~1100 hours) and high concentration measurement accuracy have confirmed the field-scale effects of the multirate matrix diffusion process (Meigs and Beauheim, *in preparation*; Haggerty *et al.*, *in preparation*; McKenna *et al.*, *in preparation*).

It is important to note that because it incorporates information about the time-scale of the experiment, the value of DaI for a short-duration, laboratory-scale tracer test, for example, may be

significantly different from that for a longer-duration, field-scale tracer test or remediation design. If multiple rates of mass transfer are present, the values of the mass transfer parameters estimated from the shorter-duration test - regardless of whether we choose to interpret the data using a single-rate or multirate model - may not be appropriate for use in the longer-duration remediation design (e.g., *Haggerty and Harvey, 1997; Cunningham and Roberts, 1998*).

2.2 The Waste Isolation Pilot Plant (WIPP)

2.2.1 General

The WIPP is a proposed repository for defense-generated transuranics located about 20 miles northeast of Carlsbad, New Mexico. Plans call for the repository to be placed approximately 655 m below ground surface in the Salado Formation, which is an interbedded Permian sequence of extremely low-permeability halite, anhydrite, polyanhydrite, dolomite, and clay. The repository, which is scheduled to begin operations in the near future with recertification every 5 years, consists of a series of drifts within the Salado into which drums of waste will be placed. When full, a given drift will be sealed off from the rest of the mine and the evaporites will flow inward under lithostatic pressure to form an impermeable seal about the waste. More complete descriptions of the WIPP are given in *Holt and Powers (1988)*, *Beauheim and Holt (1990)*, *Holt (1997)*, and *Meigs and Beauheim (in preparation)*.

One risk associated with the WIPP is the possibility that at some time in the future, the repository will be breached by human activity. For example, hydrocarbon deposits exist in the vicinity of the WIPP; it is conceivable that some future generation, unaware of the presence of the repository, might penetrate the WIPP while drilling for oil or gas. Radionuclides could then travel some distance up the borehole and into an overlying formation. If that formation is both conductive

and laterally extensive, it could provide a mechanism for transport of contaminants beyond the regulatory boundary of the site.

The Culebra Member of the Rustler Formation, an approximately 7 m thick dolomite which overlies the Salado Formation, has generally large transmissivities (about $<1 \times 10^{-7}$ to $>1 \times 10^{-3}$ m²/s; *LaVenne et al., 1990*) and covers an area of greater than 25,000 km², far larger than the WIPP site (*Holt, 1997*). Most flow is believed to occur in the lowermost 4.4 m (see *Meigs and Beauheim, in preparation*). The Culebra is considered to be the most transmissive laterally continuous hydrogeologic unit in the WIPP area and the most likely pathway of radionuclide transport from the repository in the event of human intrusion (*Holt, 1997; Meigs and Beauheim, in preparation*). It has, therefore, been the focus of much of the hydrogeologic work completed at the WIPP site.

2.2.2 Geologic History

The following summary is taken from reviews by *Holt (1997)*, *Jones et al. (1992)*, and *Hanford (1991)* unless otherwise noted. The reader is referred to these publications for further details and for references to original works regarding the geology of the Delaware Basin, the WIPP site, and the Culebra dolomite.

2.2.2.1 The Delaware Basin

The Delaware Basin was one of three early Permian, relatively deep marine basins in southeastern New Mexico and west Texas collectively known as the Permian Basin. The Delaware Basin spanned the border between New Mexico and Texas, and was bordered on the northwest by the Capitan reef complex. The limestone of the Capitan reef now forms the Guadalupe Mountains and the well-known peak of El Capitan. Behind the reef lay a shallow, sheltered carbonate platform.

The Delaware Mountain Group, which includes the Brush Canyon, Cherry Canyon, and Bell Canyon Formations (Figures 1 and 2), is an early Permian sequence of fine-grained clastic rocks and represents the fore-reef facies of the Capitan reef. In late Permian time, the Delaware Basin was quickly (over a period of perhaps 200,000 years) largely filled by the evaporites (principally halite and anhydrite) of the Castille Formation. Transformation of the deep marine basin into a shallow platform salina presumably required a dramatic lowering of relative sea level, followed by a progressive overall rise to permit continuing deposition of about 600 m of evaporites.

The Castille Formation is overlain by the evaporites of the Salado Formation. The Salado was deposited in a similar environment to that of the Castille, and consists principally of thick halite beds. Deposition of the Salado completed the infilling of the Delaware Basin, and extended to the northwest to overlap the Capitan limestone and the shallow platform that lay behind the reef. Overlying the Salado are the evaporites of the Rustler Formation, which are subdivided into five members: an unnamed lower member consisting of siltstone overlain by bedded halite, siltstone, and anhydrite; the Culebra Member, discussed below; the Tamarisk Member, consisting primarily of anhydrite; the Magenta Dolomite Member; and the Forty-Niner Member, which is similar to the Tamarisk.

The Rustler Formation is overlain by the interbedded siltstones and sandstones of the Dewey Lake Red Beds, which form the uppermost part of the Permian section. In the eastern portion of the WIPP site, the Dewey Lake Red Beds are unconformably overlain by Triassic fluvial, deltaic, and lacustrine deposits collectively known as the Dockum Group. Deposition of the Permian Dewey Lake Red Beds and, where present, the Triassic Dockum Group was followed by a very long period of non-deposition and/or erosion. Only Quaternary sediments overlie these rocks. The Quaternary deposits consist of the sandstones and conglomerates of the early to middle Pleistocene Gatuna Formation, the middle to late Pleistocene Mescalero Caliche, and Holocene surficial deposits.

System	Series	Age (Ma)	Depth (m)	Group	Formation
Quaternary	Holocene	0.01	75		surficial deposits
	Pleistocene				Mescalero Caliche
		1.6			Gatuna
Triassic		208			
Permian	Ochoan	245		Dokum	undivided
			175		Dewey Lake Red Beds
			275		Rustler
					Salado
		850		Castile	
	Guadalupian	270?	1350	Delaware Mountain	Bell Canyon
				Cherry Canyon	
				Brushy Canyon	

Figure 1: Stratigraphic chart for the WIPP site (adapted from Jones *et al.*, 1992).

Figure 2.a

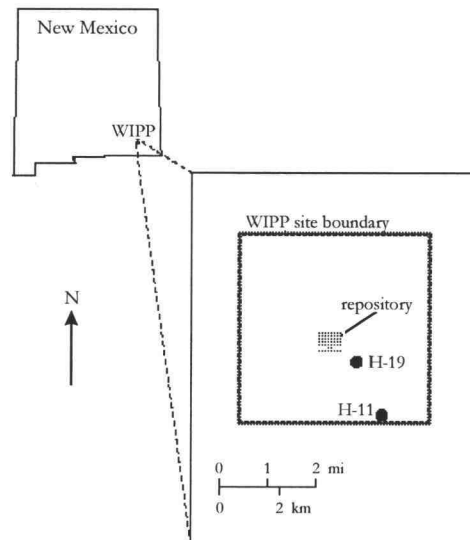


Figure 2.b

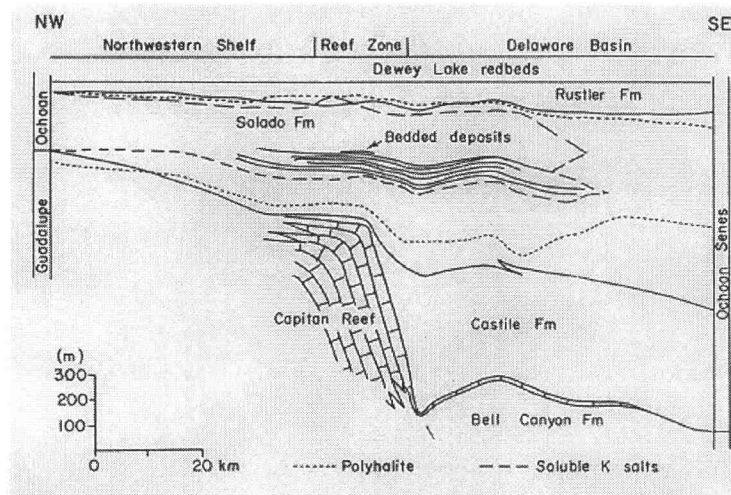


Figure 2: Location map and cross section. Figure 2.a: Map giving location of the WIPP site. H-19 is the hydro pad (suite of wells) from which samples used in the static diffusion experiments were retrieved. Field-scale tracer tests have previously been conducted at hydro pads H-11 and H-19. Figure 2.b: Geologic cross section in the vicinity of the WIPP site (from Kyle, 1991).

2.2.2.2 *The Culebra Dolomite*

The Culebra Member of the Rustler Formation consists primarily of evaporitic dolomite deposited in a lagoonal environment formed when marine waters transgressed over pre-existing salt-pan and saline-mudflat sediments. As the Culebra was deposited, the sediments immediately beneath it were dissolved and reworked. Consequently, this substrate was mechanically unstable and underwent frequent gravitational shifting and slumping, causing shearing, disruption, and deformation of the lower portion of the Culebra. The lower Culebra is also characterized by bioturbation. The upper portion of the Culebra was deposited following stabilization of the substrate, and formed planar, undisrupted strata. Deposition of the upper Culebra also coincided with a decrease in water depth of the lagoon, resulting in salinities too high to support organisms, and bioturbation ceased. Eventually, lagoon salinity increased to the point of gypsum saturation. Formation of the Culebra dolomite ended and deposition of overlying gypsum beds was initiated.

Pore water within the Culebra reached gypsum saturation as well, resulting in precipitation of gypsum nodules and cements. Depth of the lagoon continued to decrease and its salinity, and that of pore water within the Culebra, thus increased further until halite saturation was achieved. At these concentrations, anhydrite is more stable than gypsum and gypsum cement and nodules were partially replaced by anhydrite. A halite cement may also have been precipitated, but this has not been confirmed. In spite of the variety of cements, not all of the Culebra was well-indurated.

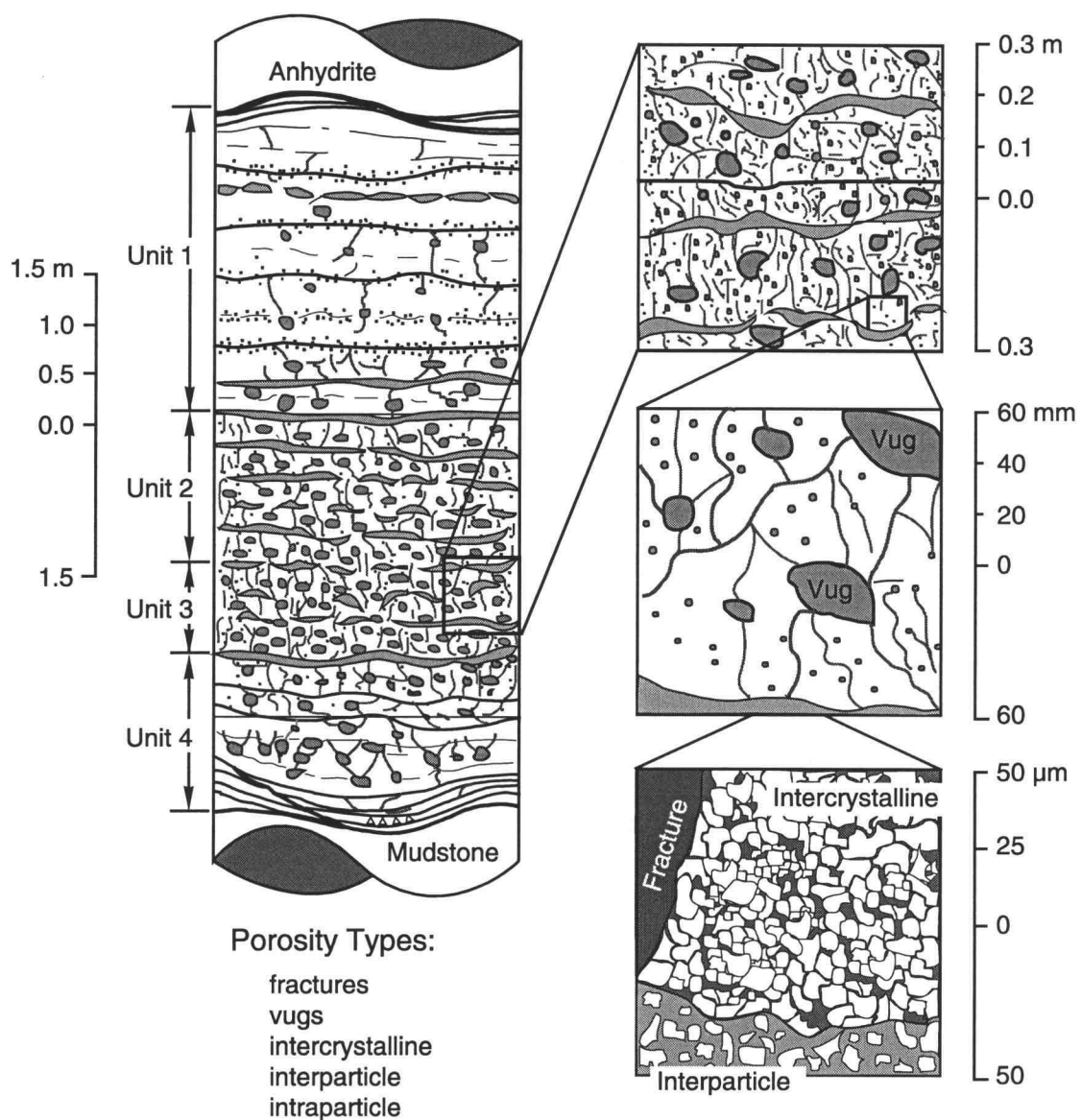
Overburden continued to accumulate, and by the end of the Cretaceous the Culebra may have been buried beneath up to 800 m of sediments. However, a large anticline formed to the north of the WIPP site, probably during the Cretaceous, and the western edge of the Delaware Basin as a whole was uplifted by the middle Tertiary. These uplift events had a number of important effects upon the Culebra dolomite.

Unloading of the Culebra through erosional removal of much of the overburden (the Culebra currently lies no deeper than about 250 m at the WIPP site) resulted in stress-release fracturing. The upper part of the Culebra was deposited in well-defined bedding planes; fracturing followed the principal zones of weakness formed by these planar interfaces. The lower Culebra, in contrast, was mechanically heterogeneous due to syndepositional deformation and bioturbation. As a result, this lower portion is characterized by shorter, more distributed fractures.

Moreover, uplift and erosion exposed both the Culebra and the highly soluble halite and anhydrite of the underlying Salado formation to meteoric waters. Exposure of the Culebra to meteoric waters first resulted in re-conversion of anhydrite to gypsum, and then partially removed this gypsum to reopen pre-existing fractures and vugs which had been filled by sulfate mineral cements and nodules. Some of the resulting open vugs collapsed under lithostatic pressure, reducing vuggy porosity but increasing the already substantial degree of fracturing in the Culebra. In addition, where the Salado underwent substantial dissolution (beyond what are now the regulatory boundaries of the WIPP), the Culebra suffered partial collapse into these karst features, resulting in brecciation.

2.2.3 Multirate Mass Transfer in the Culebra Dolomite

Due to a complex history of deposition, diagenesis, and fracturing, the Culebra dolomite is characterized by a high degree of heterogeneity (Figure 3). Multiple scales of fracturing have been observed in core (*Holt and Powers, 1988; Beauheim and Holt, 1990*), along with spatially variable degrees of vuggy porosity and gypsum-filling of vugs and fractures; poorly cemented, silt-size dolomite interbeds are also common (*Holt, 1997*). The presence of multirate diffusive mass transfer has been inferred from this observed pore- and larger-scale heterogeneity (*Holt, 1997*), and its effects have been confirmed by field-scale tracer tests (see Section 2.1). In addition to the potential plume-slowng effects of matrix diffusion, work done to date suggests that sorption of radionuclides to the



TRI-6115-514-0

Figure 3: Scales and types of Culebra matrix porosity (from Holt, 1997).

Culebra matrix is strong and would result in partial removal of solute from advective transport pathways (e.g., *Lucero et al., 1998*).

3. MODELING OF STATIC DIFFUSION DATA

3.1 Experiment and Data

A brief summary of the static diffusion experiments conducted by researchers at Sandia National Laboratories, which constitute the primary data set for this work, is given below. The innovative x-ray imaging technique used in these experiments is fully described in *Tidwell and Glass (1994)*, and details of the experimental set up and results are given in *Christian-Freear et al. (1997)* and *Tidwell et al. (in preparation)*.

Five small (approximately 6 cm by 4 cm by 2.5 cm) rectangular blocks of Culebra core retrieved from the H-19 b4 and H-19 b7 boreholes at the WIPP site were selected for the diffusion experiments to represent a distinctive suite of Culebra matrix porosity types (see Sections 2.2.2.2 and 2.2.3). Each block was attached to a tracer reservoir at one end and sealed along its other edges to form no-flux boundaries. The tracer consisted of a 0.79 molar solution of potassium iodide (KI) dissolved in a 0.8 molar solution of sodium chloride (NaCl). The iodide ion was selected due to its x-ray absorption qualities, and the NaCl solution was used to simulate naturally-occurring Culebra pore fluids (brine). Each block was initially saturated with 0.8 molar brine solution. Tracer was then allowed to diffuse from the reservoir into the block for approximately 1000 hours (in-diffusion). At the end of the in-diffusion experiment, a head gradient was established across the block and tracer was forced across it to attain saturation (i.e., until the KI concentration within the pore space was equal to that in the reservoir). After the blocks were fully saturated with the iodide tracer, the reservoir fluid was replaced with pure NaCl solution, and the tracer within the block was permitted to diffuse out into the reservoir (out-diffusion). The out-diffusion experiment was of longer duration than the in-diffusion phase (approximately 3000 hours).

X-ray images of each block were taken at intervals during the in- and out-diffusion experiments, including under fully KI-saturated and fully KI-unsaturated conditions. As the presence of the iodide ion alters the amount of x-ray energy transmitted through the sample, these images provide maps of KI concentration in the rock as a function of time. After development, the x-ray films were digitized and underwent a number of processing steps. The digital images of x-ray film density were converted using linear x-ray absorption theory into maps of normalized solute concentration within the block. An example of such an image is given in Figure 4. The spatial distribution of porosity within each block was determined using images of tracerless and tracer-saturated samples. These porosity maps were then combined with the images of normalized concentration at intermediate times to provide the data set used in our modeling: total mass diffused into or out of each block as a function of time, normalized by the total solute mass that the block can hold given the concentration of tracer within the reservoir (i.e., the initial mass for out-diffusion or the mass at infinite time for in-diffusion). These data are illustrated in Figure 5. A method for estimating measurement error in the concentration and mass data obtained using the x-ray imaging technique has not yet been developed. It is important to note that a fundamental advantage of the technique over conventional through-diffusion approaches is that it permits measurement of mass uptake into dead-end pores open only to the reservoir.

A number of difficulties were encountered during the course of the experiments. Tracer concentration in the reservoir was accidentally varied during the earliest phases of the in-diffusion study, requiring that our analysis make use of a time-dependent input boundary concentration (see Section 3.2). Sufficient dissolution of pore-filling gypsum in sample RC6-G occurred during the in-diffusion phase that its porosity was significantly increased; this block was omitted from the out-diffusion experiment. Significant gypsum dissolution probably also took place in sample B33-H, but this may have occurred while it was being saturated with KI tracer in preparation for the out-diffusion phase (*V. Tidwell, personal communication, 1998*). If so, the in-diffusion data for B33-H should

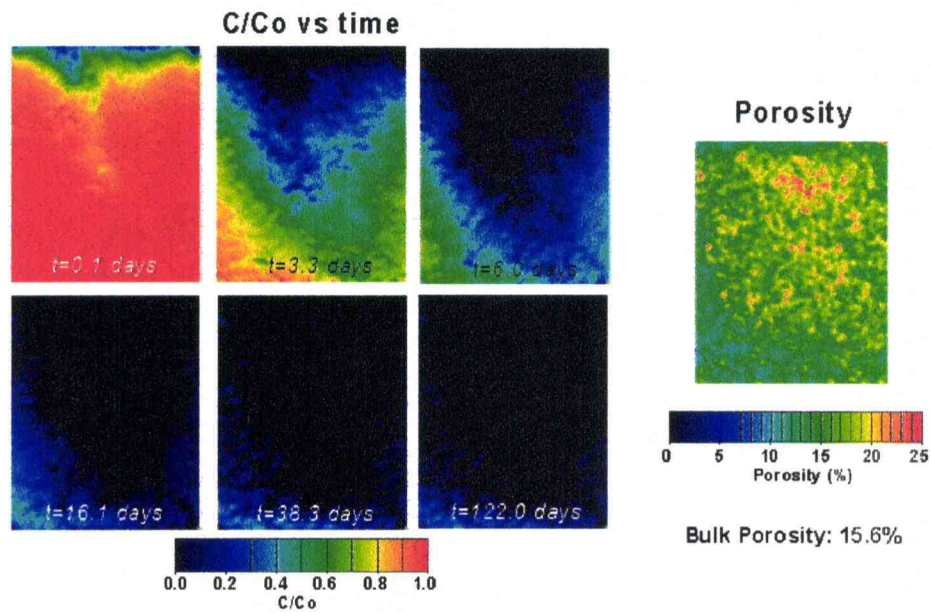


Figure 4: Out-diffusion x-ray images for sample B33-H. The image provides a map of normalized concentration within a slab of Culebra dolomite at 6 times. A reservoir of tracer-free brine is located at the top of the slab in these figures; tracer is diffusing out of the iodide-saturated block toward the reservoir. The spatial distribution of porosity within the block is given at the right. Interparticle and vug porosity predominate, with minor fracture porosity. Some vugs are gypsum-filled. Spatial resolution is about 0.0625 mm^2 . The image illustrates that the sample is heterogeneous, and solute diffuses into different regions of the rock at different rates. Maps of solute concentration generated using the x-ray imaging technique for other samples also clearly show multirate diffusion. Data provided by *V. Tidwell*; see *Christian-Freear et al. (1997)* and *Tidwell et al. (in preparation)*.

Figure 5.a

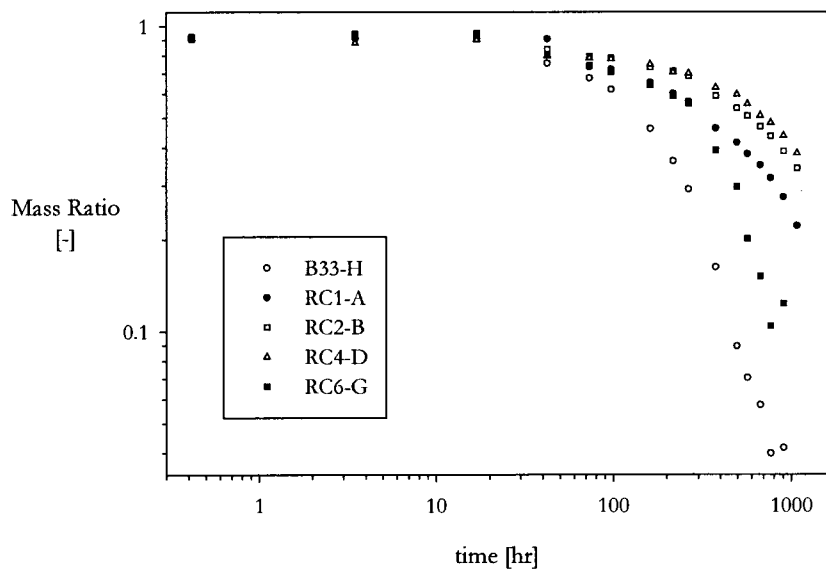


Figure 5.b

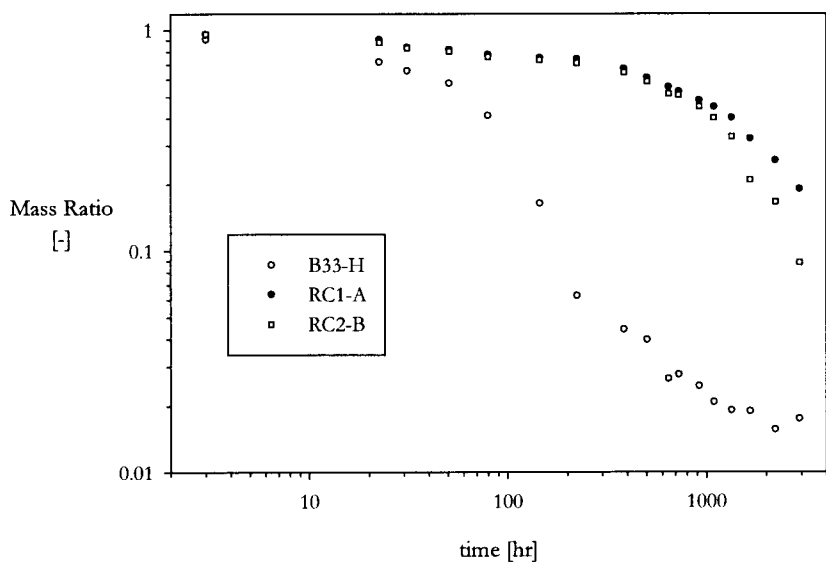


Figure 5: Mass uptake and recovery data. Figure 5.a: in-diffusion. Vertical axis gives the value of $1 - M(t)/M(t=\infty)$; see Section 3.2. Figure 5.b: out-diffusion. Vertical axis gives $M(t)/M(t=0)$. Out-diffusion experiments were not conducted for samples RC4-D and RC6-G.

be unaffected by gypsum dissolution. It proved impossible to fully saturate sample RC4-D with tracer, so it was also omitted from the out-diffusion phase.

In addition to examining each data set separately, we combined the data from the individual samples for each phase of the experiment to form bulk in- and out-diffusion data sets. This was done in such a manner that the bulk data are what would be obtained experimentally if all the blocks were arranged next to each other in parallel along a single reservoir, and normalized mass diffused in or out was measured for all blocks at once (i.e., through a single x-ray image of all the blocks, processed to give to total mass within all the blocks). The bulk mass ratio curve is the weighted arithmetic mean of the individual mass ratio curves, and is given for the example of in-diffusion:

$$\frac{M_b(t)}{M_b(t=\infty)} = \frac{\sum_{i=1}^n \frac{M_i(t)}{M_i(t=\infty)} l_i \frac{C_i(t=\infty)}{C_{reservoir}} \theta_i}{\sum_{i=1}^n l_i \frac{C_i(t=\infty)}{C_{reservoir}} \theta_i} \quad (\text{Eqn. 5})$$

where i is an index corresponding to the particular block; n is the number of blocks (i.e., 5 for in-diffusion); l_i is the length, measured away from the reservoir, of the i^{th} block [L]; $C_i(t=\infty)/C_{reservoir}$ is the normalized, late-time concentration in the i^{th} block, equal to unity and included in the above expression only for completeness [-]; θ_i is the bulk porosity of the i^{th} block [-]; and $M_i(t)/M_i(t=\infty)$ is the normalized mass [-] diffused into the i^{th} block at time t (i.e., the original static diffusion mass ratio data). Note that the widths of the individual slabs do not appear in Eqn. 5, as we treat diffusion into or out of the samples as a one-dimensional problem; this implicitly assumes that all samples have equal widths, which is approximately true. Use of the bulk diffusion data sets is intended to simulate a slightly larger-scale scenario, more representative of field-scale work, in which an extended reservoir of solute (e.g., an advective flow pathway) encounters a variety of matrix types, as

represented by the different blocks of varying porosity scales and types used in the static diffusion experiments.

3.2 Mathematical and Code Development

In this section, we derive an expression describing one-dimensional multirate diffusion into or out of a rock matrix. The conceptual physical model is similar to that used in a number of previous mathematical developments (e.g., *Haggerty and Gorelick, 1995*), but the derivation presented here is original and proceeds along significantly different lines. It is worthwhile to note, however, that our final expressions describing mass uptake and recovery in the presence of a continuous distribution of effective diffusion coefficients (Eqn. 25 and Eqn. 28) are very similar in form to an expression for diffusional mass uptake in the presence of a continuous distribution of grain sizes that was presented in the chemical engineering literature over a quarter of century ago (*Ruthven and Loughlin, 1971*).

Consider a sample of Culebra dolomite of porosity, θ , bounded at $x = l$ by a reservoir of solute (potassium iodide in our case) with a time-varying concentration, $C_i(t)$, and at $x = 0$ by a no-flux boundary, and having an initial arbitrary but uniform KI concentration, C_0 . The boundary and initial conditions are shown in Figure 6.

Conventional, single-rate diffusion of KI tracer into or out of the pore space of the slab is given by the diffusion equation subject to the boundary and initial conditions stated above:

$$\frac{\partial C}{\partial t} = D_e \frac{\partial^2 C}{\partial x^2} \tag{Eqn. 6}$$

where D_e is the effective diffusion coefficient in the rock slab (Eqn. 2).

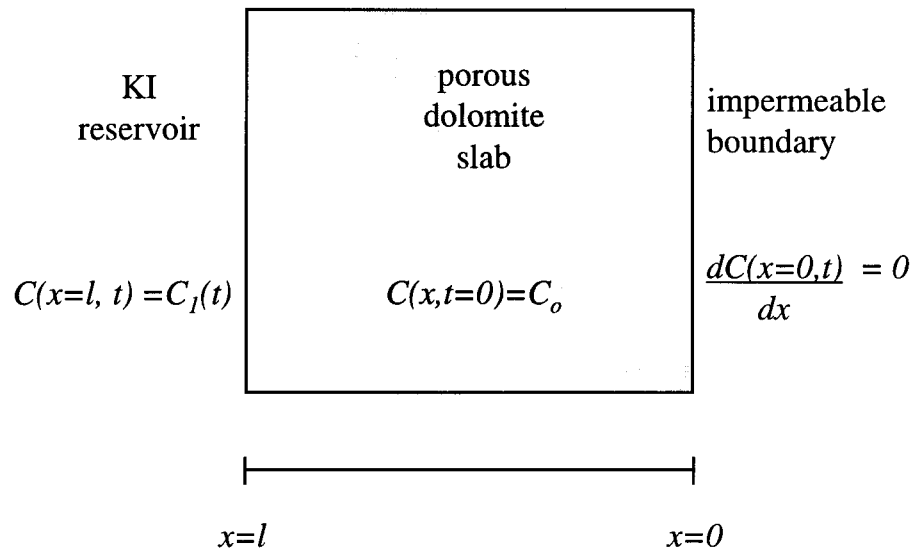


Figure 6: Boundary conditions for static diffusion experiments.

Taking the Laplace transform and rearranging, we obtain:

$$\frac{\partial^2 \bar{C}}{\partial x^2} - \frac{p}{D_e} \bar{C} = \frac{-C_0}{D_e} \quad (\text{Eqn. 7})$$

where \bar{C} is the Laplace transform of concentration within the pore space and p is the Laplace parameter. The boundary conditions are now:

$$\frac{\partial \bar{C}(x=0)}{\partial x} = 0 \quad (\text{Eqn. 8})$$

and:

$$\bar{C}(p, x=l) = \bar{C}_1(p) \quad (\text{Eqn. 9})$$

Eqn. 7 is a second order ordinary differential equation, which may be solved using the method of undetermined coefficients subject to Eqn. 8 and Eqn. 9 to obtain:

$$\bar{C}(p, x) = \left[\bar{C}_1(p) - \frac{C_0}{p} \right] \left[\frac{e^{x\sqrt{p/D_e}} + e^{-x\sqrt{p/D_e}}}{e^{l\sqrt{p/D_e}} + e^{-l\sqrt{p/D_e}}} \right] + \frac{C_0}{p} \quad (\text{Eqn. 10})$$

The 0th spatial moment of the concentration profile gives a measure of the mass, $M(t)$, within the slab at time, t :

$$M(t) = \theta A \int_{x=0}^{x=l} C(x, t) dx \quad (\text{Eqn. 11})$$

where A is the cross-sectional area of rock exposed to the solute reservoir, and which is required if $C(x, t)$ is given conventional (three-dimensional) units of mass/unit volume. Taking advantage of the

fact that the Laplace transform is a linear operator, substituting Eqn. 10 into Eqn. 11, and integrating, we obtain:

$$M(t) = (\theta A) L^{-1} \left\{ \left[\frac{\overline{C_1(p)} - \frac{C_0}{p}}{\sqrt{p/D_e}} \left[\frac{e^{l\sqrt{p/D_e}} - e^{-l\sqrt{p/D_e}}}{e^{l\sqrt{p/D_e}} + e^{-l\sqrt{p/D_e}}} \right] + \frac{C_0 l}{p} \right] \right\} \quad (\text{Eqn.12})$$

where the symbol L^{-1} indicates the inverse Laplace transform. Recognizing the definition of the hyperbolic tangent, we may rewrite Eqn. 12 as:

$$M(t, D_e) = (\theta A) L^{-1} \left\{ \left[\frac{\overline{C_1(p)} - \frac{C_0}{p}}{\sqrt{p/D_e}} \right] \text{Tanh}(l\sqrt{p/D_e}) + \frac{C_0 l}{p} \right\} \quad (\text{Eqn.13})$$

For notational convenience later in the derivation, we will define M' in the following manner:

$$M'(t, D_e) = A L^{-1} \left\{ \left[\frac{\overline{C_1(p)} - \frac{C_0}{p}}{\sqrt{p/D_e}} \right] \text{Tanh}(l\sqrt{p/D_e}) + \frac{C_0 l}{p} \right\} \quad (\text{Eqn.14})$$

Eqn. 13 may then be rewritten:

$$M(t, D_e) = \theta M'(t, D_e) \quad (\text{Eqn.15})$$

Now consider a simple model of pore-scale heterogeneity in which porosity in the rock matrix consists of N non-intersecting tubes (Figure 7). The effective diffusion coefficient within each tube (pore), $D_{e,i}$ may be different due to, at a minimum, differing tortuosities (see Section 2.1). As a result, a different mass of solute, $M_i(t)$ will have diffused into (or, equivalently, out of) each tube at a

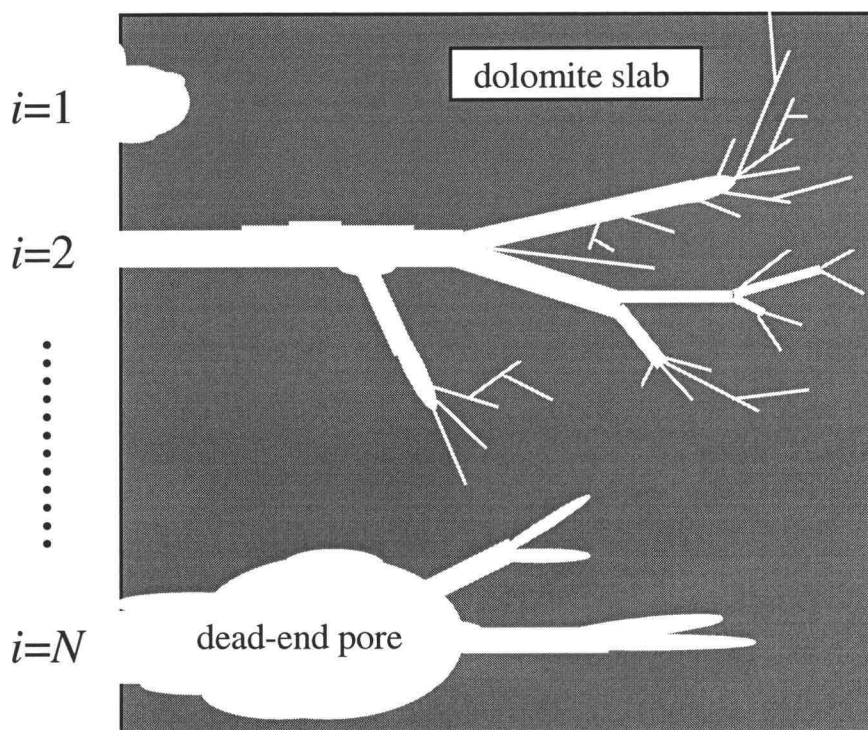


Figure 7: Schematic illustration of pore-scale heterogeneity. Heterogeneity in pore geometry gives rise to multirate diffusion. Dead-end pores are shown, but for the purpose of analyzing the lab-scale diffusion experiments any pore may completely span the sample. Pores are shown in a parallel arrangement, aligned normal to the surface of the sample. A distribution of diffusion coefficients interpreted from data under this assumption should be considered a lumped distribution, representing what may be diffusion in parallel and series in a more complex geometry (Haggerty and Gorelick, 1998). This model and our one-dimensional (in Cartesian coordinates) mathematical treatment are appropriate to interpretation of diffusion into the samples used in the static diffusion experiments, and is also representative of diffusive mass transfer into a rock matrix exposed to discrete advective pathways, such as fractures.

given time, t . That is, the i^{th} tube has a corresponding $D_{e,i}$ and $M_i(t)$. $D_{e,i=j}$ (and $M_{i=j}(t)$) may or may not be equal to $D_{e,i=k}$ (and $M_{i=k}(t)$), for $j \neq k$. As different effective diffusion coefficients have different frequencies (probabilities) of occurrence, each effective diffusion coefficient will make a different contribution to the total mass of solute diffused into the matrix.

Consider the case where there exist Z discrete values of the effective diffusion coefficient ($D_{e,j}$ for $j = 1, Z; Z \leq N$); many pores may share a particular value of D_e . Say we make many measurements of $D_{e,j}$ in many individual pores and record their frequencies (i.e., probabilities) of occurrence, N_j/N_T , where N_j is the number of pores having the j^{th} value of $D_{e,j}$ and N_T is the total number of pores in the rock. While thinking of statistical distributions of effective diffusion coefficients in terms of the probability of finding a pore with a particular geometry is more intuitive, it is ultimately both more tractable and more consistent with previous work to recast this result in terms of porosities:

$$\frac{\theta_j}{\theta_T} = \frac{V_j}{V_T} = \left(\frac{N_j}{N_T} \right) \left(\frac{V_j}{1 \text{ } j\text{-type pore}} \right) \left(\frac{N_T}{V_T} \right) \quad (\text{Eqn. 16})$$

where θ_j/θ_T is the proportion of the total porosity consisting of pores having the j^{th} value of D_e [-]; V_j/V_T is the ratio of the pore volume occupied by pores with the j^{th} D_e to the total pore volume of the rock [-]; $V_j/(1 \text{ } j\text{-type pore})$ is simply the average volume occupied by a single pore with the j^{th} D_e [L^3/pore]; and N_j/N_T is the aforementioned frequency of occurrence of pores with the j^{th} D_e [-]. For $j = 1, Z$, θ_j/θ_T therefore gives the probability mass function (PMF), $f_{d,j}$, of the discrete random variable, $D_{e,j}$, and thus describes the probability that (or frequency of) $D_e = D_{e,j}$:

$$P(D_e = D_{e,j}) = f_d(D_e) = \frac{\theta_j}{\theta_T} \quad (\text{Eqn.17})$$

Note that although capacity coefficients, strictly speaking, are not defined for a system in which only diffusion takes place and no advective porosity is therefore present, θ_j/θ_T is equal to β_j/β_T , the ratio of the capacity coefficient of the j^{th} immobile zone to the total capacity coefficient. β_j/β_T is frequently used to describe the relative contributions of different matrix diffusion rates to mass transfer in an advective transport system (e.g., *Haggerty and Gorelick, 1995*).

The total mass diffused into the pore space at a given time, t , is the sum of the masses in the N individual pores at that time:

$$M(t) = \sum_{i=1}^N M_i(t) \quad (\text{Eqn.18})$$

However, we may equally well consider $M(t)$ to be the sum of the contributions to diffusive mass uptake or release of Z classes of pores; each class of pores is characterized by its frequency of occurrence, $P(D_e = D_{e,j})$ and by a discrete effective diffusion coefficient, $D_{e,j}$. If we recognize that Eqn. 15 describes the mass diffused into the j^{th} class of pores at time t , $M_j(t)$, it may be recast as:

$$M_j(t) = \theta_j M_j'(t) \quad (\text{Eqn.19})$$

where θ_j is the porosity constituted by the j^{th} class of pores; that is, θ_j is the ratio of the volume occupied by all pores having the j^{th} value of $D_{e,j}$ to the total volume of the rock. $M_j'(t)$ is as defined in

Eqn. 14, with D_e set to the j^{th} value of $D_{e,j}$. If there are Z classes of pores, and the mass contributed by each class is given by Eqn. 19, then $M(t)$ is given by:

$$M(t) = \sum_{j=1}^Z \theta_j M_j'(t) \quad (\text{Eqn. 20})$$

Rearranging Eqn. 17 and substituting into Eqn. 20 gives:

$$M(t) = \theta_T \sum_{j=1}^Z P(D_e = D_{e,j}) M_j'(t) \quad (\text{Eqn. 21})$$

Now consider D_e to be a continuous random variable. Say we again make many measurements of D_e in many individual pores, but this time we plot up the frequencies in a histogram consisting of Z bins of width ΔD_e (Figure 8). The heavy line on Figure 8 gives a probability density function (PDF) for D_e , $f_c(D_e)$. In the case presented, the PDF is piecewise linear and consists only of vertical and horizontal segments; thus, the PDF may be represented for the time being by the discrete notation, $f_{c,j}$. In general, if D_e is a continuous random variable, the probability that it takes on a value falling within a certain (possibly very narrow) range is:

$$P(a \leq D_e \leq b) = \int_a^b f_c(D_e) dD_e \quad (\text{Eqn. 22})$$

For the case shown in Figure 8, Eqn. 22 therefore shows that the probability that D_e lies within the j^{th} bin is:

$$P(D_{e,j=k} \leq D_e \leq D_{e,j=l}) = f_{c,j=k} \Delta D_e \quad (\text{Eqn. 23})$$

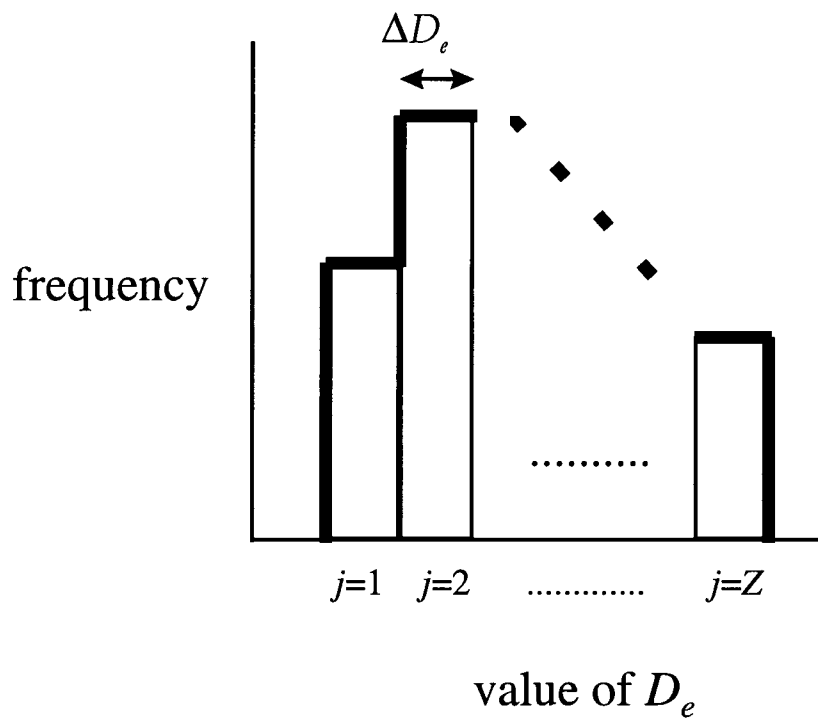


Figure 8: Hypothetical distribution of effective diffusion coefficients. Many measurements are made of D_e in many individual pores and frequencies of occurrence are plotted in the above histogram, consisting of Z bins of width ΔD_e . For the example presented, heavy line gives a PDF which is piecewise linear and consists only of vertical and horizontal segments.

where $l = k + 1$. Now substitute Eqn. 23 into Eqn. 21 to obtain the Riemann sum:

$$M(t) = \theta_T \sum_{j=1}^Z f_{c,j} M_j'(t) \Delta D_e \quad (\text{Eqn. 24})$$

If we take the limit of Eqn. 24 as Z approaches infinity, we obtain from the fundamental theorem of calculus:

$$M(t) = \theta_T \int_a^b f_c(D_e) M'(t, D_e) dD_e \quad (\text{Eqn. 25})$$

The mass diffused into a pore with effective diffusion coefficient, D_e , is now a continuous, rather than discrete, function of D_e (i.e., $M(t, D_e)$ rather than $M_j(t)$). Note that if probability is to be a dimensionless quantity, the definition of the probability of a continuous random variable (Eqn. 18) requires that the probability density function, $f_c(D_e)$, have dimensions equal to the inverse of the dimensions of the random variable, D_e . Given this fact, Eqn. 25 is dimensionally correct.

Substituting Eqn. 14 into Eqn. 25 yields:

$$M(t) = \theta_T A \int_a^b \left\{ f_c(D_e) L^{-1} \left[\left[\frac{\overline{C_1(p)} - C_0}{p} \right] \text{Tanh}(l\sqrt{p/D_e}) + \frac{C_0 l}{p} \right] dD_e \right\} \quad (\text{Eqn. 26})$$

which gives the total mass diffused into or out of the slab at time, t , in the presence of a continuous distribution of diffusion coefficients. The integration limits, a , b , represent the minimum and maximum possible values of D_e and may therefore be taken in general to be $0, \infty$.

$f_c(D_e)$ may be any continuous distribution. A number of general considerations suggest that a lognormal distribution may be appropriate (Haggerty, 1995; Haggerty and Gorelick, 1998). Discrete distributions and alternative continuous PDFs have also been used, such as gamma and piece-wise linear distributions (for discussion see Hollenbeck et al., 1998), but available formation factor data for the Culebra dolomite support the assumption of a lognormal PDF. Formation factor, a measure of the electrical properties of a rock, is commonly taken to be inversely proportional to D_e (e.g., Kelley and Saulnier, 1990). Formation factors for 21 samples of Culebra dolomite retrieved from the H-19 hydropad (a hydropad is a cluster of wells) were determined by TerraTek (TerraTek contractor's report, 1997). The samples were sourced primarily from borehole H-19 b4, from which samples for the static diffusion experiments were also obtained. An empirical CDF of these data is shown in Figure 9. Also shown is a lognormal distribution fitted by manual calibration to the data; the match is quite good. Earlier work at other locations at the WIPP site by Kelley and Saulnier (1990) also suggested that formation factors in the Culebra dolomite are lognormally distributed. Thus, there is considerable evidence that a lognormal distribution is a reasonable approximation to the true distribution of effective diffusion coefficients in the Culebra.

In practice, we normalize Eqn. 22 by the maximum possible total solute mass present in the rock, M_T . In the case of diffusion into the rock, this is the mass at $t = \infty$; for diffusion out of a saturated rock, this is the mass at $t = 0$. This maximum total mass is given by:

$$M_T = \theta_T A l C_E \quad (\text{Eqn. 27})$$

where the l is the length of the rock slab as measured perpendicular to diffusion and C_E is the concentration in the rock at $t = 0$ for diffusion out of the slab or at $t = \infty$ for diffusion into the slab.

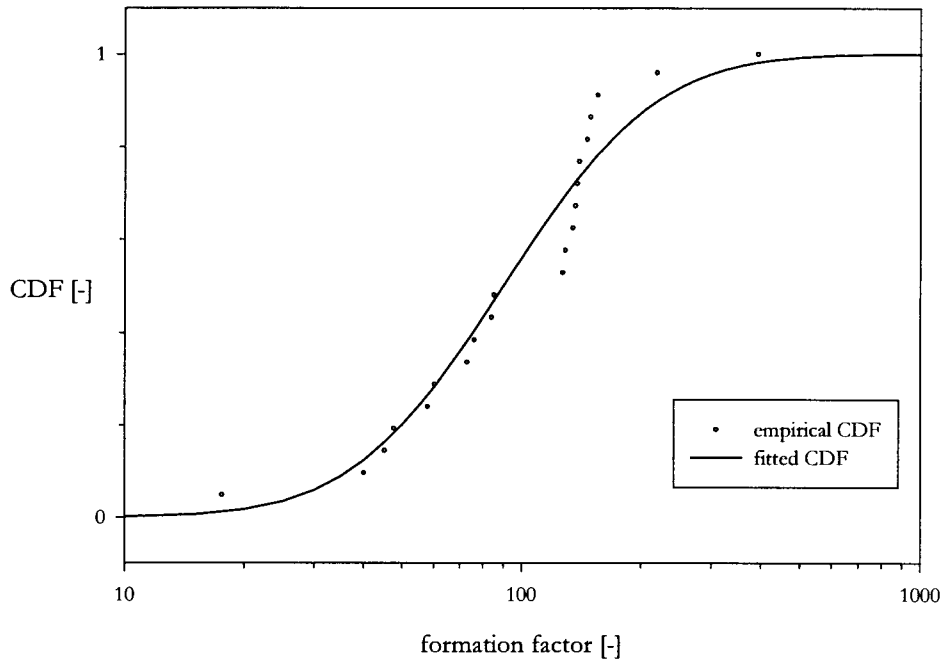


Figure 9: Empirical and best-fit CDFs of formation factor. Data is for Culebra samples analyzed by TerraTek (*TerraTek contractor's report, 1997*). Samples were taken from the H-19 hydropad, primarily borehole H-19 b4 (R. *Beaubeim, personal communication, 1997*); samples used in static diffusion experiments were taken from the same location. Best-fit lognormal CDF was determined by manual calibration and has a geometric mean of 4.5 (corresponding to a formation factor of 90) and a standard deviation of 0.7. Formation factors are inversely proportional to effective diffusion coefficients (see text), so reasonably good quality of the fit suggests that use of a lognormal distribution to approximate the true distribution of D_e in the Culebra is appropriate. Calculations of D_e from formation factors tend to be unreliable, due to the dependence of formation factor measurements on the properties of the ions present in the pore fluid and uncertainty in the precise form of the relationship between formation factor and D_e (see *Kelley and Saulnier, 1990* for discussion). However, the standard deviation of the lognormal distribution of formation factors should be a good approximation to σ_d in the distribution of D_e ; this will be further discussed in Section 3.3.4.

If normalized concentrations are used, $C_E = 1$. Making the appropriate substitution for $f_i(D_e)$ into Eqn. 26 and normalizing by Eqn. 27 gives our final expression:

$$\frac{M(t)}{M_T} = \frac{1}{l C_E} \int_a^b \left\{ \left(\frac{1}{\sqrt{2\pi D_e \sigma_d}} e^{-\frac{1}{2\sigma_d^2} [\ln(D_e) - \mu_d]^2} \right) L^{-1} \left\{ \left[\frac{C_1(p) - \frac{C_0}{p}}{\sqrt{p/D_e}} \right] \left[\text{Tanh}(l\sqrt{p/D_e}) + \frac{C_0 l}{p} \right] \right\} dD_e \right\} \quad (\text{Eqn. 28})$$

where μ_d and σ_d are the mean and standard deviation, respectively, of $\ln(D_e)$ and a and b are as discussed above.

A FORTRAN77 code (MRSD; see Appendix 1) was written to implement Eqn. 28 as a simulation and parameter estimation routine. The purpose of the code was to obtain estimates of the values of μ_d and σ_d from the diffusion data discussed in Section 3.1. Several subroutines from the IMSL (International Mathematics and Statistics Libraries) Version 3.0 package were used. These subroutines use the deHoog algorithm to numerically evaluate the inverse Laplace transform (*deHoog et al., 1982*), Gauss-Kronrod rules to perform numerical integration, and a modified Levenberg-Marquardt algorithm and a finite-difference Jacobian to solve the nonlinear least-squares optimization problem. The lower and upper limits of integration were set to the 0.0000001th and 99.9999999th percentile values of D_e , respectively, for a given μ_d and σ_d . Capability to use Eqn. 13 and Eqn. 27 to estimate a conventional, single-rate effective diffusion coefficient from the normalized mass data was also incorporated into the code. Log-space root mean square error (RMSE) was used as a measure of fit, as log-transformed data shows a greater sensitivity to the late-time, low mass ratios at which multirate effects are greatest (e.g., *Haggerty, 1995; Haggerty et al., in preparation; see also Ruthven and Loughlin, 1971*). Similar concerns led us to convert the in-diffusion mass ratio curves, which are large-valued at late times, to:

$$1 - \frac{M(t)}{M_T} \quad (\text{Eqn. 29})$$

which is small-valued at late times. When the data is then log-transformed, small relative changes in the raw late-time mass ratio data give rise to significantly larger relative changes in the converted and transformed data set. The conversion described by Eqn. 29 was also used by *Ruthven and Loughlin (1971)* for single-rate and multirate modeling of diffusive mass uptake data.

Difficulties were encountered in evaluating the hyperbolic tangent for very small times (very large values of the Laplace parameter, p). Consider, for notational simplicity, the hyperbolic tangent of a complex variable, z :

$$\text{Tanh}(z) = \frac{e^z - e^{-z}}{e^z + e^{-z}} \quad (\text{Eqn. 30})$$

By noting the following relationships:

$$z = a + ib, \quad i = \sqrt{-1}$$

$$\text{Re}(e^z) = e^a \text{Cos}(b)$$

$$\text{Im}(e^z) = e^a \text{Sin}(b)$$

$$\text{Re}(e^{-z}) = e^{-a} \text{Cos}(-b)$$

$$\text{Im}(e^{-z}) = e^{-a} \text{Sin}(-b)$$

$$\text{Cos}(-b) = \text{Cos}(b)$$

$$\text{Sin}(-b) = -\text{Sin}(b)$$

we can rewrite Eqn. 30 as:

$$\text{Tanh}(z) = \frac{e^a \text{Cos}(b) + ie^a \text{Sin}(b) - e^{-a} \text{Cos}(b) + ie^{-a} \text{Sin}(b)}{e^a \text{Cos}(b) + ie^a \text{Sin}(b) + e^{-a} \text{Cos}(b) - ie^{-a} \text{Sin}(b)} \quad (\text{Eqn. 31})$$

After some algebra, we obtain:

$$\text{Re}[\text{Tanh}(z)] = \frac{e^{2a} - e^{-2a}}{e^{2a} - e^{-2a} + 2[2\text{Cos}^2(b) - 1]} \quad (\text{Eqn. 32})$$

Note that the value of the 3rd term in the denominator of Eqn. 32 never exceeds 2. The value of the real part of the hyperbolic tangent at large z may therefore be found by omitting the terms in Eqn. 28 containing b and considering the expression's value at large a :

$$\text{Re}[\text{Tanh}(z)] \sim \frac{e^{2a}}{e^{2a}} = 1 \text{ for high values of } z \text{ and } a \quad (\text{Eqn. 33})$$

Eqn. 31 also gives:

$$\text{Im}[\text{Tanh}(z)] = \frac{2\text{Sin}(b)\text{Cos}(b)}{e^{2a} + e^{-2a} + 2[2\text{Cos}^2(b) - 1]} \quad (\text{Eqn. 34})$$

The values of both the numerator and the 3rd term in the denominator of Eqn. 34 never exceed 2. The value of the imaginary part of the hyperbolic tangent at large z is therefore its value at large a , neglecting the terms in Eqn. 30 containing b :

$$\text{Im}[\text{Tanh}(z)] \sim \frac{1}{e^{2a}} = 0 \text{ for high values of } z \text{ and } a \quad (\text{Eqn. 35})$$

For large values of the Laplace parameter, p , the value of the hyperbolic tangent in Eqn. 28 may thus be set to [1,0]. Eqn. 33 and Eqn. 35 are valid for values of a in excess of approximately 21, but the precise value depends on the value of b . The critical combinations of a , b are difficult to specify in a straightforward manner conducive to computer coding due to the periodic nature of the dependence of $Tanh(z)$ on b . In practice, the hyperbolic tangent is set to [1,0] when the function to evaluate the hyperbolic tangent returns the value NaN (Not a Number).

3.3 Results

Log-space plots of mass ratio data and best-fit curves calculated using both single-rate and multirate models (see Section 3.2) are given in Figures 10 through 15. Tables 1 and 2 summarize the results, giving the best-fit value of the effective diffusion coefficient, D_e , for each sample and for bulk diffusion (see Section 3.1) obtained using a single-rate model, as well as the corresponding best-fit multirate parameters. As discussed in Section 3.2, a lognormal distribution of effective diffusion coefficients was used in the multirate model, which is parameterized by a geometric mean, μ_d , and a standard deviation, σ_d . A larger value of μ_d indicates faster diffusion, on average, for a given block length and a larger value of σ_d indicates that a wider range of diffusion coefficients is present (i.e., that multirate effects are more significant). Log-space RMSE between the data and mass ratio curves calculated using the best-fit single-rate and multirate parameters are also given in Tables 1 and 2.

3.3.1 Parameter Estimation Statistics

Confidence limits are provided in Tables 1 and 2 for the fitted parameters. This type of information is a very useful statistical estimate of the reliability of the modeling results, and is the primary advantage of using formal parameter estimation techniques as opposed to conventional manual calibration of the model to the data.

Figure 10.a

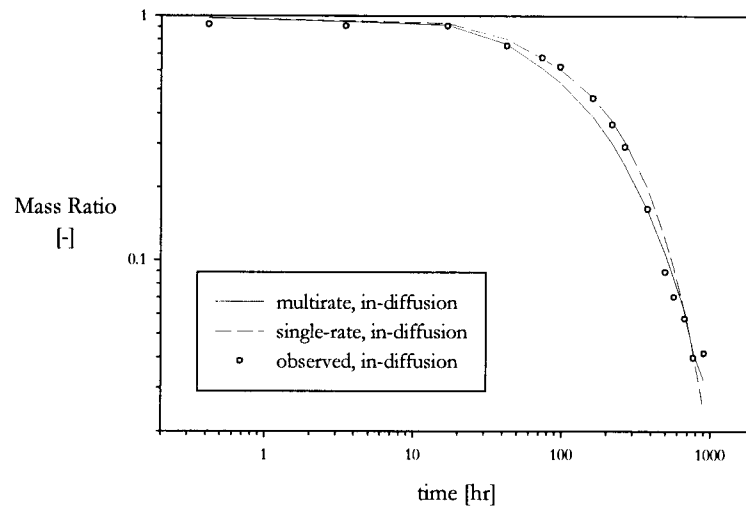


Figure 10.b

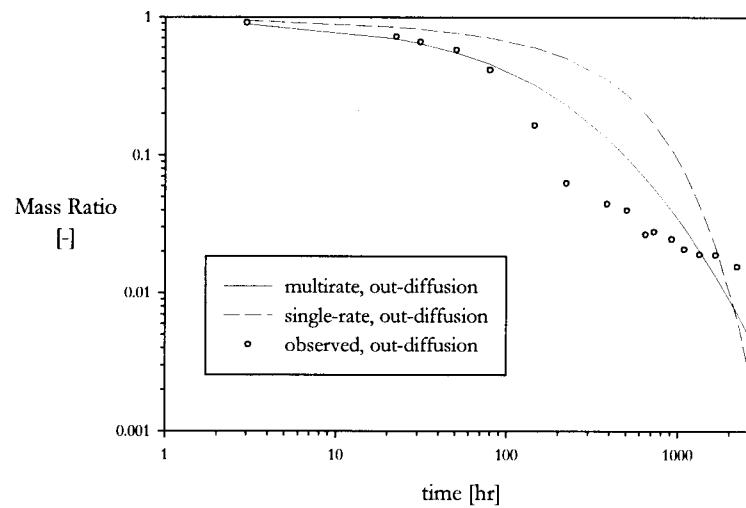


Figure 10: Mass ratio data and model responses for B33-H. Best-fit curves were calculated using a conventional single effective diffusion coefficient and a lognormal distribution of effective diffusion coefficients, for both in-diffusion and out-diffusion experiments. Figure 10.a: in-diffusion. Vertical axis gives the value of $1-M(t)/M(t=\infty)$; see Section 3.2. Figure 10.b: out-diffusion. Vertical axis is $M(t)/M(t=0)$.

Figure 11.a

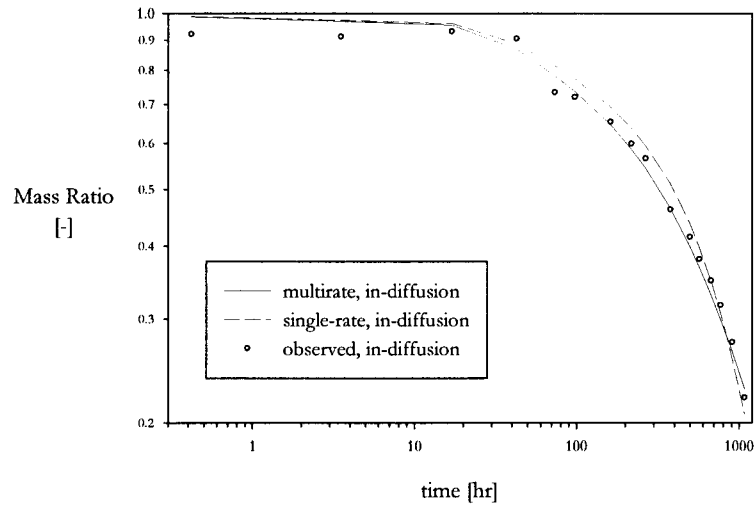


Figure 11.b

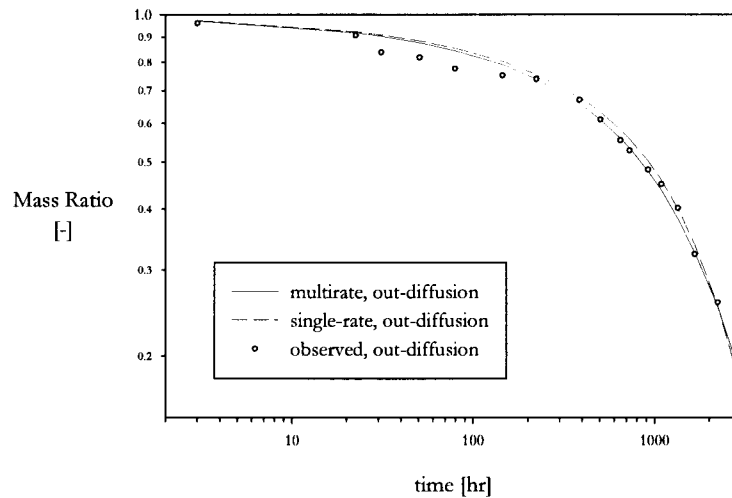


Figure 11: Mass ratio data and model responses for RC1-A. Best-fit curves were calculated using a conventional single effective diffusion coefficient and a lognormal distribution of effective diffusion coefficients, for both in-diffusion and out-diffusion experiments. Figure 11.a: in-diffusion. Vertical axis gives the value of $1 - M(t)/M(t=\infty)$; see Section 3.2. Figure 11.b: out-diffusion. Vertical axis is $M(t)/M(t=0)$.

Figure 12.a

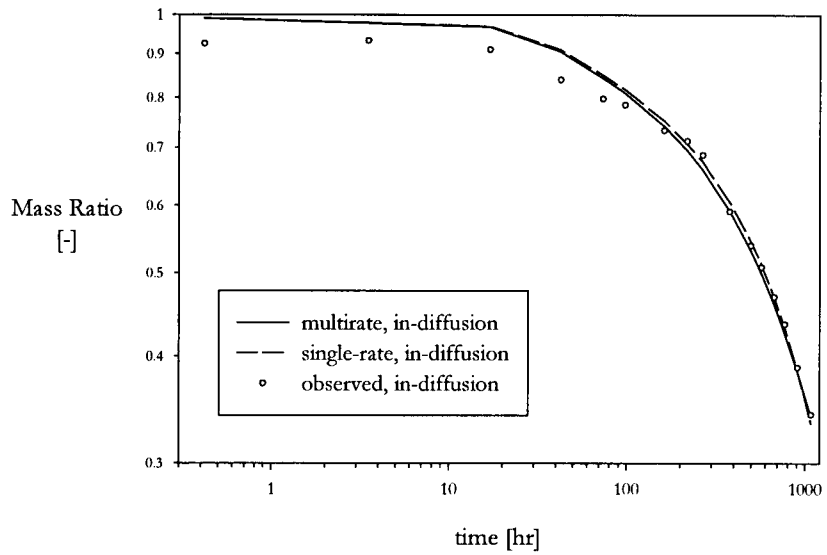


Figure 12.b

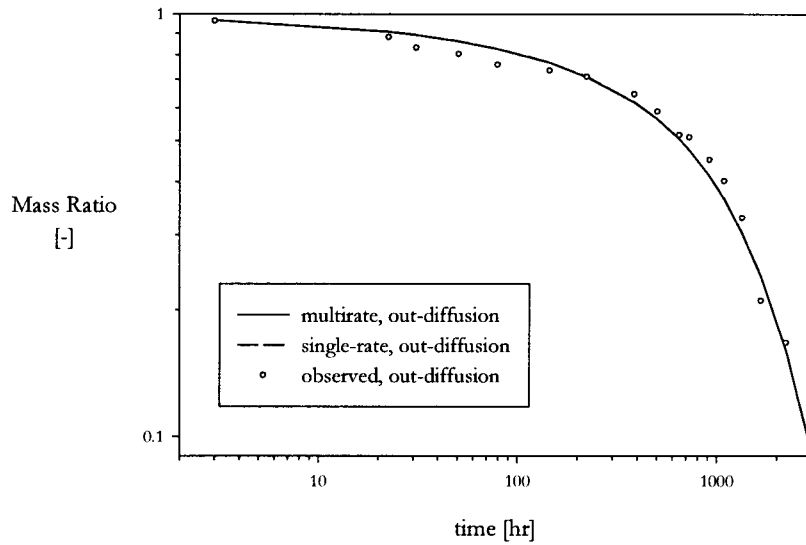


Figure 12: Mass ratio data and model responses for RC2-B. Best-fit curves were calculated using a conventional single effective diffusion coefficient and a lognormal distribution of effective diffusion coefficient, for both in-diffusion and out-diffusion experiments. Figure 12.a: in-diffusion. Vertical axis gives the value of $1-M(t)/M(t=\infty)$; see Section 3.2 text for explanation. Figure 12.b: out-diffusion. Vertical axis $M(t)/M(t=0)$.

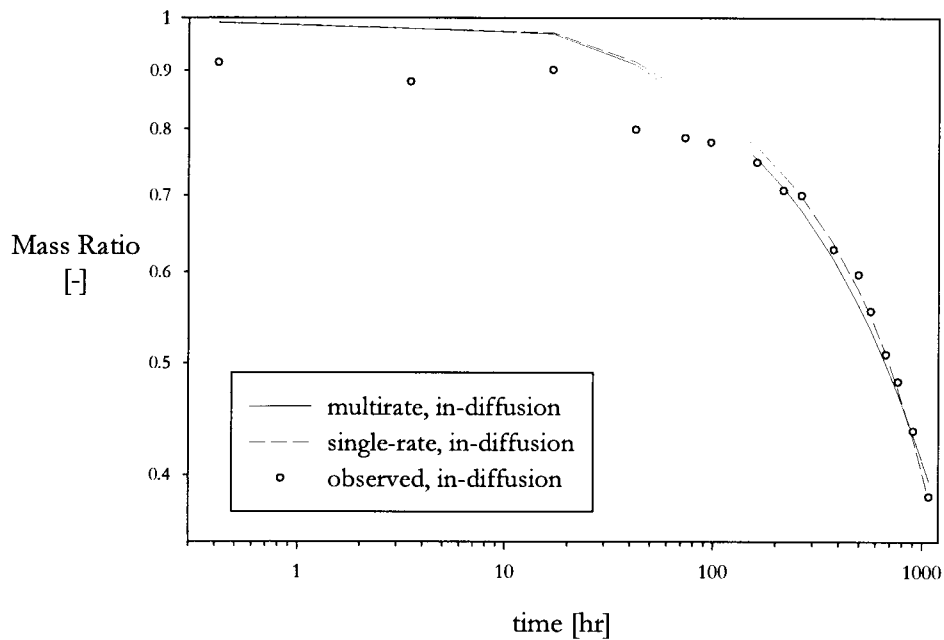


Figure 13: Mass ratio data and model responses for RC4-D. Best-fit curves were calculated using a conventional single effective diffusion coefficient and a lognormal distribution of effective diffusion coefficients, for in-diffusion. Out-diffusion experiment was not conducted for this sample due to difficulty in saturating the block with tracer. The vertical axis gives the value of $1-M(t)/M(t=\infty)$; see Section 3.2.

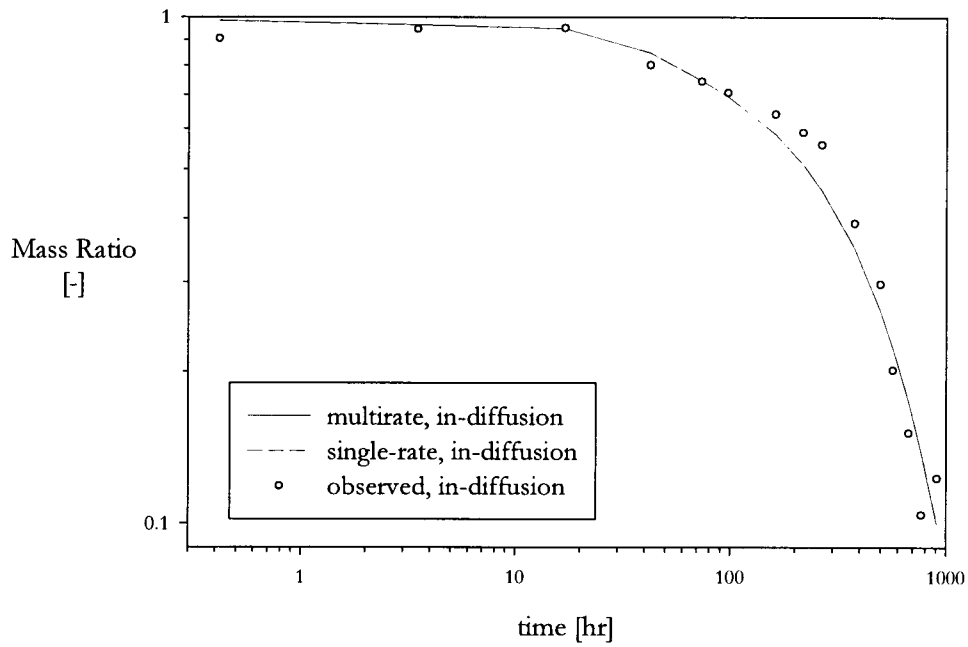


Figure 14: Mass ratio data and model responses for RC6-G. Best-fit curves were calculated using a conventional single effective diffusion coefficient and a lognormal distribution of effective diffusion coefficients, for in-diffusion. Out-diffusion experiment was not conducted for sample RC6-G due to extensive dissolution of pore-filling gypsum. The vertical axis gives the value of $1-M(t)/M(t=\infty)$; see Section 3.2.

Figure 15.a

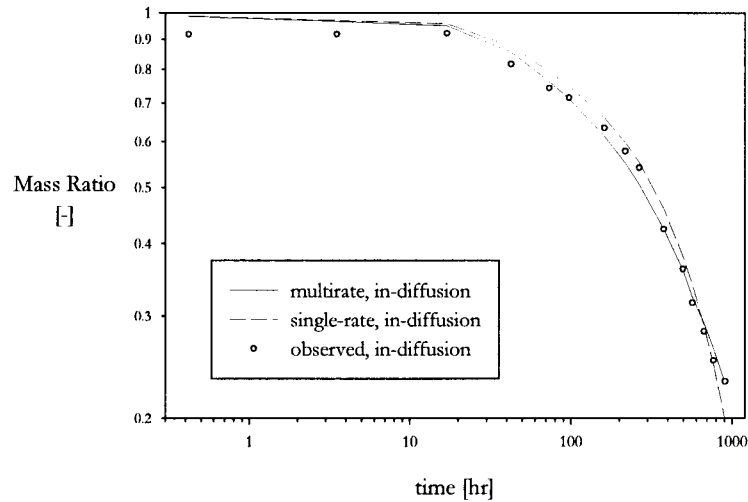


Figure 15.b

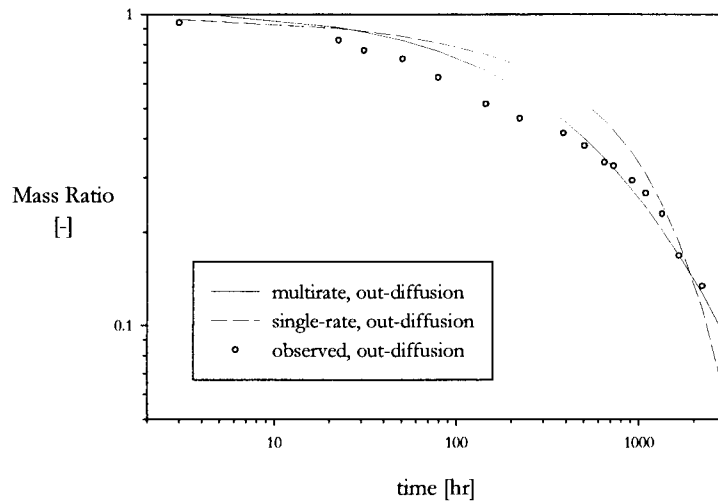


Figure 15: Mass ratio data and model responses for bulk diffusion. Best-fit curves were calculated using a conventional single effective diffusion coefficient and a lognormal distribution of effective diffusion coefficients, for both in-diffusion and out-diffusion. Figure 15.a: in-diffusion. Vertical axis gives the value of $1-M(t)/M(t=\infty)$; see Section 3.2. Figure 15.b: out-diffusion. Vertical axis is $M(t)/M(t=0)$.

Test	D_e [m ² /hr] $\ln(D_e) \pm 2\sigma$ range	$\mu_d \pm 2\sigma$ range	σ_d $\ln(\sigma_d) \pm 2\sigma$ range	RMSE _{SR}	RMSE _{MR}
B33-H	4.78E-06 <i>-12.2 ± 0.230</i> 3.80E-06, 6.02E-06	-12.0 ± 0.242 -11.8, -12.2	0.598 <i>-0.514 ± 0.0610</i> 0.563, 0.636	0.730	0.510
RC1-A	1.22E-06 <i>-13.6 ± 0.196</i> 1.00E-06, 1.51E-06	-13.5 ± 0.344 -13.2, -13.8	0.958 <i>-0.0429 ± 0.892</i> 0.393, 2.34	0.245	0.169
RC2-B	1.49E-06 <i>-13.4 ± 0.195</i> 1.25E-06, 1.84E-06	-13.4 ± 0.334 -13.1, -13.7	0.666 <i>-0.407 ± 2.08</i> 0.0832, 5.33	0.161	0.157
RC4-D	9.75E-07 <i>-13.8 ± 0.340</i> 7.23E-07, 1.43E-06	-13.9 ± 0.622 -13.3, -14.5	0.988 <i>-0.0121 ± 2.06</i> 0.126, 7.75	0.241	0.239
RC6-G	3.66E-06 <i>-12.5 ± 0.274</i> 2.83E-06, 4.90E-06	-12.5 ± 0.496 -12.0, -13.0	0.0369 <i>-3.30 ± 472</i> 0, ∞	0.516	0.517
bulk	2.15E-06 <i>-13.1 ± 0.198</i> 1.68E-06, 2.49E-06	-13.0 ± 0.194 -12.8, -13.2	0.976 <i>-0.0243 ± 0.0178</i> 0.959, 0.994	0.253	0.152

Table 1: In-diffusion results for single-rate and multirate parameter estimations. D_e is the effective diffusion coefficient estimated using a conventional single-rate model. μ_d and σ_d are parameters of the lognormal distribution used in the multirate inversion. μ_d may be compared to $\ln(D_e)$. Quality of the fits to the data are described by the log-space root mean square errors for both single-rate (SR) and multirate (MR) inversions.

Test	D_e [m ² /hr] $\ln(D_e) \pm 2\sigma$ range	$\mu_d \pm 2\sigma$ range	σ_d $\ln(\sigma_d) \pm 2\sigma$ range	RMSE _{SR}	RMSE _{MR}
B33-H	2.64E-06 -12.8 ± 1.15 8.74E-07, 8.72E-06	-11.7 \pm 3.14 -8.56, -14.8	0.946 -0.0555 ± 2.12 0.114, 7.88	5.78	3.01
RC1-A	4.96E-07 -14.5 ± 0.178 4.22E-07, 6.03E-07	-14.5 \pm 0.276 -14.2, -14.8	0.560 -0.580 ± 1.73 0.0997, 3.16	0.218	0.163
RC2-B	1.30E-06 -13.6 ± 0.161 1.06E-06, 1.46E-06	-13.5 \pm 0.240 -13.3, -13.7	0.00590 $-5.13 \pm 2.22E+04$ 0.00, ∞	0.275	0.274
bulk	1.15E-06 -13.7 ± 0.496 6.84E-07, 1.84E-06	-13.2 \pm 0.552 -12.6, -13.8	1.20 0.182 ± 0.652 0.625, 2.30	1.02	0.495

Table 2: Out-diffusion results for single-rate and multirate parameter estimations. D_e is the effective diffusion coefficient estimated using a conventional single-rate model. μ_d and σ_d are parameters of the lognormal distribution used in the multirate inversion. μ_d may be compared to $\ln(D_e)$. Quality of the fits to the data are described by the log-space root mean square errors for both single-rate (SR) and multirate (MR) inversions.

The parameter estimation statistics are calculated from the Jacobian, or sensitivity, matrix. This is a n by nt matrix, where n is the number of parameters to be estimated (1 for a single-rate model, 2 for multirate) and nt is the number of data points in the mass ratio curves (i.e., the number of times at which a data point was collected), which gives a measure of how sensitive the calculated curve is to perturbations in the fitted parameters. If a small change in a parameter value yields a large change in the calculated mass ratio curve, then the model is sensitive to that parameter and it will be well-estimated. The entries of the Jacobian, J_{ij} , consist of the derivative of the calculated mass ratio at the i^{th} time, M_i/M_T , with respect to the j^{th} parameter, p_j (e.g., *Knopman and Voss, 1987; Harvey et al., 1996*):

$$J_{ij} = \frac{\partial \left(\frac{M_i}{M_T} \right)}{\partial p_j} \quad (\text{Eqn. 36})$$

The sensitivity matrix is automatically returned by the parameter estimation subroutine used in our code (see Section 3.2).

The covariance matrix is a n by n matrix estimated by taking the inverse of the square of the Jacobian and multiplying each entry by the variance of the random error in the observed data (e.g., *Knopman and Voss, 1987*). The information in the Jacobian with respect to the sensitivity of the model to its parameters is presented in the covariance matrix in a more concise form. As we have no direct measure of the error in the data (see Section 3.1), we follow the common approach of using the mean square error between the data and the calculated curves (the square of the RMSE values given in Tables 1 and 2) as a surrogate for the replicate variance. This is a viable alternative provided that the model is an accurate representation of the physical processes responsible for the observed system response and that (similarly) error in the measurements is random. In our case, this requires that the single-rate or multirate models employed adequately describe those mechanisms within the

samples responsible for the observed mass ratio curves (note that if only a single rate of diffusion is present, the multirate model implemented in the parameter estimation routine will "collapse" into a physically correct single-rate model by returning a near-zero value for σ_d). However, external effects that occurred during the static diffusion experiments (such as gypsum dissolution; see Section 3.1), which likely affected some of the mass ratio curves, have not been incorporated into our mathematical model. Nonetheless, for most of the samples, use of the mean square error between the data and the calculated curves as an approximation to the true variance in the random error in the data is appropriate. For those cases where some additional effects clearly took place (such as out-diffusion in B33-H; see below), it seems likely that this approximation leads to an underestimate of the entries in the covariance matrix.

The square roots of the entries along the diagonal of the covariance matrix give, in turn, the standard deviations or 68% confidence intervals (σ or CI, respectively) of normally-distributed error about the best-fit values of the estimated parameters. For example, $\pm 2\sigma$ gives the region about the best-fit value of the parameter within which it can be said with 95% confidence that the actual value resides. Note that our code estimated the natural logarithms of D_e and σ_d , so the confidence intervals shown in Tables 1 and 2 are calculated with respect to the arithmetic value of μ_d but the natural logarithms of D_e and σ_d . The resulting actual ranges in D_e , μ_d , and σ_d , within which the true value can be known to exist with 95% confidence, are explicitly given in the tables.

3.3.2 Sources of Error

3.3.2.1 Experimental Error

While the quality of the fits of the calculated curves to the data is generally good, both qualitative consideration of Figures 10 through 15 and the quantitative estimates of error given in

Tables 1 and 2 indicate that these matches are inferior to those obtained from analysis of field-scale tracer tests using a multirate mass transfer model (*Haggerty et al., in preparation; McKenna et al., in preparation*). This is probably attributable to the quality of the data. Scatter in a number of the static diffusion data sets is significant relative to that seen in the extremely high-quality data collected during the field experiments, and as mentioned in Section 3.1, no means of providing a quantitative measure of uncertainty in these data currently exists. It is likely that this scatter results from some combination of failure to maintain a constant-concentration boundary condition, gypsum dissolution, and perhaps a lack of precision in the x-ray imaging technique, which is still under development.

Moreover, systematic error appears to be present in some of the static diffusion data, particularly that for B33-H out-diffusion. This mass ratio curve shows a distinct break at about 200 hours, but the in-diffusion data for the same sample shows no such irregularities. A possible explanation for this behaviour relates to the dissolution of gypsum that is believed to have occurred during saturation of sample B33-H with tracer following the in-diffusion phase (see Section 3.1). If a significant amount of gypsum dissolved, creating a new, open pore network, the distribution of diffusion coefficients could conceivably have been transformed from approximately lognormal to bimodal. One peak in the new bimodal distribution would be located roughly at the value of the diffusion coefficient given by the geometric mean of the lognormal distribution operative during the in-diffusion phase, whereas the second would correspond to the new porosity created by gypsum dissolution. If the two peaks were sufficiently far apart, this could result in a distinct break in the mass recovery curve. It is believed that such behavior has been observed in through-diffusion experiments conducted in samples of crystalline rock from the Äspö Hard Rock Laboratory in Sweden, which was tentatively interpreted to possess two discrete, or a bimodal continuous distribution of, diffusion coefficients (*Johansson et al., in preparation*).

An additional source of systematic error in the in-diffusion data for sample RC4-D arises from the fact that it was not fully saturated with solute at the end of the in-diffusion experiment. Recall from Section 3.1 that the value of $M(t=\infty)$ used to normalize the mass uptake data was calculated from the x-ray image of the fully saturated sample. If the sample was not fully saturated, inflated values of normalized mass diffused into the sample as a function of time would result. Such data would suggest faster mass uptake and a steeper late-time slope than are true. Modeling of this data could conceivably give overestimates of D_e and μ_d (Tidwell *et al.*, *in preparation*) and an underestimate of σ_d (e.g., Haggerty, 1995). It is possible that similar effects were present to a lesser degree in the other samples (Tidwell *et al.*, *in preparation*).

3.3.2.2 Concentration-Dependent Diffusion

Concentration-dependent diffusion may have occurred during the experiments (V. Tidwell, *personal communication*, 1998). Aqueous diffusion coefficients increase with increasing concentration (e.g., Cussler, 1997); as the tracer concentration in the samples varied as a function of time, the diffusion coefficients might have as well. It is not unreasonable to conjecture that such a concentration- (or equivalently, time-) dependence of the aqueous, and therefore effective, diffusion coefficients could lead to some of the observed irregularities in the data.

However, while the aqueous diffusion coefficients probably varied somewhat over the course of the experiments due to progressive changes in tracer concentration, a review of the chemical engineering literature (Cussler, 1976) revealed that concentration-dependence of the aqueous diffusion coefficient has a negligible effect on concentration profiles and breakthrough curves determined for systems similar to that in the static diffusion experiments. As the mass ratio curves used in our analysis are simply integrated concentration curves, concentration-dependence should not, therefore, contribute to the irregularities in our data sets.

Moreover, we were permitted to test whether concentration-dependent diffusion was a significant effect by observing that the in-diffusion experiments did not progress to saturation of the samples with tracer, and the out-diffusion phase did not end with full unsaturation (see Figures 10 to 15). As a result, average tracer concentration within a given sample was significantly higher during the out-diffusion phase than during in-diffusion. If concentration-dependence of the aqueous diffusion coefficients was present and had a significant effect upon the mass curves, then the out-diffusion experiments would show consistently faster diffusion coefficients than those obtained for the same sample for the in-diffusion phase. This was not observed. Tables 1 and 2 show that the best-fit values of both D_e and μ_d for a given sample are identical within measurement error for the in-diffusion and out-diffusion experiments. The only exception to this is sample RC1-A, which actually shows slightly larger D_e and μ_d for the in-diffusion phase (note that in all cases, estimates of σ_d for a given sample are statistically identical for in- and out-diffusion). It was mentioned in the discussion on Damkohler numbers in Section 2.1 that the estimated values of mass transfer parameters may depend on the duration of the experiment. The out-diffusion experiments were approximately three times as long as the in-diffusion phase; while an order of magnitude or more increase in duration of the experiment is likely required to give such time-scaling effects, it is nonetheless conceivable that the longer duration of the out-diffusion phase resulted in a decrease in estimated D_e and μ_d relative to those found for in-diffusion, counteracting the effects of concentration-dependent diffusion. However, truncating the out-diffusion data set for a given sample to the length of the corresponding in-diffusion experiment and rerunning the parameter estimations yielded results comparable to those found for the full data set.

3.3.2.3 Multicomponent Diffusion

Comparison of the aqueous diffusion coefficient of the KI tracer to the estimated distribution of diffusion coefficients (for the multirate model) and the estimated D_e (for the single-rate model)

could provide a means of confirming the reasonableness of the static diffusion results, because D_e can never exceed D_{aq} . However, three considerations show that such comparisons are both problematic and unnecessary. First, although D_e and μ_d are well-constrained, the confidence intervals about the best-fit values are nonetheless sufficiently wide to accommodate any reasonable value of D_{aq} for this system. Second, judging the entire distribution against the aqueous diffusion coefficient presumes that the tails of the distribution should be reliable. However, as discussed previously, the lognormal distribution is only an approximation to the true distribution of diffusion coefficients in the rock. Moreover, the sensitivity of any experiment to diffusion rates in the tails of the distributions is lower than that to rates of diffusion closer to the mean (*Haggerty et al., in preparation*). And third, the aqueous diffusion coefficient for the iodide tracer imaged in the static diffusion experiments is, in fact, unknown. The concentration-dependence of D_{aq} was alluded to in Section 3.3.2 and shown not to have any significant bearing upon the data and the modeling process, but this problem presents itself again if we wish to choose one particular value against which to compare our results. More fundamentally, however, the static diffusion experiments consisted of a quaternary diffusion system containing Na^+ , Cl^- , K^+ , and I^- ions. Some other species might also have been present, such as calcium and sulphate ions produced by gypsum dissolution. The implications of this are as follows (taken largely from *Cussler, 1997*).

Although each ion has, in theory, its own diffusion coefficient, maintaining electrical neutrality in a binary diffusion system (e.g., potassium iodide dissolved in pure water) requires that the cation and anion diffuse at the same rate. The net aqueous diffusion coefficient of both ions is the harmonic mean of their individual aqueous diffusion coefficients. As a result, diffusion coefficients for strong electrolytes are expressed similarly to molecular diffusion coefficients in spite of the fact that the salt may completely dissociate. If additional ions are present in the solution, however, the electrical neutrality requirement may be partially satisfied by movement of the other ions. The fact that no concentration gradient may exist for those additional ions is irrelevant. In fact, under certain

conditions, an ion in a greater-than-binary system may actually diffuse against its own concentration gradient (obviously no longer classical Fickian diffusion). For a ternary system, it is still possible to calculate the diffusion coefficient of a particular ion from those of the salts involved, and a number of theoretical and measured values are tabulated in the chemical engineering and oceanography literature (e.g., *Cussler, 1997; Li and Gregory, 1974*). For a quaternary system, however, theoretical determination of the aqueous diffusion coefficient of a particular ion is extremely difficult. The number of diffusion coefficients required to characterize a system is $(n-1)^2$, where n is the number of components. For quaternary diffusion, the diffusion coefficient is actually a 3 by 3 tensor. If sufficient gypsum dissolution occurred in a particular sample to affect diffusion (the necessary degree of dissolution might not be macroscopically noticeable), the diffusion coefficient would be a 5 by 5 tensor. Expressions exist which describe D_{aq} under such conditions, but the information necessary to evaluate these equations is not available for the diffusion system represented by the static diffusion experiments. In general, aqueous diffusion coefficients for particular species in such complex systems are determined experimentally, but this work has not been performed for the diffusion system in question.

3.3.3 Single-Rate Versus Multirate Models

Qualitative examination of Figures 10 through 15 suggests that in general, for a given sample, model curves calculated using best-fit single-rate and multirate parameters are similar. In a superficial sense, this is attributable to the facts that D_e and μ_a are identical within one confidence interval or less, and the best-fit values of σ_a , excluding those interpreted from the bulk diffusion data, are small (<1). As a result, the best-fit distribution of diffusion coefficients is both relatively narrow and centered on the best-fit single-rate diffusion coefficient. The multirate model in this case appears, therefore, similar to a single-rate model for many of the samples.

Difficulty in distinguishing single-rate from multirate processes during the analysis of these data was encountered by *Christian-Freear et al. (1997)*, who attempted to use the type-curve method for estimating multirate mass transfer parameters of *Haggerty (1995)*. While the method permitted quantification of the mean diffusion coefficient (as in our case, the mean estimated under the assumption of multirate diffusion corresponded closely to the best-fit single-rate value), they found that σ_d could not be uniquely identified. This failure was due to the fact that the method could only be reliably applied if approximately two orders of magnitude of variation in the mass ratio data were present. Multirate effects are typically clearly visible only at late times, when a large proportion of the tracer mass has been taken up or removed (see also *Ruthven and Loughlin, 1971*). In contrast, most of the static diffusion data sets offer a range of one order of magnitude or less in the mass ratio.

Use of numerical modeling and the resulting parameter estimation statistics, however, permits us to extract more information from the data than is possible using the type-curve approach. As shown in Tables 1 and 2, the 95% confidence ranges for σ_d are, proportionately, much larger than for D_c and μ_d due to the aforementioned problems with insufficient dynamic range in the data. However, it is clear that the 95% confidence ranges in σ_d for B33-H, RC1-A, and RC4-D do not approach 0. It is also clear from the RMSE_{MR} and RMSE_{SR} values provided in Tables 1 and 2 that the multirate model provides a quantifiably superior fit. Multirate diffusion, therefore, occurs in these samples. In contrast, conservative consideration of the in-diffusion and out-diffusion results taken together suggests that multirate diffusion was not detected in sample RC2-B. It is also clear that multirate diffusion was not detected in sample RC6-G.

It would be incorrect to conclude from the small estimated values of σ_d , and from the fact that two of the five samples can not be proven from this data to show multirate effects, that multiple simultaneous rates of diffusion are not significant at the lab-scale. There are three reasons for this. First, σ_d describes the standard deviation of a lognormal distribution of diffusion coefficients. As a

result, a σ_d value of only 0.5, for example, indicates that diffusion coefficients present within that sample show, at a minimum, more than half an order of magnitude variation. Second, while the visible effects of multirate mass transfer upon calculated mass ratio curves for single samples generally do not appear to be large for the small values of σ_d estimated from these data, the single-rate and multirate curves diverge at larger times (e.g., *Ruthven and Loughlin, 1971; Haggerty, 1995; Haggerty and Gorelick, 1998*). Thus, even a small value of σ_d (<1) may have significant implications for long-term solute transport. Third, the above discussion regarding whether multirate mass transfer was detected in particular samples made use of a conservative approach to hypothesis testing which, although justified, does not fully reflect the physics of the problem. We rejected the hypothesis that multiple rates of diffusion are present in a given sample if we could not prove that they were - that is, if the 95% confidence range in estimated σ_d included or very nearly included 0, and if the RMSE values did not show that the multirate model provided a significantly better fit than the single-rate model. However, these statistical tests do not indicate that a single-rate model is preferred, either. Any σ_d range which included 0 also included infinity; the inversion statistics in such a case simply tell us that it is impossible to infer from the available data whether multirate effects are present in that sample. This is due to a high degree of insensitivity of the calculated result for that block, over the dynamic range of the data and for a given value of μ_d (which is well-estimated in all cases), to the value of σ_d . If a single-rate model was clearly superior, the multirate inversion would return a value of σ_d near 0, with narrow confidence bounds. In addition, multirate and single-rate curves are, as mentioned above, similar for early-time data (i.e., prior to uptake or removal of a large proportion of the solute mass). This is true even for somewhat larger values of σ_d (e.g., *Haggerty and Gorelick, 1998*). Thus, failure to detect multirate effects in two of the five data sets is attributable primarily to lack of dynamic range in the mass ratio data, and it can not be stated with confidence whether distributed diffusion does or does not occur in those samples. It is also important to note that while we have described this approach as being conservative, this is only true in relation to historical treatments of

diffusive mass transfer. In fact, the most cursory examination of any geologic media reveals it to be highly heterogeneous. The use of some form of multirate diffusion model is, therefore, a conservative treatment of mass transfer in naturally-occurring porous media; application of a single-rate model requires the simplifying assumption of homogeneity, which must be justified.

The bulk diffusion data clearly show multirate effects. A multirate model provides both a qualitatively and quantitatively superior fit (Figure 15 and Tables 1 and 2). This is to be expected, as the bulk data sets combine the diffusion responses of individual blocks which are seen to give different values of D_e and μ_d . It is useful to compare the results from the bulk diffusion data to that from the individual samples. Using in-diffusion as an example, it can be seen from Table 2 that the arithmetic average of all the best-fit D_e (and μ_d) values for the individual blocks is equal, within much less than one confidence interval, to the best-fit D_e (and μ_d) found for the bulk data. In addition, the 16th and 84th percentile values in the cumulative distribution function (CDF) of effective diffusion coefficients for the bulk data, as parameterized by the best-fit μ_d and σ_d , correspond quite closely to the minimum (RC4-D) and maximum (B33-H) best-fit values of D_e and μ_d found for individual blocks. Of course, neither the five single-rate diffusion coefficients nor the five lognormal distributions from the individual slabs combine additively, in a rigorous sense, to form a new lognormal distribution corresponding to the bulk experiment. However, it is clear that the best-fit lognormal distribution estimated solely from the bulk diffusion data provides a reliable representation of the range of diffusion coefficients known to exist within the individual slabs.

3.3.4 Comparison to Other Culebra Modeling Results

Our best-fit values for single-rate effective diffusion coefficients are consistent with those found by *Christian-Frear et al. (1997)*, who modeled the in-diffusion mass ratio data for three samples by manual calibration using a single-rate code. For RC2-B and RC6-G, reported D_e values are

statistically identical to our best-fit values. Their value of D_e for B33-H is very slightly smaller than the -2 CI value we obtained.

Christian-Freear et al. (1997) also attempted to interpret the mass ratio data in terms of multirate diffusion using the type-curve method of *Haggerty (1995)*, as discussed in Section 3.3.3. Although they were not able to determine values for σ_d using this simple technique due, primarily, to insufficient dynamic range in the data, they determined values for μ_d for a number of samples. Values were not reported, but they indicated that interpreted μ_d values corresponded well to D_e values found using a single-rate model. We observed similar behaviour in our modeling (Section 3.3.3). As their D_e estimates are similar to ours, their estimated μ_d values are probably also consistent with those we found. For both single-rate and multirate models, we assign more validity to our results due to the superior ability of formal inversion techniques to identify a best-fit value and provide a quantitative measure of the degree of confidence that can be held in those results.

Of greater interest is how our multirate modeling of the laboratory-scale experiments compares to that completed for field-scale tracer tests. Figure 16 shows best-fit lognormal distributions of the diffusion rate coefficient, D_e/a^2 , for a number of static diffusion and field-scale experiments, where a is the diffusion path length within the matrix (Section 2.1). Distributions of diffusion rate, rather than effective diffusion coefficient, were estimated from the field-scale tracer tests because the diffusion path length represents an additional form of pore-scale variability in diffusion processes not experienced at the lab-scale. We converted our estimates of the distributions of D_e to distributions of D_e/a^2 using:

$$\mu_{dr} = \mu_d - \ln(a^2) \quad (\text{Eqn. 37})$$

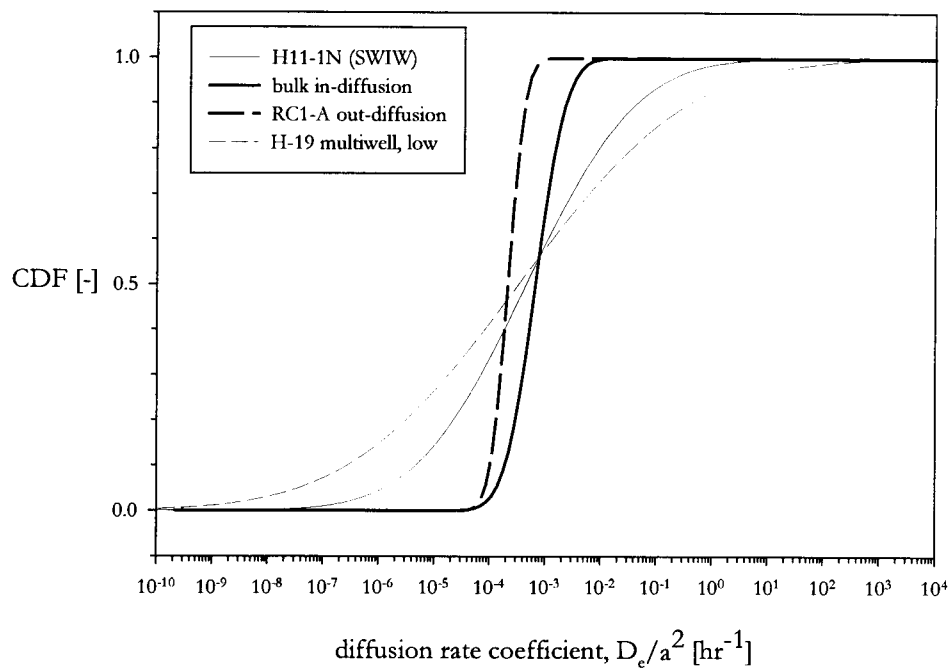


Figure 16: CDFs from lab- and field-scale experiments. All are best-fit lognormal distributions of diffusion rates. Distributions of effective diffusion coefficients estimated from lab-scale work (individual samples and bulk diffusion) have been converted to diffusion rate coefficients using the length of the sample perpendicular to the reservoir as a measure of diffusion path length. This conversion is completed so as to render the CDFs from the lab- and field-scale work amenable to presentation on the same plot, but the resulting μ_{dr} for the lab-scale work cannot be taken to be reliable; the displayed widths of the distributions, however, are robust. H-11 field-scale data from *Haggerty et al.* (in preparation); H-19 field-scale data from *McKenna et al.* (in preparation).

where μ_{dr} is the geometric mean of the lognormal distribution of diffusion rates, μ_d is the geometric mean of the lognormal distribution of effective diffusion coefficients estimated in our static diffusion work, and a , the diffusion path length, is taken to be the length of the sample in the static diffusion experiment measured perpendicular to the reservoir. This choice is discussed below. σ_d does not require adjustment, as the length of a given sample is constant and all variability in diffusion processes thus results from heterogeneity in the effective diffusion coefficient.

μ_{dr} values from the static diffusion experiments appear to correspond very closely to those estimated for single-well and two-well field-scale tracer tests conducted at the H-11 hydropad, and at the H-19 hydropad, from which the static diffusion samples were collected. A number of independent interpretations of several different types of experiment would thus seem to provide estimates of μ_{dr} that converge upon a narrow range of values. However, taking the length of the sample as the value of a in Eqn. 37 is likely inappropriate. The values of μ_d estimated from the lab-scale work are independent of the length of the sample, and much larger or smaller samples would therefore give the same result. Thus, the values of μ_{dr} derived from the lab-scale work and presented graphically in Figure 16 reflect, in part, an arbitrarily chosen sample length which has no effect on the diffusion process. The fact that these μ_{dr} values correspond very closely to those directly estimated in the field-scale work may be explained in two ways. First, it may suggest that the mean diffusion path length in the Culebra, in situ, may be roughly similar to the lengths of the samples used in the static diffusion experiments. Second, it may be a coincidence; we will adopt this more conservative interpretation. Note that we have not adjusted μ_{dr} for the difference (perhaps a factor of 2) between the aqueous diffusion coefficient of the KI tracer used in the lab-scale experiments and that for the benzoic acid tracers used in the field-scale experiments, on account of these significant uncertainties in the appropriate value of a and the uncertainty in the aqueous diffusion coefficient of the KI tracer (see Section 3.3.2.3).

In contrast to μ_d , the values of σ_d corresponding to the distributions given in Figure 16 are robust and show a great deal of variability between the experiments. In general, the distributions are narrow for individual samples, somewhat larger for the bulk diffusion experiment, and considerably larger for the field-scale tests; that is, as the spatial scale of the experiment increases, greater variability in diffusion rate is encountered by the solute. Distributions estimated from both multiwell and SWTW (not shown) tracer tests at H-19 are wider than those from the H-11 hydropad. This has been attributed to the more distributed nature of advective porosity at H-19 relative to H-11 (*Haggerty et al., in preparation*).

When comparing the results from lab-scale diffusion experiments to those from field-scale tests which involve advective tracer transport, it is important to consider the effects that different types of porosity have upon each. In the field-scale SWTW and two-well convergent flow tests, advective porosity acts as a distinct entity from diffusive porosity. In contrast, in the static diffusion experiments all porosity present in the rock acts as diffusive porosity - including interconnected pore networks which could contribute to advective transport rather than mass transfer in the field-scale tests. In the absence of a hydraulic gradient, the addition of such nominally advective porosity to the total diffusive porosity would not produce dramatic effects. Nonetheless, it seems likely that well-connected, and perhaps less restricted, pore space would give rise to higher bulk effective diffusion coefficients than the dead-end pore space which functions as the immobile zone in a test involving advective transport.

This may be an important consideration in some rocks, but it is unlikely to have much effect upon our interpretation of diffusion processes in the Culebra dolomite for two reasons. First, the diffusive porosity (i.e., matrix or dead-end porosity) in the Culebra dolomite is typically about one to two orders of magnitude larger than the advective porosity (*Haggerty et al., in preparation; McKenna et al., in preparation*). As a result, interconnected pore networks that would act as advective porosity in an

active tracer test generally represent a negligible addition to the total porosity sampled in the static diffusion experiments. In addition, a pore network or fracture that spans the entire sample used in the static diffusion experiment might, in situ, have terminated some short distance away. This feature would behave as advective porosity in the sample if a hydraulic gradient had been established across it, and might be described as interconnected, advective-type porosity if viewed in hand specimen. However, it would act as dead-end pore space within the formation. As a result, the contribution it makes to diffusion within the sample is an accurate representation of the role it would play in diffusive mass transfer during a field-scale, advective-flow tracer test.

Another data set against which results from the static diffusion modeling can be compared is the CDF of formation factors introduced in Section 3.2 (Figure 9). As D_e is inversely proportional to formation factor, the distribution of one should be equivalent to that of the other. Unfortunately, calculations of D_e from formation factors may be unreliable due, for example, to the dependence of formation factor measurements on the properties of the ions present in the pore fluid (see *Kelley and Saulnier, 1990* for discussion). It is therefore difficult to directly convert the fitted CDF of formation factors to a CDF of D_e . However, the standard deviations of the lognormal distributions should be similar if both sets of data were obtained from the same rock. These formation factors were determined for 21 samples of Culebra dolomite by TerraTek (*TerraTek contractor's report, 1997*) retrieved from the H-19 hydropad, primarily from borehole H-19 b4 (*R. Beauheim, personal communication, 1997*); this is the same location from which the samples used in the static diffusion experiments were sourced. The standard deviation in the best-fit lognormal CDF of formation factors determined from all 21 samples should, therefore, be similar to σ_d estimated from the bulk static diffusion experiments. σ for the formation factors was found to be roughly 0.7, which corresponds closely to the values found for bulk diffusion data. Failure of the values to be exactly equal is not troublesome. Effective diffusion coefficients may be a function of rock properties other than tortuosity, such as the restrictivity of the pores (see Section 2.1), which may not be reflected in

the formation factor data. Moreover, formation factor determinations were not performed on the same samples used in the static diffusion experiments. This second issue may be of particular significance as samples used in the diffusion experiments were selected to represent a distinctive suite of Culebra matrix porosity types. As a result, analyses of the diffusion data might lead to slightly higher estimated values for σ_d than obtained from the formation factor data.

The reasonably close correspondence between the standard deviations of these two distributions serves as supporting evidence for our interpretation of the static diffusion experiments. It also raises the possibility that formation factors – which are much easier and cheaper to obtain than laboratory diffusion data – might provide an indirect but reasonably reliable means of estimating pore-scale heterogeneity at many locations in the Culebra dolomite.

3.4 Discussion

3.4.1 Correlation of Modeling Results to Observable Geology

One objective of the study was to determine whether the quantitative information provided by single-rate and, in particular, multirate modeling could be correlated to macroscopically visible features in the samples. Figures 17 through 24 give plots of a ranking of the samples in terms of the relative presence of 4 types of features against estimated values of μ_d and σ_d . Degrees of vugginess, gypsum-filling, and fracturing, in addition to bulk porosity, are considered. Qualitative rankings of the blocks in terms of the relative abundances of these features were provided by *V. Tidwell (personal communication, 1998)*, except for porosity, which was determined using gravimetric methods (*Christian-Frear et al., 1997*). Best-fit and ± 1 CI values for μ_d and σ_d are shown for both in-diffusion and out-diffusion. Note that only 3 samples were used in the out-diffusion experiment. As μ_d and $\ln(D_e)$ are identical within ± 2 CI or less for all tests, plots of μ_d also address possible correlation of single-rate

Figure 17.a

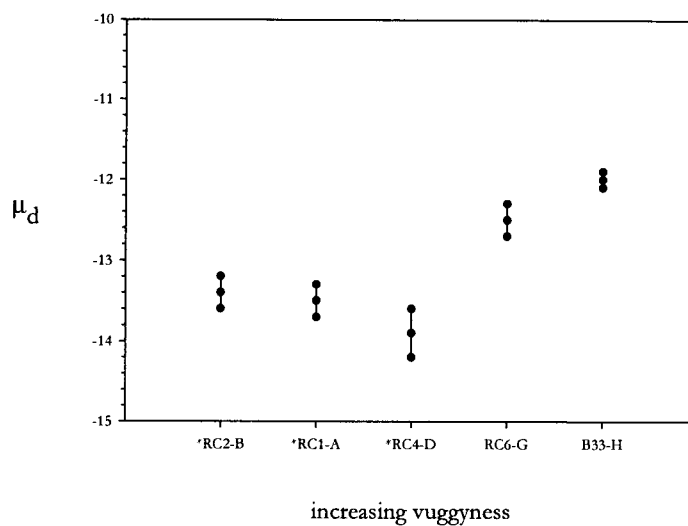


Figure 17.b

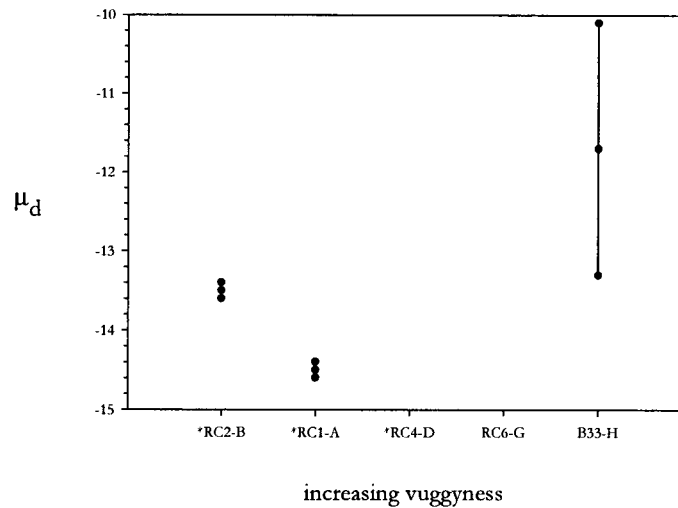


Figure 17: Correlation of μ_d to degree of vugginess. Figure 17.a: in-diffusion. Figure 17.b: out-diffusion. Best-fit and ± 1 CI values of μ_d are shown. Rankings of the blocks in terms of degree of vugginess were provided by *V. Tidwell (personal communication, 1998)*. *Samples RC1-A, RC2-B, and RC4-D were observed to contain almost no vugs (*V. Tidwell, personal communication, 1998*).

Figure 18.a

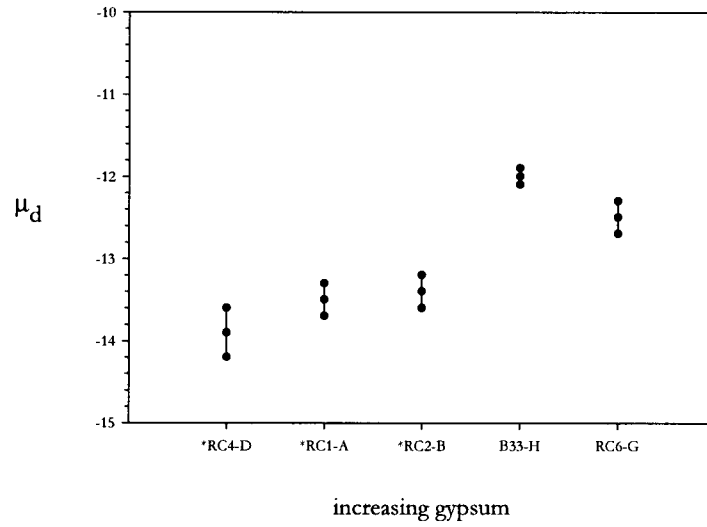


Figure 18.b

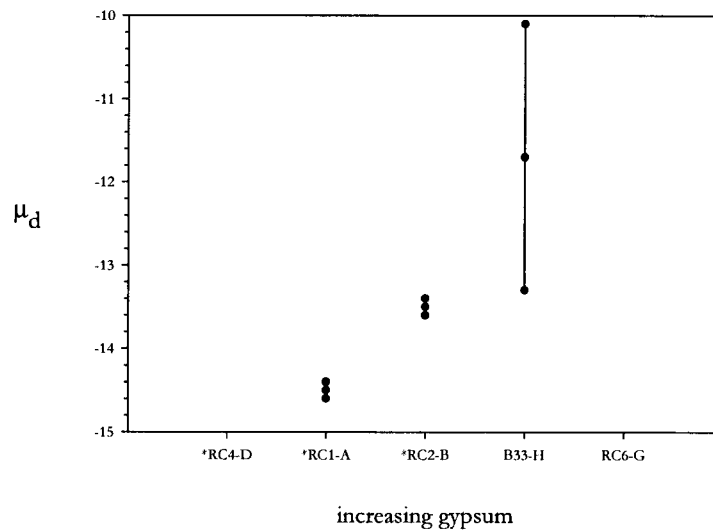


Figure 18: Correlation of μ_d to degree of gypsum-filling. Best-fit and ± 1 CI values of μ_d are shown. Figure 18.a: in-diffusion. Figure 18.b: out-diffusion. Rankings of the samples in terms of the degree of gypsum present were provided by *V. Tidwell (personal communication, 1998)*. *Samples RC1-A, RC2-B, and RC4-D were not observed to contain gypsum (*V. Tidwell, personal communication, 1998*).

Figure 19.a

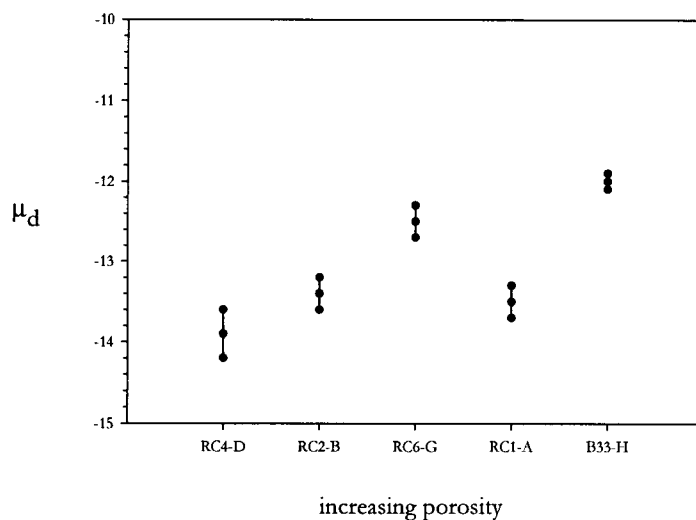


Figure 19.b

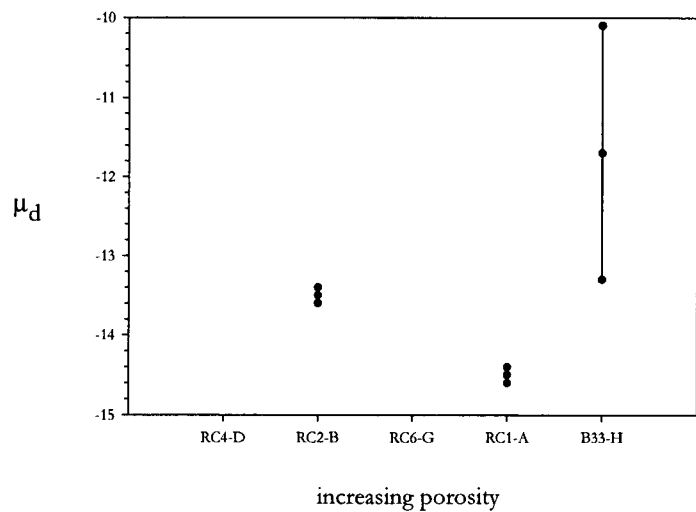


Figure 19: Correlation of μ_d to bulk porosity. Figure 19.a: in-diffusion. Figure 19.b: out-diffusion. Best-fit and ± 1 CI values of μ_d are shown. Ranking of the blocks in terms of increasing bulk porosity was taken from *Christian-Frear et al. (1997)*.

Figure 20.a

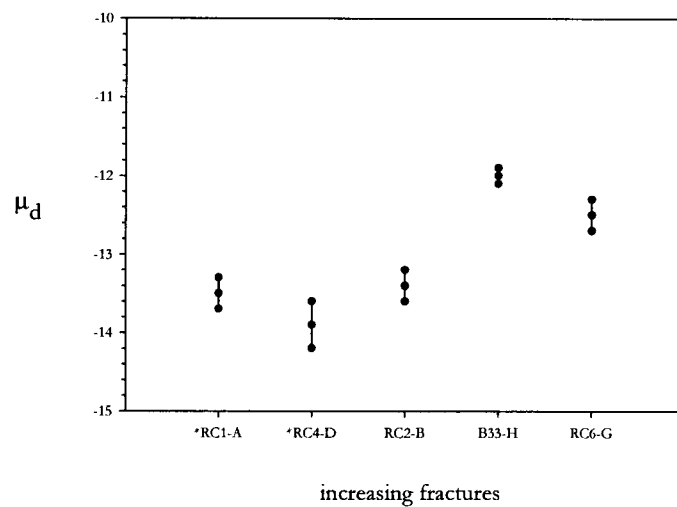


Figure 20.b

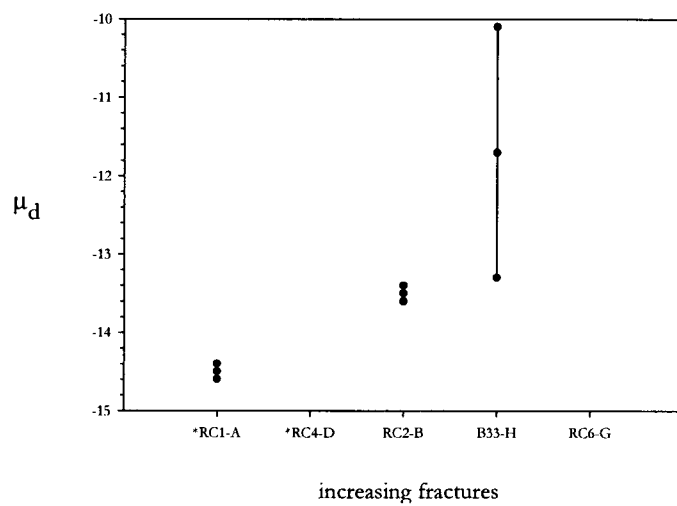


Figure 20: Correlation of μ_d to degree of fracturing. Figure 20.a: in-diffusion. Figure 20.b: out-diffusion. Best-fit and ± 1 CI values of μ_d are shown. Rankings of the samples in terms of increasing fracturing were provided by *V. Tidwell (personal communication, 1998)*. *Samples RC1-A and RC4-D were not observed to contain fractures (*V. Tidwell, personal communication, 1998*).

Figure 21.a

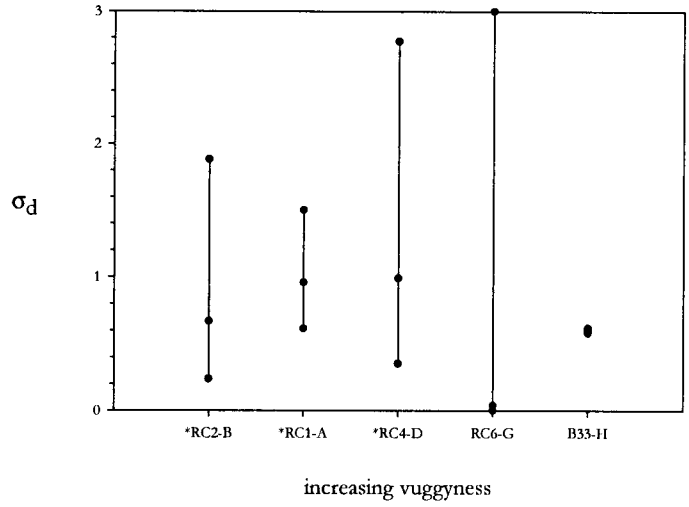


Figure 21.b

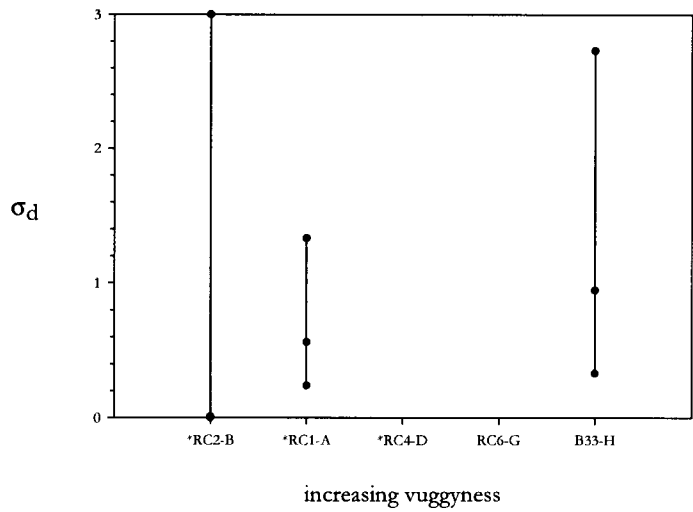


Figure 21: Correlation of σ_d to degree of vugginess. Best-fit and ± 1 CI values of σ_d are shown. Figure 21.a: in-diffusion. Figure 21.b: out-diffusion. Ranking of the blocks in terms of increasing vugginess was completed by *V. Tidwell (personal communication, 1998)*. *Samples RC1-A, RC2-B, and RC4-D were observed to contain almost no vugs (*V. Tidwell, personal communication, 1998*).

Figure 22.a

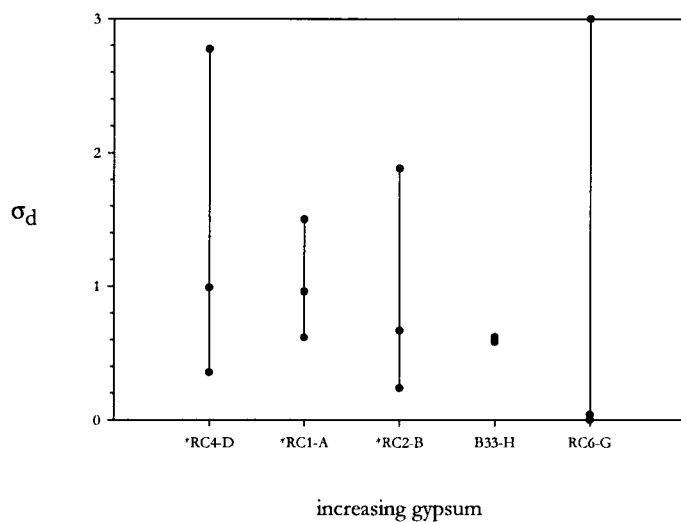


Figure 22.b

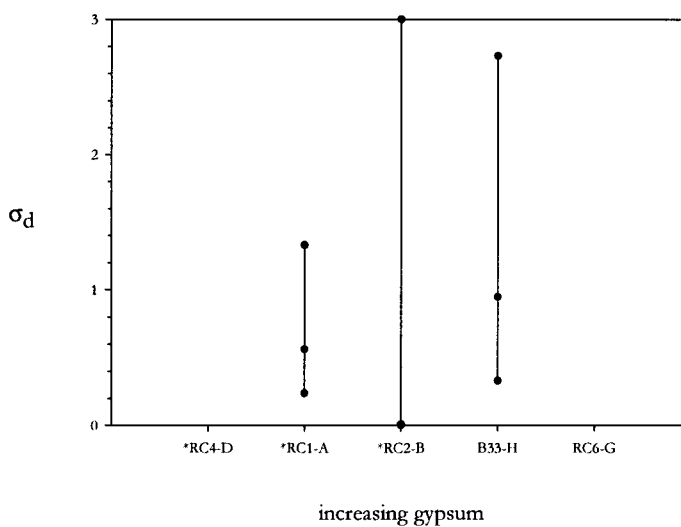


Figure 22: Correlation of σ_d to degree of gypsum-filling. Best-fit and ± 1 CI values of σ_d are shown. Figure 22.a: in-diffusion. Figure 22.b: out-diffusion. Ranking of the blocks in order of increasing gypsum presence was completed by *V. Tidwell (personal communication, 1998)*. *Samples RC1-A, RC2-B, and RC4-D were not observed to contain gypsum (*V. Tidwell, personal communication, 1998*).

Figure 23.a

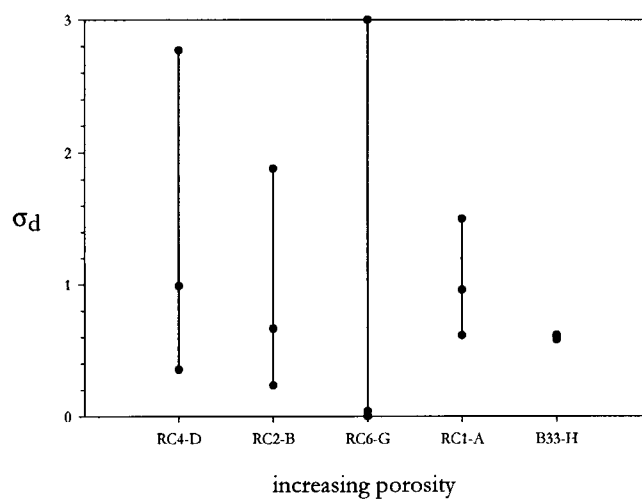


Figure 23.b

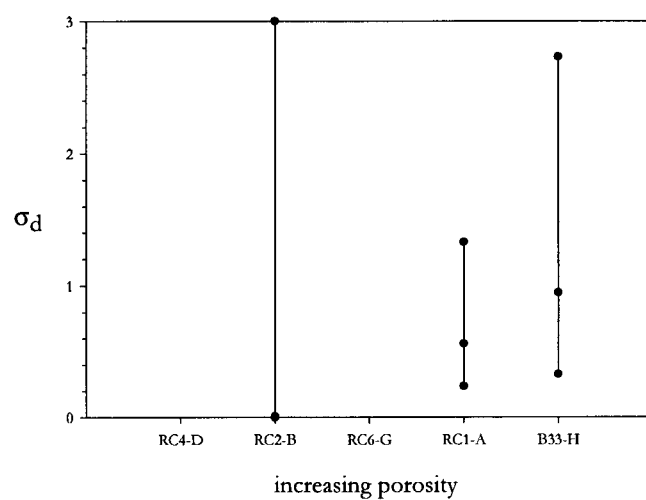


Figure 23: Correlation of σ_d to bulk porosity. Best-fit and ± 1 CI values of σ_d are shown. Figure 23.a: in-diffusion. Figure 23.b: out-diffusion. Ranking of the blocks was taken from *Christian-Frear et al. (1997)*.

Figure 24.a

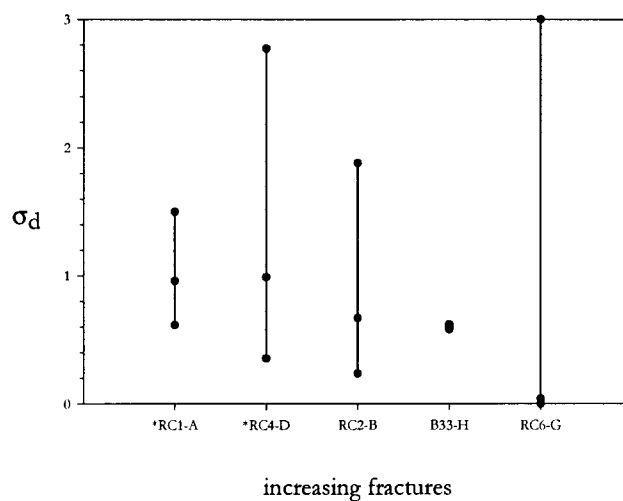


Figure 24.b

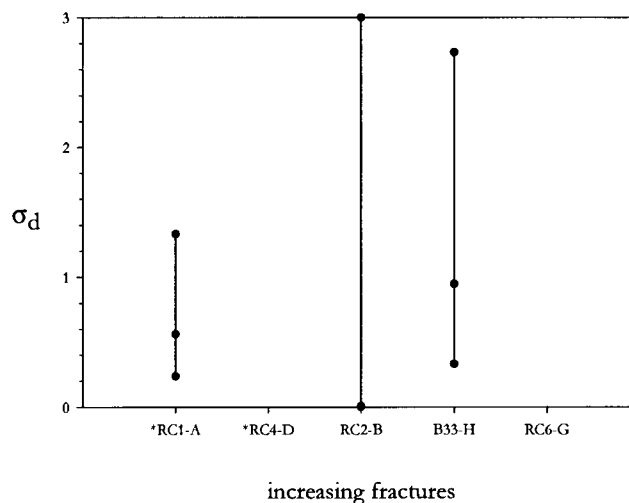


Figure 24: Correlation of σ_d to degree of fracturing. Best-fit and ± 1 CI values of σ_d are shown. Figure 24.a: in-diffusion. Figure 24.b: out-diffusion. Rankings of the blocks were provided by V. Tidwell (personal communication, 1998). *Samples RC1-A and RC4-D were not observed to contain fractures (V. Tidwell, personal communication, 1998).

estimation results to geologic characteristics of the samples. ± 1 CI, rather than ± 2 CI, results are shown because the latter confidence bounds are very large for some samples, particularly in σ_d . The ± 1 CI range in σ_d values for RC6-G in-diffusion and RC2-B out-diffusion is 0 to infinity; the upper limit is represented simply by a point at the upper border of the graph. In addition, a plot of the number of types of features (vugginess, fracturing, and gypsum-filling) observed macroscopically in the sample against estimated σ_d is given in Figure 25. Confidence bounds are omitted from this figure for simplicity, but results from the bulk in- and out-diffusion experiments are included.

There appears to be a correlation between bulk porosity and μ_d (Figure 19). As the porosity factors cancel in the expression for the mass ratio curves (Eqn. 28) from which μ_d is estimated, porosity should not directly affect the value of μ_d . In addition, our definition of D_e does not include porosity (Section 2.1). However, as the proportion of the rock volume occupied by pore space increases, it becomes more likely that individual pores will intersect. Interconnected pore space likely leads to faster average rates of diffusion, relative to dead-end pores in which solute becomes trapped (e.g., *Dykhuiszen and Casey, 1989*). Another, related, explanation for this observed behaviour is suggested by the apparent correlations between μ_d and degrees of fracturing and vugginess (Figures 17 and 20), and between the relative presence of these features and bulk porosity (Figure 26). Obviously, the presence of major, macroscopically visible porosity features could contribute to increased porosity and, as a result, to faster diffusion rates. In addition, though, fractures and vugs, being large features tend to span considerable portions of the sample or even the sample in its entirety (note that many vugs are associated with fracturing; refer to Section 2.2.2.2). Consequently, these particular types of porosity are especially effective at providing the extended pore networks that could increase mean diffusion rates. A correlation also appears to exist between the amount of gypsum present and both μ_d and porosity. This is likely because gypsum presence is diagenetically related to fracturing and vugginess. Gypsum occurs in the Culebra as a fracture- and vug-filling

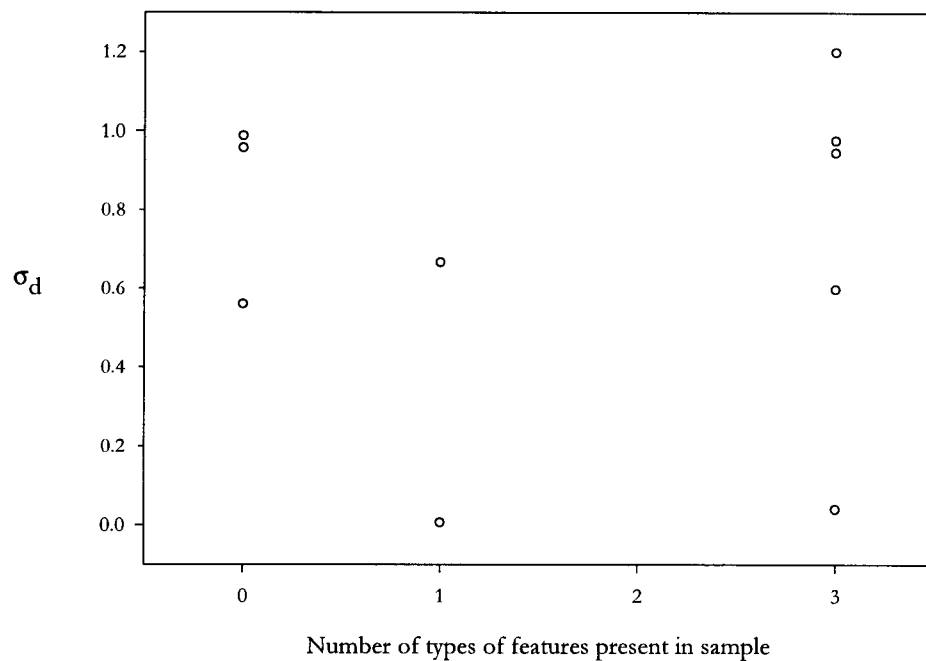


Figure 25: Correlation of σ_d to number of types of features observed. Features considered are vugginess, fracturing, and gypsum-filling (*V. Tidwell, personal communication, 1998*). Our best-fit values of σ_d for in-diffusion and out-diffusion are shown, but confidence bounds are omitted from this figure for simplicity. Results from the bulk in- and out-diffusion experiments are included.

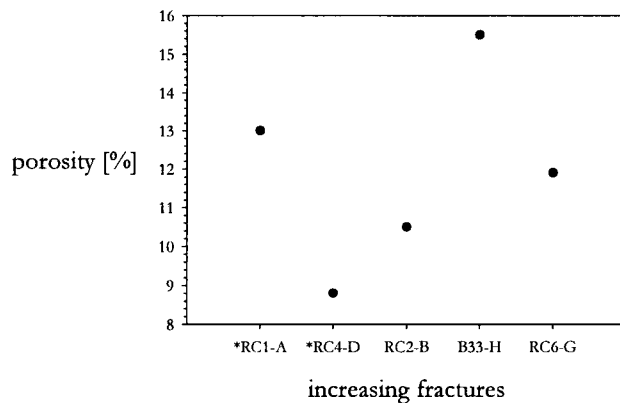


Figure 26.a

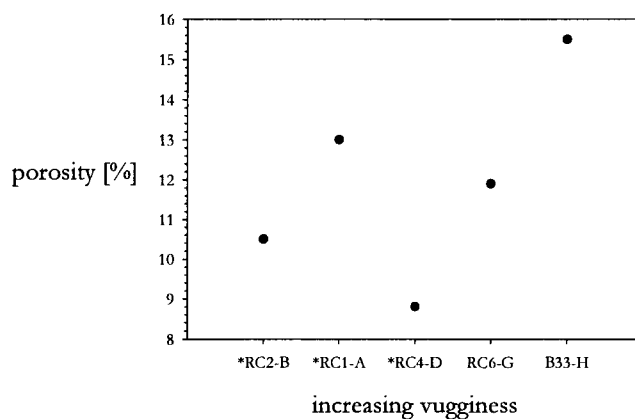


Figure 26.b

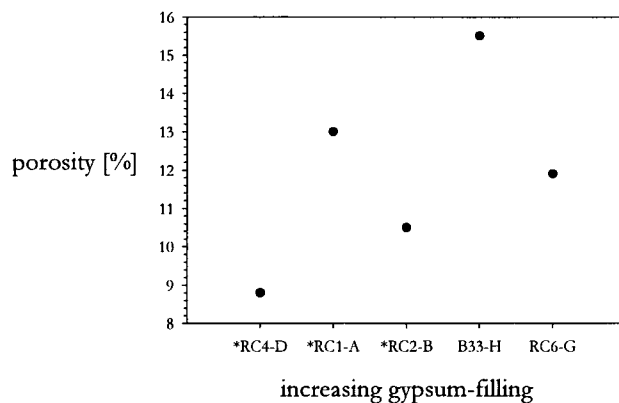


Figure 26.c

Figure 26: Correlations between porosity and macroscopic features. Figure 26.a: degree of fracturing against porosity. Figure 26.b: degree of vugginess against porosity. Figure 26.c: degree of gypsum-filling against porosity. Rankings of samples in terms of relative abundance of macroscopic features provided by *V. Tidwell (personal communication, 1998)*. Porosities are from *Christian-Freear et al. (1997)*.

cement. However, considerable gypsum dissolution has taken place in the Culebra, forming secondary porosity (see Sections 2.2.2.2 and 2.2.3). It is likely that, although gypsum cementation remains in these samples, some interconnected porosity has been reopened along the long, continuous diffusion pathways that the gypsum inhabits. It is possible, then, that the presence of gypsum simply serves as a marker for the presence of fracture and vug porosity.

In contrast, best-fit values of σ_d do not appear to correlate with porosity, fracturing, vugginess, gypsum-filling, or the number of types of features present in the samples. Much of the difficulty with evaluating the presence of correlations between σ_d and such geologic characteristics, apart from the scarcity of data, lies in the large confidence bounds in estimated σ_d (see Section 3.3.3). In general, a line of positive, negative, or zero slope can be drawn through any of the available data such that it passes through the ± 1 CI range for estimated σ_d (see Figures 21 through 24), but this clearly can not be taken as evidence of a relationship. However, the apparent absence of a correlation between best-fit σ_d and fracturing, gypsum-filling, and vugginess, or the variety of such features present in a sample (Figure 25), may be an indication that such macroscopic characteristics of the rock contribute less to the establishment of a distribution of diffusion rates than does variability in much smaller-scale porosity, such as intergranular or intercrystalline porosity. Macroscopically highly homogeneous soils, for example, have been shown to possess orders of magnitude in variation in diffusion rates, corresponding to heterogeneity at the micropore-scale (e.g., *Haggerty and Gorelick, 1998*). An alternate explanation for the apparent absence of a correlation is that the magnitude of σ_d may be reflective of variations in pore geometry within a macroscopic feature. A third possibility is that σ_d could be a function of additional macroscopic features within the sample that are not externally visible. However, it seems likely that such features would also help to control μ_d ; this is inconsistent with the observed correlations between μ_d and the presence of externally visible macroscopic features.

Due to the small number of samples considered and the large confidence bounds on σ_d , firm conclusions regarding the correlation of mass transfer parameters to readily observable geologic features can not be drawn. Nonetheless, available information does suggest that the mean diffusion rate in the Culebra dolomite may be strongly influenced by large-scale features such as fractures and vugs, but the breadth of the distribution of diffusion rates may be more strongly controlled by variability in pore geometry within such macroscopic features and/or by micropore-scale variability.

3.4.2 Development of Spatial Scaling Relationships

Another main goal of the work is to evaluate relationships between mass transfer parameters determined from laboratory experiments and those inferred from field-scale tracer tests. We briefly broached the subject in Section 3.3.4, where we noted that as the spatial scale of an experiment increases, the distribution of rates grows broader (Figure 16). We now consider the matter in more detail.

Best-fit values of σ_d are plotted on Figure 27 against sampling volumes for 14 experiments. Three classes of spatial scale are considered: individual samples in the static diffusion experiments, bulk static diffusion data, and SWIW and two-well tracer tests at the field-scale. All experiments were conducted at the H-19 hydropad or on samples taken from that location, so any inferred relationships should be reflective only of sampling volume, rather than being a product of major regional-scale changes in Culebra hydrogeology. Best-fit values of μ_{dr} are also plotted on Figure 27 against sampling volumes for the 10 experiments from the lab-scale work. Field-scale results are not included for μ_{dr} due to the uncertainty in conversion between the effective diffusion coefficients estimated from the static diffusion experiments and diffusion rates estimated from the field-scale experiments (see Section 3.3.4). σ_d does not require this conversion.

Figure 27.a

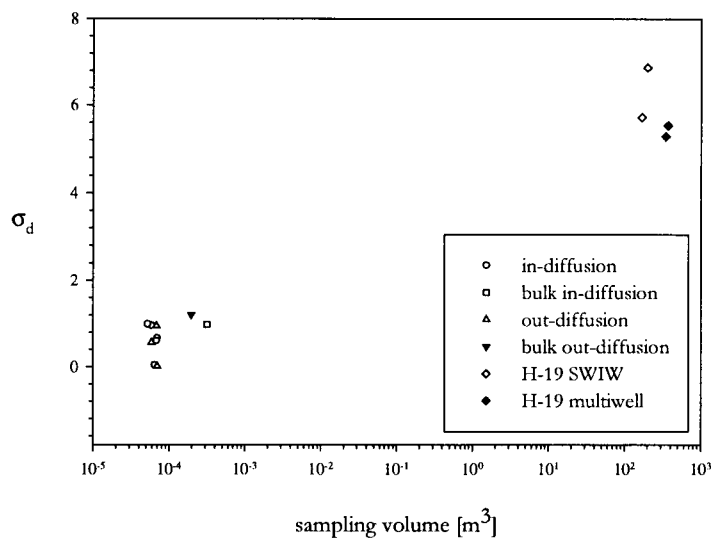


Figure 27.b

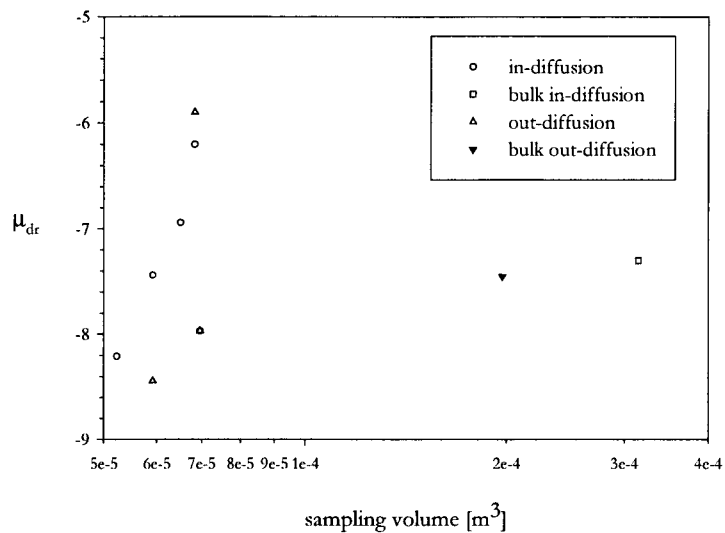


Figure 27: Correlation between mass transfer parameters and spatial scale of experiment. Figure 27.a: correlation between σ_d and sampling volume. Figure 27.b: correlation between μ_{dr} and sampling volume. Note logarithmic horizontal axes on both plots.

Sampling volume for an individual sample in the static diffusion experiments was taken to be the full volume of the sample. For the bulk diffusion experiments, the sum of the volumes of the constitutive blocks was used. Sampling volumes for the SWIW and multiwell tests, respectively, were taken to be $\pi r^2 b$ and $0.5\pi r^2 b + rpb$ (J. Ogintz, *personal communication, 1998*), where b is the thickness of the formation (4.4 m; see Section 2.2.1) and p is the distance from the injection to the pumping well in the multiwell case. The radial distance from the injection well at which a normalized concentration of approximately 10^{-5} is found at the end of injection, r , was determined from intermediate output files produced by the STAMMT-R modeling runs used in *Haggerty et al. (in preparation)* and *McKenna et al. (in preparation)*. Confidence intervals have been omitted from the figures for simplicity. However, uncertainty in the parameter values is implicitly reflected by incorporating results from both the in-diffusion and out-diffusion phases of the lab-scale experiments, and from two SWIW and two multiwell tests conducted at the same hydropad. In theory, in-diffusion and out-diffusion results for a given sample should be the same, as should two tracer tests of the same type (SWIW or two-well) conducted at the same location. The fact that they are not is a reflection of uncertainty in the parameter estimates, and by including all experimental results we introduce an indirect measure of that uncertainty into the plot. It should also be noted that all experiments have time-scales of the same order of magnitude, an issue to which we will return later in this section.

Best-fit μ_{dr} values from individual samples in the static diffusion experiments show a large degree of scatter. As confidence bounds for these parameter estimates are fairly narrow, this should be taken to represent true variation in the mean diffusion rate from one sample to the next. Estimated μ_{dr} values for the bulk diffusion experiments are mutually nearly identical, and are approximately equal to the arithmetic mean of μ_{dr} values estimated for their constitutive individual samples (refer to Section 3.3.3). Although the mean diffusion rates estimated from the field-scale work are not directly comparable to μ_{dr} from the lab-scale experiments, it is worth noting that the

best-fit μ_{dr} values for the multiwell tests at the H-19 hydropad and the SWIW and multiwell tests at the H-11 hydropad are all mutually similar.

Best-fit σ_d values from individual samples in the static diffusion experiments show a smaller degree of scatter than seen in μ_{dr} , though it must be remembered that confidence intervals for these σ_d estimates are generally large. Estimated σ_d for the bulk diffusion experiments are mutually similar, well-constrained, and larger than the arithmetic average of σ_d values determined from individual samples. Recall also from Section 3.3.3 that 1 σ_d in the distribution of rates estimated for the bulk diffusion experiments corresponds very closely to the range in best-fit D_e and μ_{dr} measured for individual, constitutive samples. At the field-scale, σ_d estimates from the H-19 hydropad are greater than those found at H-11 (*Haggerty et al., in preparation; McKenna et al., in preparation*), but all field-scale σ_d values are much larger than those found from smaller-scale experiments. Although data are available for essentially only 3 sampling volumes, it is clear that σ_d scales with sampling volume, and it appears to do so in a roughly logarithmic fashion: the best-fit curve through the points on the semi-log plot given in Figure 27.a is a straight line (not shown).

We interpret these results in the following manner. The geometric mean varies as a function of spatial scale in a manner similar to that in which many other geologic properties do. Very small sampling volumes yield point estimates of μ_{dr} , with quite different values from one measurement location to the next. Each small sampling volume has a different distribution of rate coefficients characterized by a different geometric mean or, if diffusion processes within those small sampling volumes are essentially single-rate, a different D_e . This spatial scale corresponds to the individual samples in the static diffusion experiments. A somewhat larger sampling volume (the representative elementary volume, REV) yields an average value of μ_{dr} , as local heterogeneities are integrated. The distribution at the REV-scale has grown broader, incorporating the fluctuations in the point

estimates, and the corresponding mean rate is approximately the arithmetic average of the point estimates of μ_{dr} from the smaller spatial scale. This corresponds to the bulk diffusion experiments. We might hypothesize that larger experimental scales (the field-scale tracer tests) may give rise to perturbations about the mean rate coefficient obtained at the REV-scale, as more aquifer heterogeneities are encountered at the progressively farther reaches of the sampling volume. However, there would be no systematic increase or decrease in μ_{dr} with increasing spatial scale and the value of μ_{dr} obtained at the REV-scale would remain a reasonable estimate, provided that no major, large-scale changes in the nature of the aquifer occur. This is consistent with, although not required by, the observation that the values of μ_{dr} from the field-scale experiments, at two different hydropads and following different flow paths at a given hydropad, are mutually similar (*Haggerty et al., in preparation; McKenna et al., in preparation*).

In general, geologic materials are heterogeneous, and the larger the region considered, the greater the degree of heterogeneity. σ_d is a measure of heterogeneity in mass transfer rate coefficients within the volume of rock sampled. σ_d thus increases with spatial scale as a result of an increase in the heterogeneity in rate coefficients encountered over the larger sampling volume. This occurs in a manner closely analogous to that in which macrodispersivity increases with spatial scale as a result of an increase in the heterogeneity in hydraulic conductivity encountered over the larger sampling volume (*Gelhar et al., 1985; Quinodoz and Valocchi, 1993*). At the smallest spatial scales (i.e., individual samples in the static diffusion experiments), mass transfer rates may vary considerably from one point in the formation to the next, but there is relatively little heterogeneity within each small sampling volume. At a larger spatial scale, a range of mass transfer rates - the point values found at the smaller spatial scale - will simultaneously exist within that sampling volume, resulting in an increase in σ_d . This corresponds to the bulk diffusion experiments. As the spatial scale continues to increase, a greater variety of mass transfer rates are encountered, leading to further increases in σ_d .

This corresponds to the field-scale tracer tests, although it should be noted that the increase in σ_d estimates for the field-scale experiments relative to those for the diffusion work may be partly attributable to the effects of slow advection. Unless large and abrupt changes in mass transfer characteristics are encountered, the increase in σ_d might be expected to level off, reflecting the fact that all mass transfer rates in the aquifer observable at the time-scale of the experiment have been sampled. This may account for the roughly logarithmic form of the relationship. Note that an analogous decrease in the rate of change of macrodispersivity with spatial scale also occurs at larger sampling volumes (*Gelhar, 1985*).

It would appear that the logarithmic form of the scaling relationship would permit a conservative extrapolation of σ_d to the regional-scale. For example, a continuous-source plume 50 m wide and 500 m long and distributed over the full 4.4 m thickness of the lower Culebra (for a total sampling volume of 110,000 m³, over 500 times that of the field-scale tests) gives, using a best-fit line to the data in Figure 27.a, an extrapolated σ_d of about 8. This value is not dissimilar to those found from a number of the field-scale tests. As a result, use of such roughly logarithmic spatial scaling relationships does not give radically large σ_d estimates.

However, applying these relationships at scales significantly larger than the field-scale requires that no major, large-scale changes in geologic properties is encountered by the expanding sample volume (see above). That is, the relationship must be valid for any suite of samples of different volumes from anywhere within that larger-scale region of interest. This is untrue. While no lab-scale data are available and it is not, therefore, possible to develop another scaling relationship, a number of SWIW and multiwell tracer tests at the H-11 hydropad (*Haggerty et al., in preparation; McKenna et al., in preparation*) have given values of σ_d significantly smaller than those from the field-scale at H-19. Clearly, the local degree of heterogeneity in mass transfer characteristics changes from one region in the Culebra to another.

It is possible, nonetheless, to hypothesize what effect this larger scale of variability might have by considering the simple case of advection of a solute plume in series through two adjacent regions with different mass transfer characteristics. From both theoretical considerations and scoping runs performed using a code capable of modeling one-dimensional advective-dispersive transport with multirate mass transfer (*Haggerty and Reeves, 1998*), it appears that: 1) the net effect of different μ_{dr} values across the two regions, but a shared σ_d value, is a bulk μ_{dr} value roughly equal to the average of the two individual ones and a bulk σ_d that is somewhat, but not drastically, increased; and 2) the net effect of a shared μ_{dr} value, but different σ_d values, is the original μ_{dr} value and an average of the two σ_d values. Thus, if a large plume were to transect both the H-11 and H-19 hydropads (tests from which have yielded similar values for μ_{dr} but different values for σ_d), the scaling relationships inferred from Figure 27.a would provide an overestimate of σ_d over that larger sampling volume. On the other hand, there may be other locations in the Culebra characterized by a higher degree of heterogeneity than seen at H-19; in that case, our scaling relationship would give an underestimate of the regional σ_d . Similarly, if other locations exhibit different field-scale μ_{dr} values (even if σ_d is identical to that at H-19), the regional value of σ_d extrapolated from this relationship would again provide an underestimate.

A corollary regarding the distinction between temporal and spatial scales is in order. In Section 2.1, we indicated that the rates of mass transfer estimated from experimental data may depend, in part, on the time-scale of the experiment. For a given velocity, the spatial-scale of an experiment clearly determines its time-scale. Insofar as the influence of Damkohler numbers upon mass transfer rate estimates are concerned, however, the controlling factor (all other things being equal) is the duration of exposure of a clean rock matrix to solute, or of a contaminated rock matrix to clean advecting pore water, relative to the time-scale of mass transfer. The spatial scale is only significant in that it determines, together with velocity, the ratio of these time-scales. All the

parameter estimates discussed in this section, however, were determined from experiments of roughly similar time-scales. For these experiments, spatial scale controls mass transfer parameter estimates by controlling the volume of aquifer sampled and, therefore, the degree of spatial heterogeneity in mass transfer characteristics encountered by the solute.

3.4.3 Suggestions for Future Laboratory-Scale Diffusion Work

Continued study of multirate diffusion processes at the laboratory-scale is desirable given the fundamental importance of these effects to both aquifer remediation and evaluation of the risk associated with hazardous waste repositories. Specific suggestions to be considered in future experimental design and modeling in the Culebra dolomite, which could also be used as a checklist for work in other geologic media, might include the following:

1) increase the dynamic range of the data to at least 2, or preferably 3 or more, orders of magnitude. Greater range in the mass ratio data (i.e., collection of data over a longer experimental duration) is desirable for any modeling effort, and is of particular significance to multirate modeling;

2) increase the number of samples in the study. The ability to reliably draw or dismiss correlations between mass transfer parameters and easily recognized or measured geologic properties of the samples, such as porosity and the degree of fracturing or vugginess, would be greatly improved if more samples were available. Moreover, by combining the mass ratio data from a greater number of samples in the manner described in Section 3.1 to form a bulk data set, a significantly larger-scale experiment may be simulated. In addition, if a sufficiently large number of samples were available, the sampling volume could be carefully controlled by varying the number of individual slabs included in the bulk data set. This would compliment efforts to identify and describe spatial scaling relationships;

3) perform diffusion experiments for samples from other hydropads. This would help to ascertain whether results from the study are generally applicable over the WIPP site. H-11 would be an appropriate choice, as parameter estimates from the static diffusion experiments could be compared to those obtained from multirate modeling of the field-scale tracer tests conducted at this hydropad;

4) measure the formation factor and construct one or more thin sections for each sample.

Comparison of detailed observations from thin section to estimated mass transfer parameters would be likely to greatly expand our understanding of the relationships between mathematical mass transfer models and observable geology. In addition, the details of the relationship between diffusion coefficients and formation factors are not fully understood. As a result, comparison of formation factors to mass transfer parameters measured for the same sample might enhance the ability to use electrical rock properties as an inexpensive and simple surrogate for laboratory diffusion experiments;

5) reduce experimental error by ensuring that a constant-concentration boundary condition is maintained, that gypsum dissolution does not occur, and that the sample is fully saturated with solute between the in- and out-diffusion experiments;

6) develop a method for calculating measurement error in the mass ratio data. This would permit the modeler to determine with certainty whether the modeling result is consistent with the data, and would also permit more accurate calculation of parameter estimation statistics.

4. REGIONAL-SCALE SIMULATIONS

4.1 General

The effects of multirate mass transfer upon solute transport at very large time- and spatial-scales, such as the 10,000 year period considered for WIPP certification and the approximately 3 km distance from the center of the WIPP site to its regulatory boundary, have been the subject of conjecture but remain unclear. In this second phase of the study, we address these issues by performing one-dimensional simulations of advective-dispersive solute transport in presence of a variety of mass transfer regimes.

Two approaches are used. First, a series of five deterministic scoping simulations are completed to evaluate the effects of the following mass transfer models upon breakthrough curves (BTCs) of both solute concentration and mass: 1) no mass transfer (A-D); 2) equilibrium mass transfer (LEA); 3) a single rate of diffusive mass transfer (SR); 4) a lognormal distribution of diffusion rate coefficients (MR); and 5) a similar multirate model wherein the geometric mean of the distribution is shifted significantly toward slower rates, in accordance with the hypothesis that mass transfer rates scale temporally (MR-S). These simulations are performed for transport distances of both 3000 m and 1 m for purposes of comparison.

Second, for each of these column lengths, four Monte Carlo simulations are performed: 1) single-rate diffusive mass transfer with statistically-described uncertainty in V_{pw} , the pore water velocity [L/T]; β_{tot} , the capacity coefficient; and D_e/a^2 , the diffusion rate coefficient (SR); 2) single-rate mass transfer with uncertainty only in D_e/a^2 (SR-MT); 3) multirate mass transfer incorporating uncertainty in V_{pw} , β_{tot} , the geometric mean (μ_{dr}) of the lognormal distribution of diffusion rate coefficients, and the standard deviation (σ_d) of the diffusion rate distribution (MR); and 4) multirate

mass transfer with uncertainty only in μ_{dr} and σ_d (MR-MT). This permits comparison of the consequences of the different mass transfer models in the presence of uncertainty in their parameterization, and also allows investigation the effects of variation in mass transfer rates and regimes to be compared with those due to uncertainty in the combination of Darcy velocity, advective porosity, and diffusive porosity.

For simplicity, D_e/a^2 (in the single-rate model) and μ_{dr} and σ_d (in the multirate model) will hereafter be collectively referred to as the mass transfer parameters. The pore water velocity and capacity coefficient will be referred to as flow parameters, although these parameters do, of course, control in part the nature of mass transfer experienced by an advecting solute plume.

4.2 Model Parameterization

4.2.1 Monte Carlo Input Distributions

Input distributions of V_{pw} and β_{tot} (Figure 29) were constructed from available distributions of travel time, advective porosity (θ_a), and diffusive porosity (θ_d) (Figure 28). The travel time distribution represents the time required for a particle of solute to travel an average distance of 3682 m within the Culebra dolomite in the absence of mass transfer and assuming an advective porosity of 0.16, and was provided by M. Wallace (*personal communication, 1998*). These travel times were calculated using a two-dimensional particle tracking groundwater flow code, for realizations of heterogeneous transmissivity fields developed using the pilot point method of *LaVenué et al. (1990)* and generated using the GRASP-INV code (*M. Wallace, personal communication, 1998; S. McKenna, personal communication, 1998*). The piece-wise linear travel time distribution was converted to a distribution of Darcy velocities, q , by dividing the travel distance of 3682 m by the travel time and multiplying by the advective porosity of 0.16 which was assumed in their simulations. A piece-wise

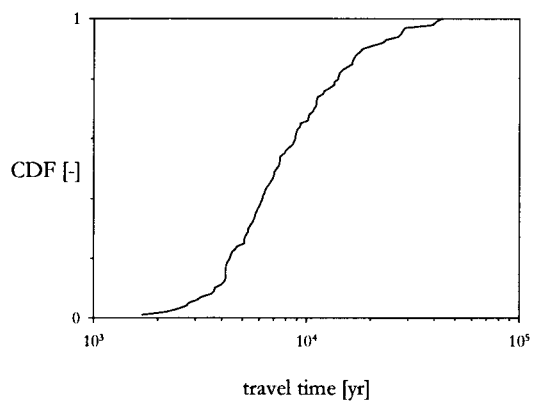


Figure 28.a

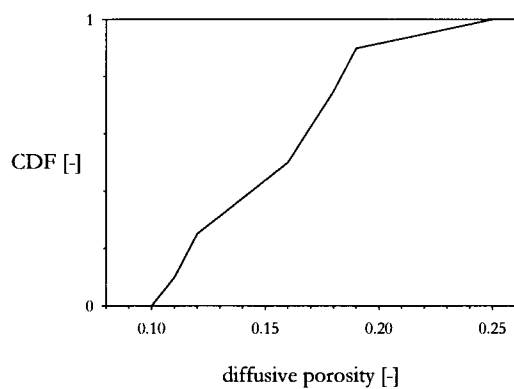


Figure 28.b

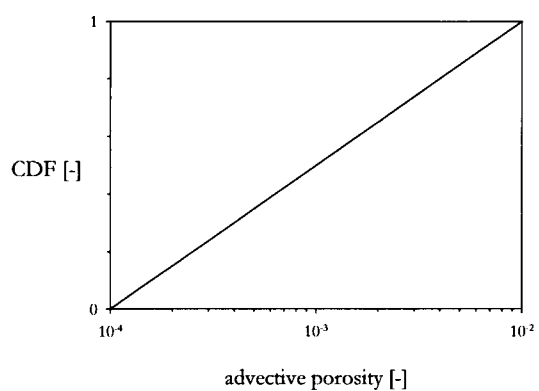


Figure 28.c

Figure 28: Indirectly utilized input distributions. Figure 28.a: travel time distribution (*M. Wallace, personal communication, 1998*). Figure 28.b: distribution of diffusive porosity (*Meigs and McCord, 1996*). Figure 28.c: distribution of advective porosity (*Meigs and McCord, 1996*).

Figure 29.a

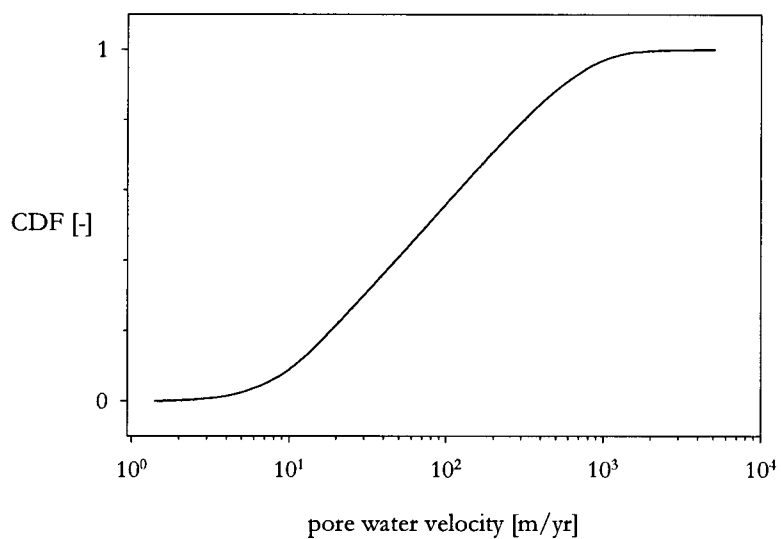


Figure 29.b

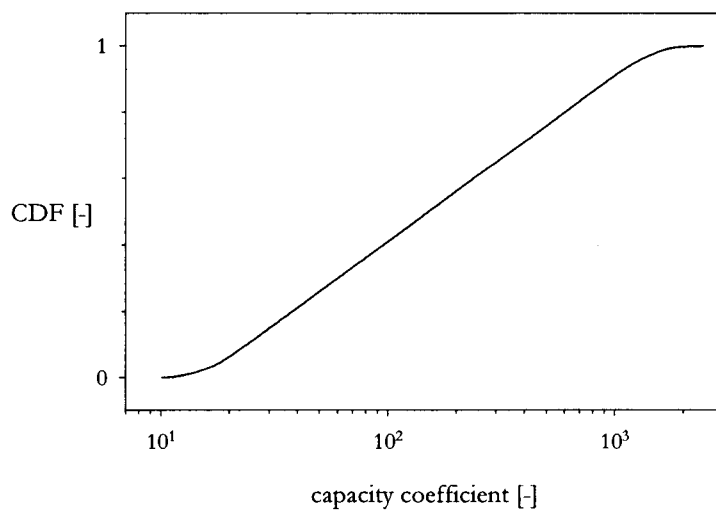


Figure 29: Flow parameter input distributions. Figure 29.a: pore water velocity distribution, calculated from distributions of travel time and advective porosity. Figure 29.b: distribution of capacity coefficient, calculated from advective and diffusive porosity distributions.

linear distribution of Culebra diffusive porosity and a log-uniform distribution of Culebra advective porosity, both developed by *Meigs and McCord (1996)*, were also used.

In a given Monte Carlo realization, single values of q , θ_a , and θ_d are independently and randomly drawn from their respective distributions. Corresponding values of V_{pw} and β_{tot} are then calculated for use in the transport simulation. Note that the distributions of V_{pw} and β_{tot} used in the simulations are not independent, as both are a function of θ_a . For Monte Carlo simulations in which only the mass transfer variables are treated stochastically (MR-MT and SR-MT), V_{pw} is set to 81.54 m/yr (the product of the 50th percentile values of q and θ_a) and β_{tot} is set to 160 (the quotient of the 50th percentile values of θ_d and θ_a).

The input distribution of μ_{dr} for the multirate simulations (MR, MR-MT) is constructed primarily from nine field-scale tracer tests conducted in the Culebra dolomite at two locations (*Haggerty et al., in preparation; McKenna et al., in preparation*). Field-scale estimates of μ_{dr} are used rather than those from the static diffusion work (Section 3) because they directly incorporate variability in the diffusion path length, and because they represent sampling volumes more similar to that of the regional-scale transport considered here. We use a uniform CDF to describe uncertainty in regional-scale μ_{dr} . This is the most appropriate distribution to use when little is known about the true distribution but minimum and maximum reasonable values of the random variable can be specified with some confidence (e.g., *Jensen et al., 1997*). The smallest estimated value of μ_{dr} estimated from field-scale tracers tests conducted in the Culebra, in units of $\ln(\text{yr}^{-1})$, is -0.372. The parameter estimation routine used to obtain this best-fit value also provides quantitative information regarding the degree of uncertainty associated with that estimate, expressed in terms of 68% and 95% confidence limits (± 1 CI and ± 2 CI, respectively). The -2 CI value corresponding to this minimum estimate of μ_{dr} is -1.51; this is the smallest possible value of μ_{dr} that can be interpreted from the

available tracer test data. Similarly, the +2 CI value corresponding to the largest estimated value of μ_{dr} from these field-scale experiments is 3.01; this is the largest possible value of μ_{dr} that can be interpreted from the available field-scale data. Comparison of lab-scale and field-scale analyses (Section 3) does not provide evidence of a systematic scaling of μ_{dr} with increasing sampling volume, so use of these field-scale estimates in regional-scale simulations is not likely to result in systematic error. We therefore use values of μ_{dr} of -1.51 and 3.01 as the upper and lower limits of the uniform distribution which, following the method of *Jensen et al. (1997)*, gives the expression for the CDF of μ_{dr} (Figure 30.a):

$$P(\mu_{dr}^* \leq \mu_{dr}) = \frac{\mu_{dr} + 1.51}{4.52} \quad (\text{Eqn. 38})$$

There are two important caveats to be made with regard to this input distribution for μ_{dr} . First, the field-scale tracer tests used to construct the CDF were conducted at only two sites. It is possible that tests performed at other locations on the WIPP site, through which regional-scale transport of solute might occur, could yield different values of μ_{dr} . However, the distribution we use is quite broad, incorporating two orders of magnitude variation in the mean rate of diffusion; this range seems likely to include most physically reasonable values of μ_{dr} that might be estimated from field-scale tests at other locations. Moreover, interpretations of lab- and field-scale analyses suggest that the increased heterogeneity in diffusion rates encountered by a solute plume as the transport distance (and hence sampling volume) increases is in part accounted for by increases in σ_d (Section 3; see also below, this section). Thus, variations in μ_{dr} from one field-scale location to the next will at least partially be absorbed by changes in σ_d .

Figure 30.a

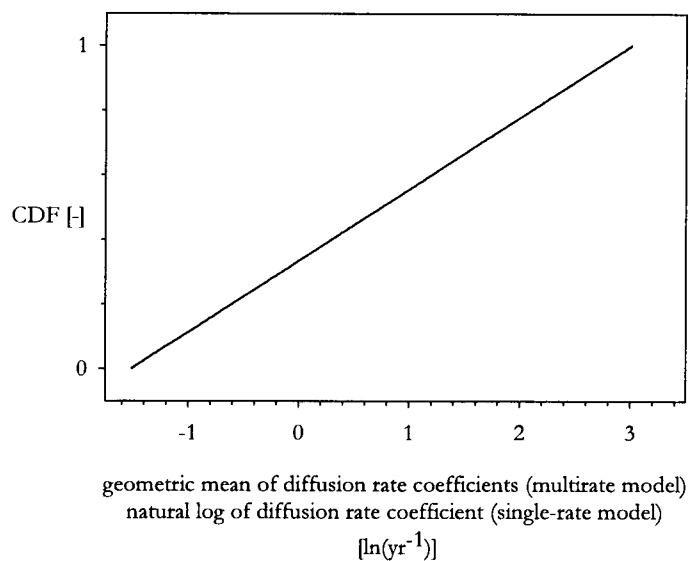


Figure 30.b

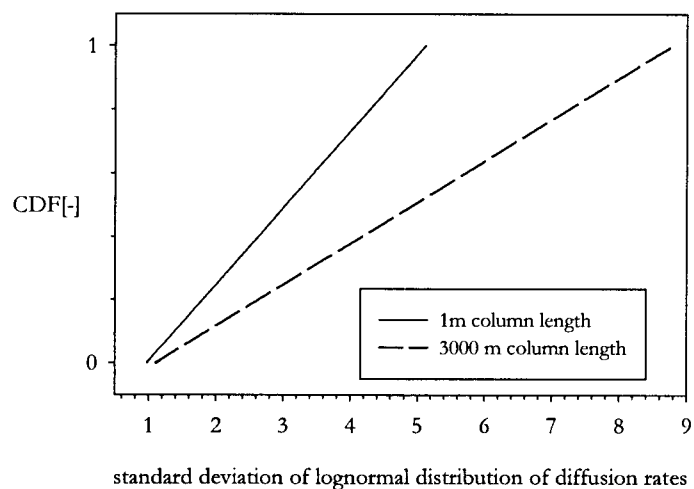


Figure 30: Mass transfer parameter input distributions. Figure 30.a: distribution of μ_d , the geometric mean of a lognormal distribution of D_e/a^2 . This also gives the input distribution of $\ln(D_e)$ used in the single-rate models. Figure 30.b: distribution of σ_d , the standard deviation of a lognormal distribution of D_e/a^2 . A wider σ_d distribution is used for the regional-scale simulations (see text for details).

Second, for a given pore water velocity, the duration of exposure of a rock matrix to solute is much longer for the regional-scale simulations than for the field-scale tracer tests. From the Damkohler number arguments presented in Section 2, it is clear that modeling of data obtained from an experiment conducted at the regional-scale would yield significantly slower mass transfer rate estimates than those that were conducted at the field-scale, provided that a distribution of rates is present. Thus, application of a μ_{dr} value estimated from a field-scale test may not be appropriate to simulations of regional-scale transport. However, no means currently exists for scaling multirate mass transfer parameters from one time-scale to another, and we omit these potentially very important effects from the distributions used in our Monte Carlo simulations. The consequences of time-scaling of μ_{dr} are, however, tentatively explored in the scoping runs.

The input CDF of μ_{dr} is also used to describe the uncertainty in D_e/a^2 for single-rate simulations (SR and SR-MT; refer again to Figure 30.a). That is, the geometric mean of the lognormal distribution of diffusion rate coefficients is used to describe the rate coefficient in a single-rate model, and uncertainty in the geometric mean is used to describe uncertainty in the single-rate D_e/a^2 . In a given Monte Carlo realization, a value of $\ln(D_e/a^2)$ is drawn randomly from the CDF of μ_{dr} ; $\exp[\ln(D_e/a^2)]$ is then used in the transport simulation. We take this approach to constructing a CDF of uncertainty in D_e/a^2 , rather than incorporating best-fit values of the diffusion rate coefficient estimated from the field-scale data using a single-rate model, for two reasons. First, single-rate fits to the tracer test data were generally very poor (*Haggerty et al., in preparation; McKenna et al., in preparation*). Second, the approach used permits more direct comparison of the effects of single-rate and multirate models. It should be noted that recent work (*Haggerty and Gorelick, 1995; Cunningham and Roberts, 1998*) suggests that if a distribution of rates is to be approximated by a single-rate model, use of the harmonic mean may be more appropriate than the geometric mean. However, use of either method requires that the true form of the distribution is known. In general, this is not the case; any continuous statistical distribution of diffusion rate coefficients is only an approximation to the actual

distribution in the rock. Moreover, the CDF of D_e/a^2 used in this study is very broad and therefore incorporates uncertainty that may arise from the issue of selecting the appropriate mean.

A uniform distribution is also used to describe uncertainty in σ_d for the multirate simulations (MR, MR-MT). Unlike μ_{dr} , however, σ_d increases with spatial scale, reflecting the incorporation of additional heterogeneities in pore geometry into the increasing sampling volume (Section 3). Thus, regional-scale values are likely to be larger than those obtained from the field-scale experiments. In addition, as the simulations are performed for transport distances of both 1 m and 3000 m, two input distributions for σ_d are therefore necessary. By fitting the steepest reasonable line to the plot of σ_d as a function of sampling volume given in Section 3 (Figure 27), we obtain:

$$\sigma_d = 4.446 + 0.4574 \ln(\text{sampling volume}) \quad (\text{Eqn. 39})$$

Extrapolating this relationship to a sampling volume of 13200 m³ (3000 m column length, 4.4 m Culebra thickness, and unit aquifer width in the one-dimensional simulation) gives a maximum reasonable value of σ_d of 8.79 at the regional-scale. Note that such a large value of σ_d effectively gives rise to a uniform distribution of diffusion rates. For a 1 m column length, the maximum predicted value of σ_d is 5.12. Eqn. 39 is based on a small number of data points obtained from only one location, and it is possible that field-scale σ_d values may be inflated relative to those from the lab-scale diffusion experiments due to the effects of slow advection, so this relationship can not be considered to be highly reliable and universally applicable over the WIPP site. Nonetheless, the values of σ_d predicted by Eqn. 39 are suitable for the heuristic purposes of the simulations performed here, and are used as upper limits on the distributions of σ_d . It should also be noted that a σ_d value of 8.79 is not much greater than the largest best-fit value obtained from the field-scale experiments (*Haggerty et al., in preparation*).

For a lower bound on the regional-scale CDF of σ_d , we use 1.11, the smallest estimated value from the field-scale experiments (*McKenna et al., in preparation*). Applying this low value at the regional-scale implies a very high degree of homogeneity in immobile zone pore geometry over the entire 3000 m transport distance and that, as a result, σ_d is both small and scale-invariant. Note that exploratory calculations (not included here) using a σ_d of approximately 1 for a 3000 m column length gave concentration and mass breakthrough curves indistinguishable from those predicted by a single-rate model (i.e., σ_d of 0), suggesting that if the minimum value of σ_d is small, the precise value is unimportant. The uniform CDF of σ_d at the regional-scale is then:

$$P(\sigma_d^* \leq \sigma_d) = \frac{\sigma_d - 1.11}{7.68} \quad (\text{Eqn. 40})$$

For the CDF of σ_d corresponding to a 1m column length, the lower limit is set to 0.976, the smallest value estimated from the bulk static diffusion experiments (Section 3). The CDF of σ_d used in these smaller-scale simulations is given by:

$$P(\sigma_d^* \leq \sigma_d) = \frac{\sigma_d - 0.976}{4.14} \quad (\text{Eqn. 41})$$

Plots of these CDFs are given in Figure 30.b.

For all simulations, dispersivity (α_L) is taken to be 5% of the travel distance, and the retardation factor for the advective porosity, R [-], is set to 1. A square wave input pulse at a normalized concentration of 1.0 was used for all simulations, with pulse lengths of 2000 yr for the 3000 m simulations and 0.5 yr for the 1 m simulations.

4.2.2 Deterministic Simulations

In all simulations, V_{pw} was set to 81.45 m/yr, the 50th percentile value from the distribution discussed in Section 4.2.1. For the A-D simulations (see Section 4.1 for nomenclature), β_{tot} was set to 0 and R was set to 1. In the LEA simulations, β_{tot} was again set to 0 but the retardation factor was calculated using:

$$R = 1 + \beta_{tot} \quad (\text{Eqn. 42})$$

For a β_{tot} of 160, the 50th percentile value discussed in Section 4.2.1, R is then 161. For the SR simulations, β_{tot} was set to 160, R was taken to be 1, and a diffusion rate coefficient of 2.117 yr⁻¹ was used, corresponding to the 50th percentile μ_{dr} value of 0.75 (see Eqn. 38). The same μ_{dr} value was applied in the MR simulations, but two values of σ_d were used. For the 1 m column, σ_d was set to 3.05, the 50th percentile value given by Eqn. 41; for a transport distance of 3000 m, σ_d was taken to be 4.95, the 50th percentile value given by Eqn. 40. This value is also similar to the arithmetic average of best-fit σ_d values (4.01) for all nine field-scale Culebra tracer tests at both WIPP locations (*Haggerty et al., in preparation; McKenna et al., in preparation*).

In the MR-S simulations, β_{tot} was again taken to be 160, R was set to 1, and σ_d was set to the values described above for the different column lengths. However, μ_{dr} was decreased substantially to investigate the potential effects of time-scaling of mass transfer parameters (see Section 4.1). A tentative empirical relationship between estimated first-order rate coefficients and experimental time-scale taken from a literature review was used as a very rough guide to the scaling of μ_{dr} , suggesting values of -3.06 for the 1m transport distance and -12.1 for the 3000 m column. However, no time-scaling relationship for multirate mass transfer parameters has yet been formally developed, and these

figures should be viewed as arbitrary values adopted only to explore the possible consequences of time-scaling. The very slow diffusion rates implied by such time-scaled distributions may correspond, for example, to diffusion into and out of low-permeability layers lying above and below that lower section of the Culebra in which advective transport takes place. Although some preliminary work consisting of performing parameter estimations on truncated data sets suggests that σ_d may increase with experimental duration (*Fleming, unpublished data, 1997*), this may in fact be reflective of variability in sampling volume and we assume here that σ_d does not scale with time.

Longitudinal dispersivity and solute input pulse durations for the deterministic simulations are identical to those used in the Monte Carlo runs (see Section 4.2.1).

4.3 Code Development

The scoping simulations were performed using STAMMT-L (Solute Transport And Multirate Mass Transfer, Linear coordinates; *Haggerty and Reeves, 1998*), a FORTRAN code which applies the multirate series approach of *Haggerty and Gorelick (1995)* to calculate concentration and mass BTCs for one-dimensional advective-dispersive contaminant transport in the presence of single-rate or multirate matrix diffusion. A FORTRAN code consisting essentially of STAMMT-L with pre- and post-processors (STAMMT-LMC; see Appendix 2) was written to perform the Monte Carlo simulations. A flow chart illustrating the basic steps involved in performing these simulations is given in Figure 31. Several thousand (5000 to 160,000) realizations were performed for a given Monte Carlo simulation. Output distributions were returned for six variables: the maximum normalized concentration in the BTC (C_{max}); the times required for 1% and 90% of the input solute mass to break through at the end of the column ($T_{M1\%}$ and $T_{M90\%}$, respectively); the mean solute arrival time (T_{MSA}); the standard deviation of the concentration BTC (σ_{BTC}); and the skewness of the concentration BTC (S_{BTC}).

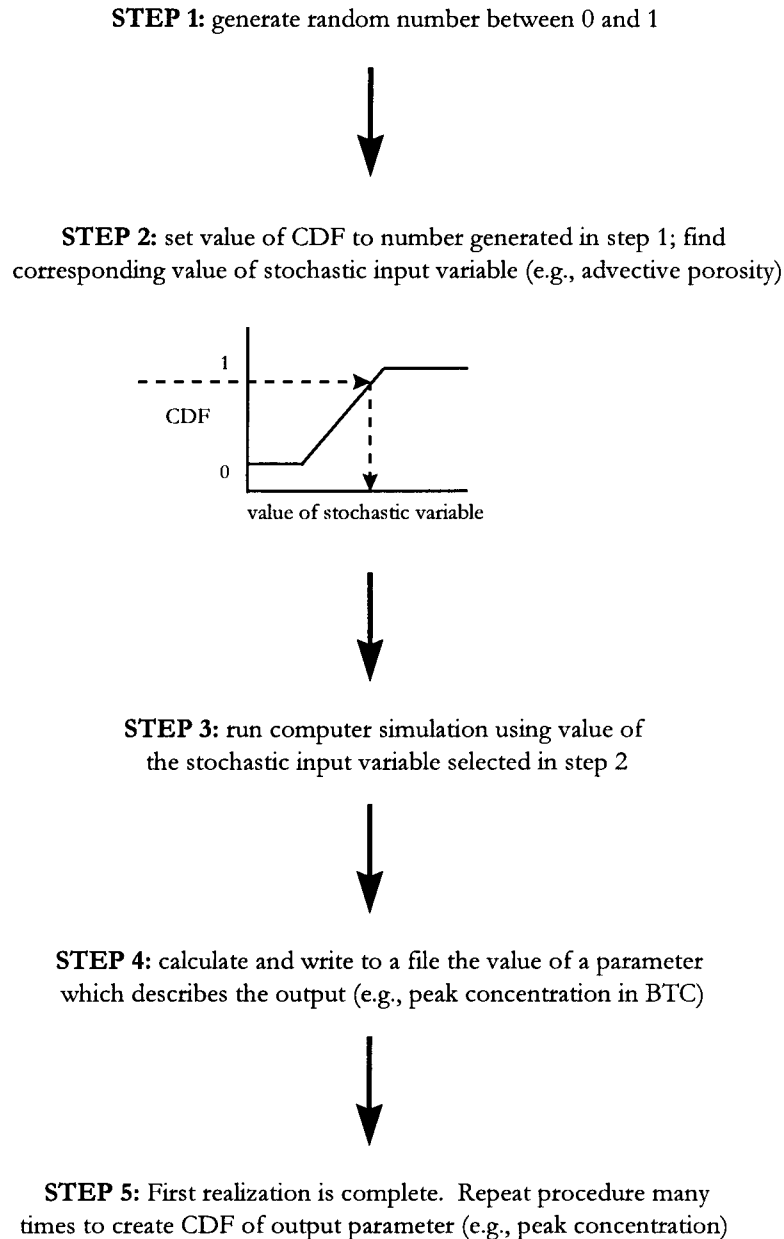


Figure 31: Flowchart delineating steps in performing Monte Carlo simulations. Note that if several stochastic input parameters are used, steps 1 and 2 are completed independently for each of those variables during a given realization. In the MR-MT simulations, for example, two random numbers are generated (step 1); one is used to determine a value of μ_d from its CDF for that realization, and the other is used to determine a value of σ_d (step 2). These values of μ_d and σ_d are then used in a single computer simulation (step 3).

Peak concentration is read directly from the concentration BTC. This variable is useful for determining, for example, whether a maximum contaminant level (MCL) will be exceeded at any time downgradient from a contaminant source. As the normalized mass BTC returned by STAMMT-L gives data points at specified times rather than at specified masses, $T_{M1\%}$ and $T_{M90\%}$ were found by linear interpolation between the times of arrival of normalized masses lying just above and below the desired values. A useful estimate of the time required for removal of most of the solute mass in a contaminated aquifer is given by $T_{M90\%}$, and $T_{M1\%}$, which gives a measure of the time required for a significant amount of solute mass to arrive at the end of the column, is of particular importance to addressing the risk associated with breaching of a hazardous waste repository.

Temporal moment methods were used to calculate T_{MSA} , σ_{BTC} , and S_{BTC} from concentration BTCs (e.g., *Harvey and Gorelick, 1995*). The n^{th} temporal moment, m_n , is given by:

$$m_n = \int_{t=0}^{t=\infty} t^n C(t) dt \quad \text{Eqn. 43}$$

where t is time and $C(t)$ is concentration. The temporal moments are calculated by numerical integration of the simulated BTCs of normalized concentration. As STAMMT-L output has been found to be free of numerical error for concentrations of greater than approximately 10^{-7} , simulated concentrations less than this value are omitted from the integration.

The mean arrival time of the solute at a given location (the end of the column, in our case) is given by the following relationship:

$$T_{MSA} = \frac{m_1}{m_0} \quad (\text{Eqn. 44})$$

Mean solute arrival time is clearly a very useful parameterization of the characteristics of solute transport. However, provided that some form of mass transfer occurs at the time-scale of the experiment (as opposed to pure advective-dispersive transport), the value of T_{MSA} is predicted from theory to be independent of the particular mass transfer regime invoked (e.g., *Valocchi, 1990; Harvey and Gorelick, 1995; Cunningham and Roberts, 1998*) and therefore should be the same for single-rate and multirate Monte Carlo simulations. The standard deviation of the concentration BTC is given by:

$$\sigma_{BTC} = \left[\frac{m_2}{m_0} - T_{MSA}^2 \right]^{1/2} \quad (\text{Eqn. 45})$$

and gives a measure of plume spreading, which may be due to nonequilibrium mass transfer or dispersion. The skewness of the concentration BTC is calculated from:

$$S_{BTC} = \frac{\left[\frac{m_3}{m_0} - 3 \frac{m_1 m_2}{m_0^2} + 2 T_{MSA}^3 \right]}{\sigma_{BTC}^3} \quad (\text{Eqn. 46})$$

and gives a measure of tailing in the breakthrough curve. A positive value indicates tailing, whereas a null value is indicative of a Gaussian BTC. Tailing is a well-recognized consequence of nonequilibrium mass transfer, but may also result from other mechanisms (Section 4.5.1). σ_{BTC} and, in particular, S_{BTC} are useful parameters for evaluating the effects of rate-limited mass transfer upon the efficiency of aquifer remediation.

4.4 Results

Concentration and mass BTCs from the deterministic scoping simulations are presented in log and arithmetic space in Figures 32 to 35. Arithmetic plots are generally more intuitive, whereas the log-space figures more effectively illustrate some of the effects of nonequilibrium mass transfer, such as late-time, low-concentration tails. Note that the LEA and SR models produce identical concentration and mass BTCs for a 3000 m column, and therefore can not be distinguished on the plots.

Output distributions from the Monte Carlo simulations are given in Figures 36 to 41. It was mentioned in Section 4.3 that multirate and single-rate models should provide identical values of T_{MSA} . The MR-MT and SR-MT simulations should, as a result, produce identical single-valued output distributions for a given column length. Similarly, the MR and SR output distributions of T_{MSA} should also be identical, although not single-valued as V_{pw} and β_{tot} (which help to control the value of T_{MSA}) are not held constant in these runs. However, Figures 37.b and 40.b suggest that for some small proportion of the total number of realizations, T_{MSA} for the multirate model is smaller than that for the single-rate model. The effect is most noticeable when comparing the SR-MT and MR-MT runs.

The divergence between the T_{MSA} distributions for the single-rate and multirate models is due to numerical error. By tracing individual realizations from the output distributions back to the corresponding input parameter values, it was determined that the small number of lower T_{MSA} values returned by the multirate simulations for both column lengths corresponded to realizations performed using some of the largest values of σ_d permitted by this variable's input CDFs. In addition, μ_{dr} values for these realizations tended to be small. For very large values of σ_d , tailing becomes extreme. This effect is exacerbated by small values of μ_{dr} , as a smaller proportion of the

Figure 32.a

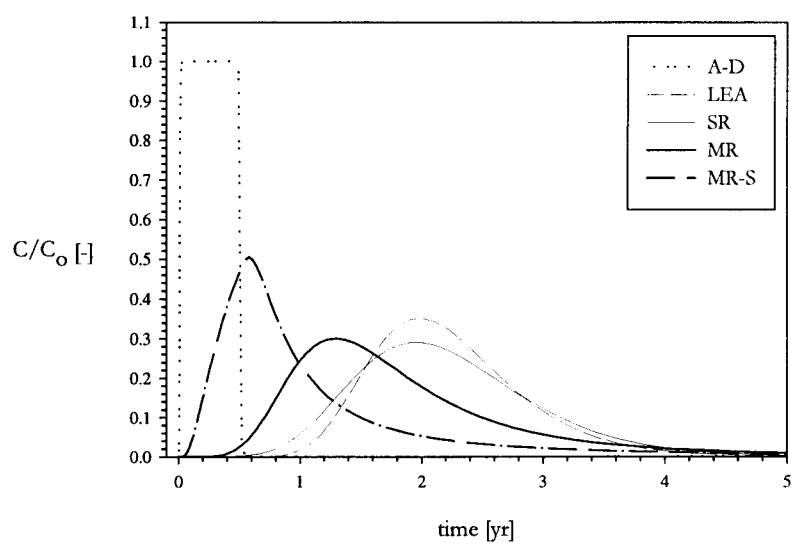


Figure 32.b

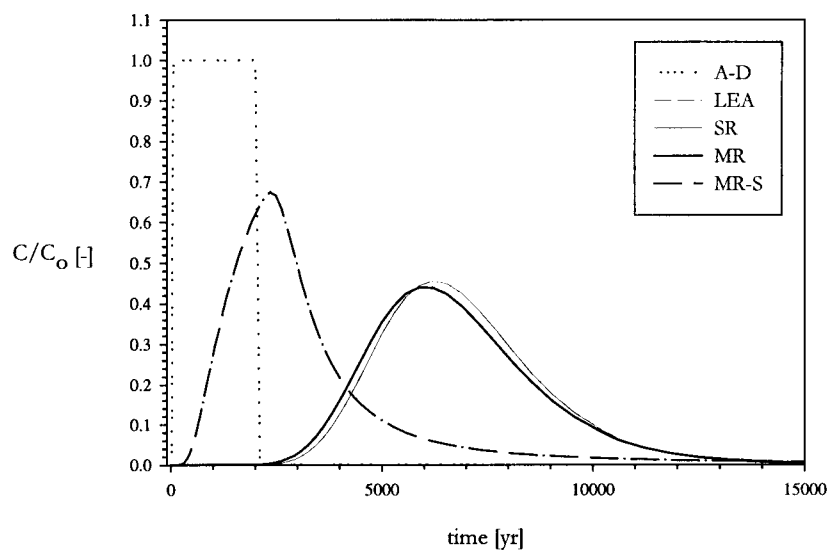


Figure 32: Arithmetic-space plots of concentration BTCs. Figure 32.a: 1 m column length. Figure 32.b: 3000 m column length.

Figure 33.a

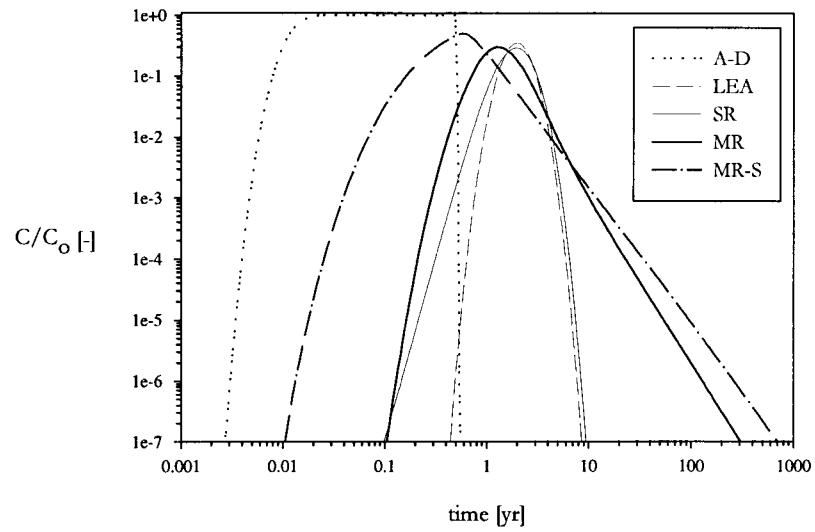


Figure 33.b

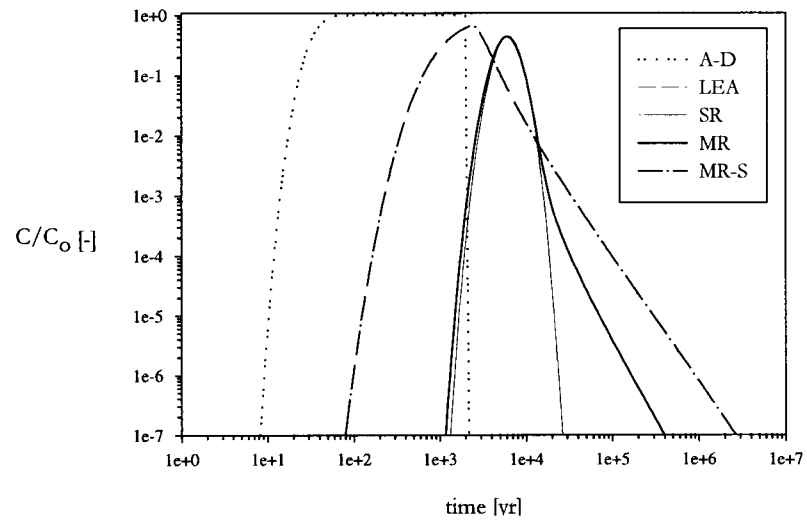


Figure 33: Log-space plots of concentration BTCs. Figure 33.a: 1 m column length. Figure 33.b: 3000 m column length.

Figure 34.a

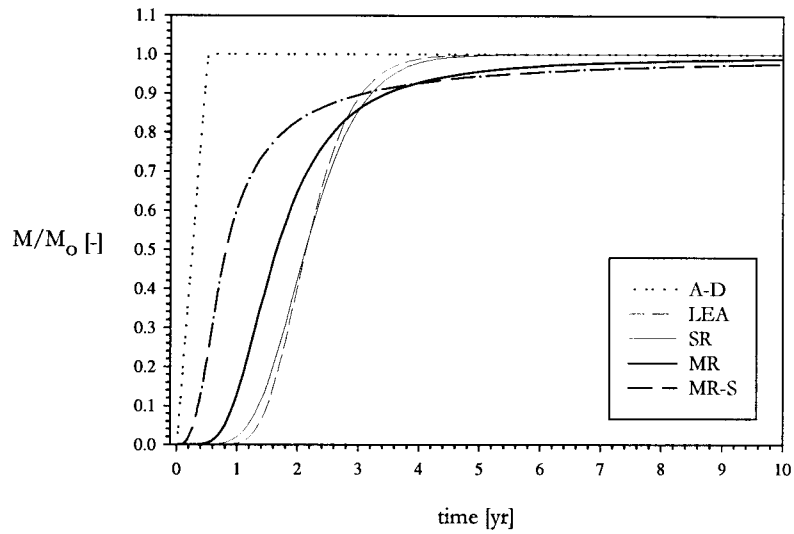


Figure 34.b

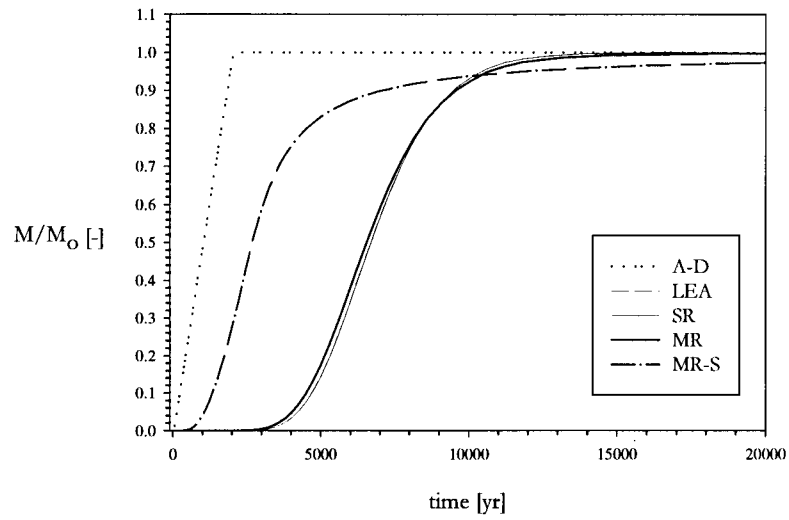


Figure 34: Arithmetic-space plots of mass BTCs. Figure 34.a: 1 m column length. Figure 34.b: 3000 m column length.

Figure 35.a

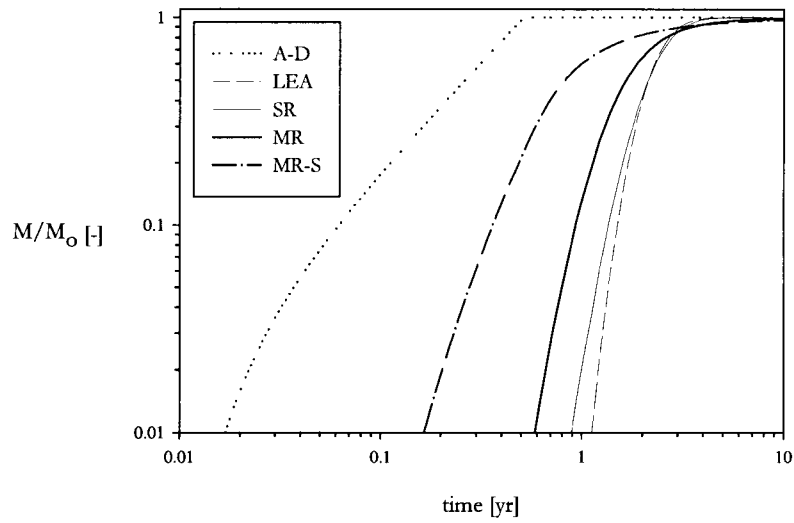


Figure 35.b

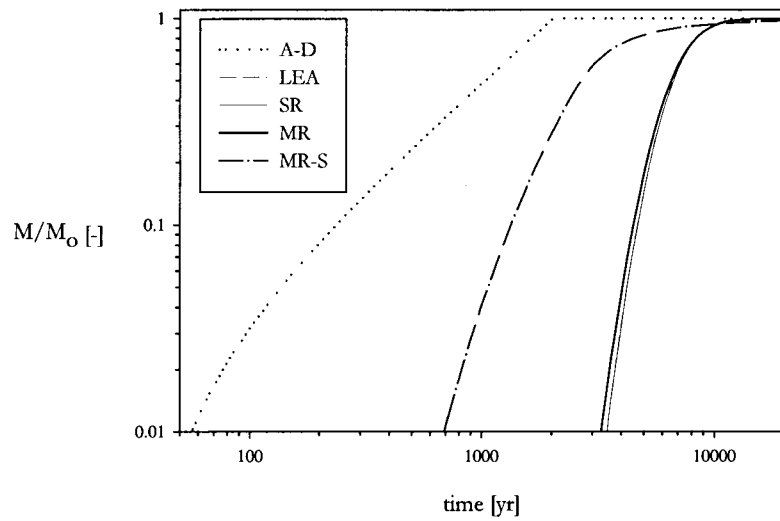


Figure 35: Log-space plots of mass BTCs. Figure 35.a: 1 m column length. Figure 35.b: 3000 m column length.

Figure 36.a

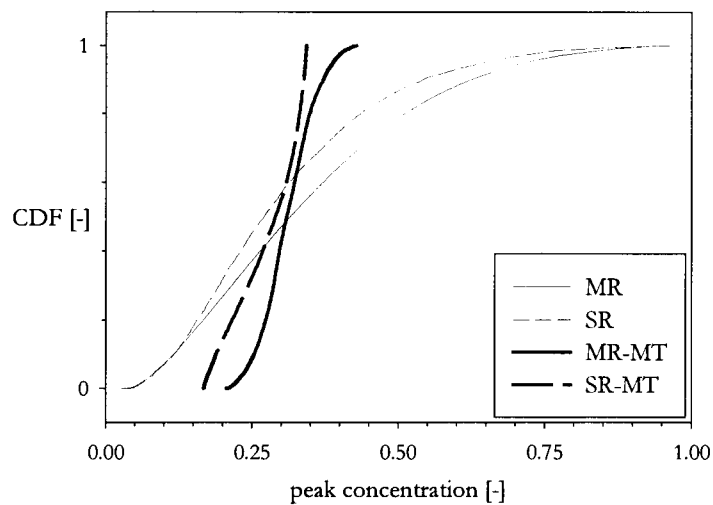


Figure 36.b

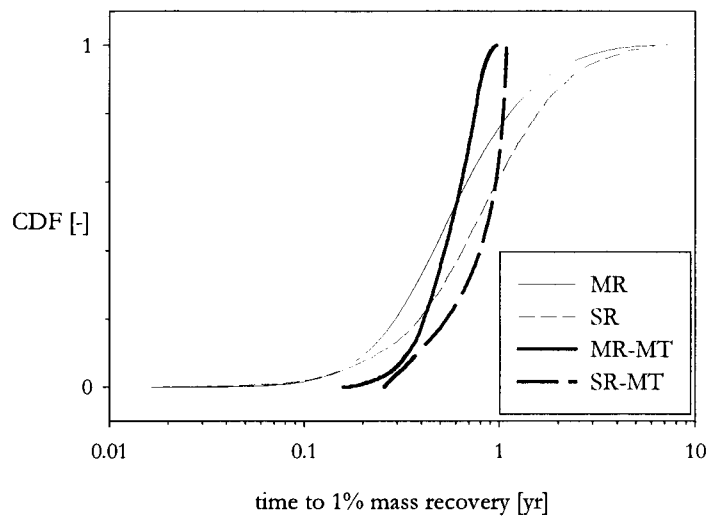


Figure 36: Output CDFs of C_{max} and $T_{M1\%}$, 1 m column. Figure 36.a: Peak concentration in concentration BTC, C_{max} . Figure 36.b: Time required for 1% of input mass to be removed, $T_{M1\%}$.

Figure 37.a

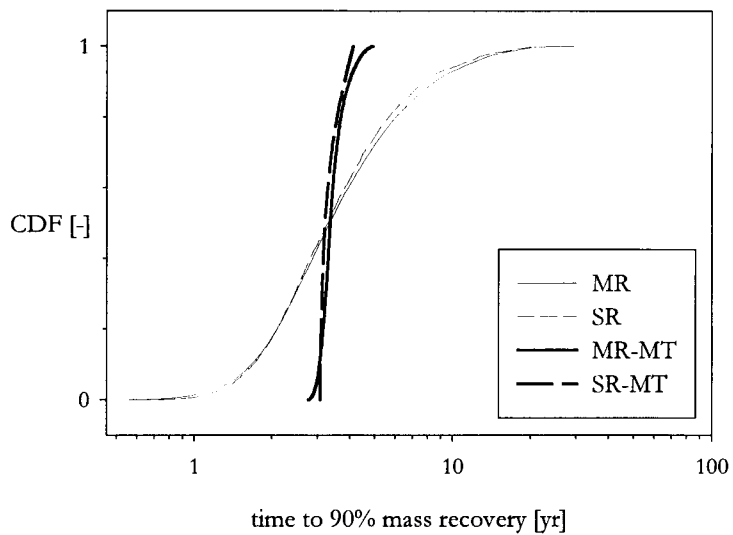


Figure 37.b

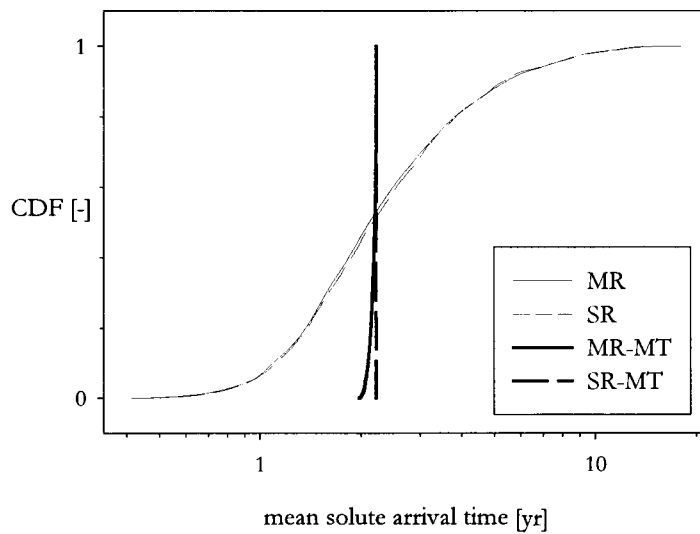


Figure 37: Output CDFs of $T_{M90\%}$ and T_{MSA} , 1 m column. Figure 37.a: time required for 90% of input mass to be recovered, $T_{M90\%}$. Figure 37.b: mean solute arrival time, T_{MSA} .

Figure 38.a

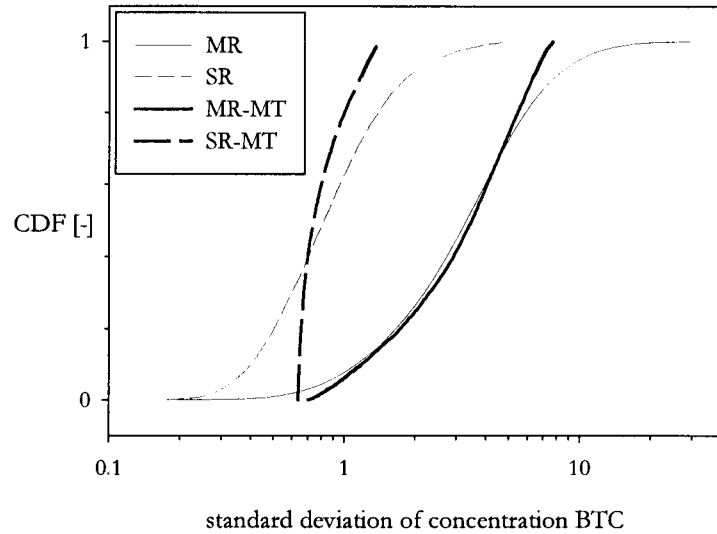


Figure 38.b

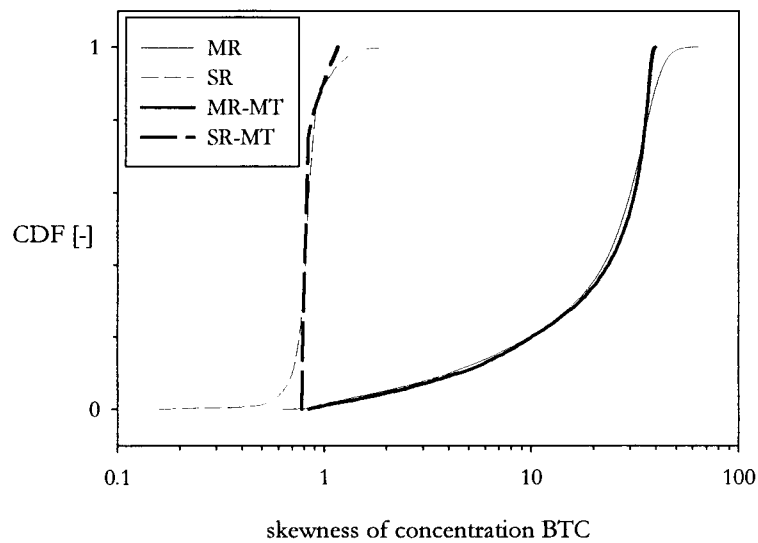


Figure 38: Output CDFs of σ_{BTC} and S_{BTC} , 1 m column. Figure 38.a: standard deviation of concentration BTC, σ_{BTC} . Figure 38.b: skewness of concentration BTC, S_{BTC} .

Figure 39.a

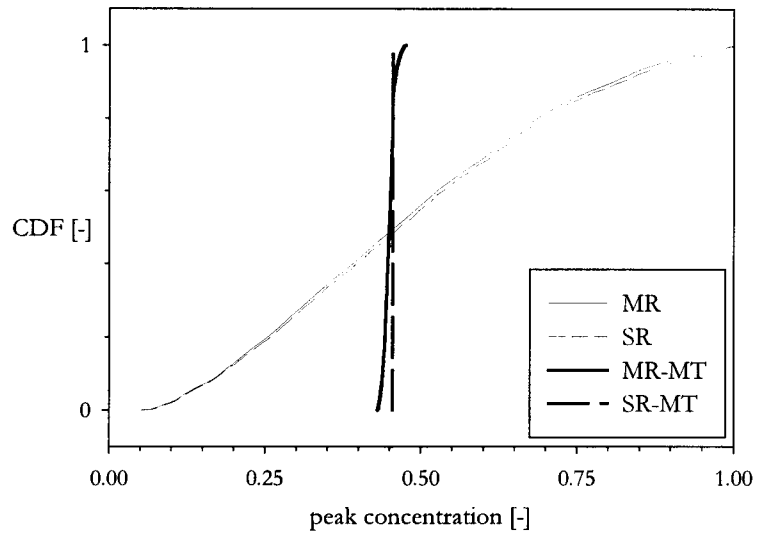


Figure 39.b

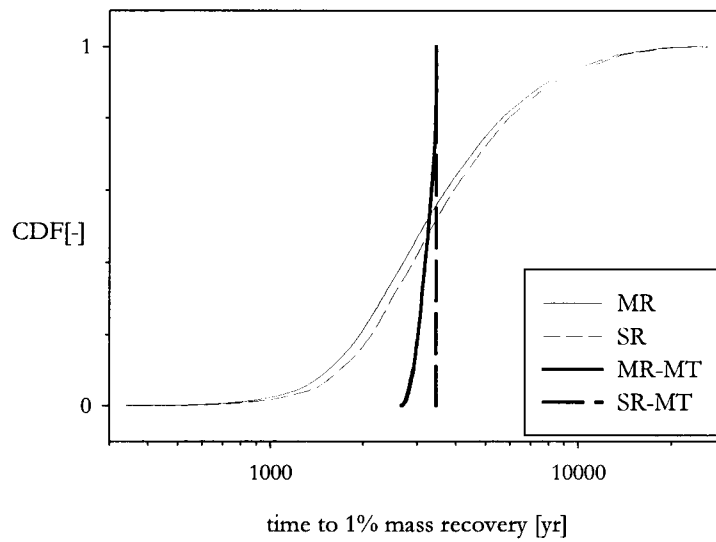


Figure 39: Output CDFs of C_{max} and $T_{M1\%}$, 3000 m column. Figure 39.a: Peak concentration in concentration BTC, C_{max} . Figure 39.b: time required for recovery of first 1% of input mass, $T_{M1\%}$.

Figure 40.a

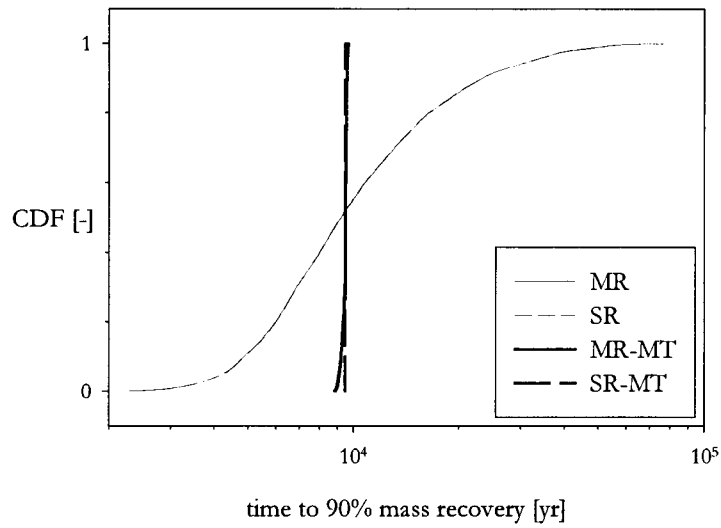


Figure 40.b

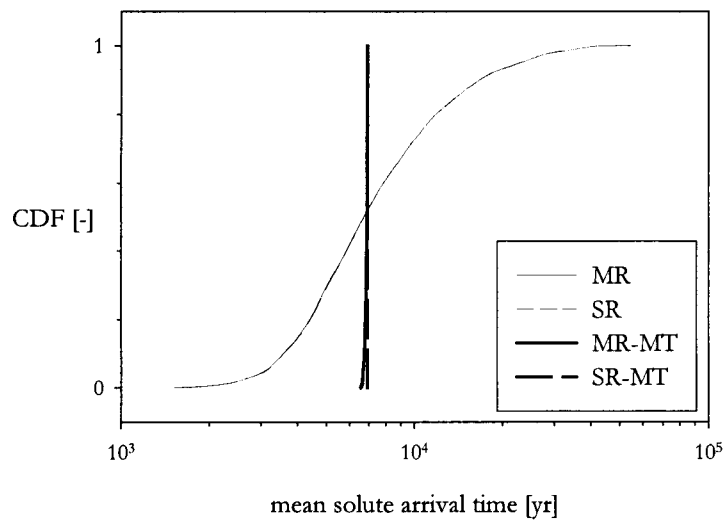


Figure 40: Output CDFs of $T_{M90\%}$ and T_{MSA} , 3000 m column. Figure 40.a: time required for recovery of 90% of input mass, $T_{M90\%}$. Figure 40.b: mean solute arrival time, T_{MSA} .

Figure 41.a

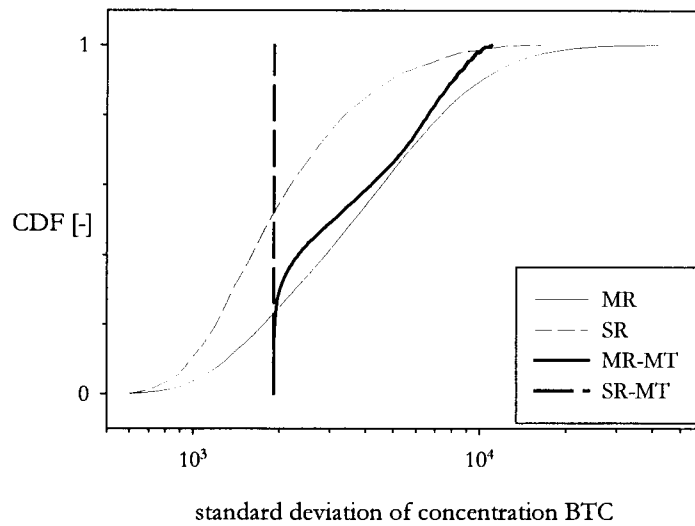


Figure 41.b

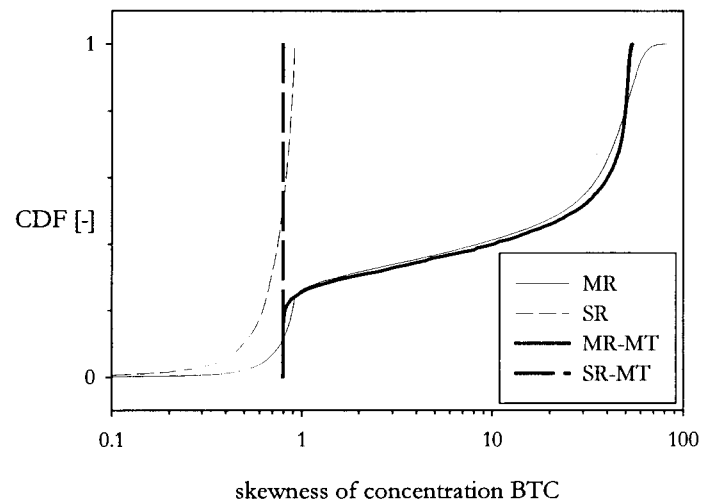


Figure 41: Output CDFs of σ_{BTC} and S_{BTC} , 3000 m column. Figure 41.a: standard deviation of concentration BTC, σ_{BTC} . Figure 41.b: skewness of concentration BTC, S_{BTC} .

distribution of diffusion rates is at equilibrium (see Sections 4.5.1 and 4.5.2 for discussion of these effects). The net result is that a comparatively large proportion of the plume mass lies within extensive tails of very low concentration. However, the concentration BTCs were truncated prior to numerical integration for values of normalized concentration less than 10^{-7} (Section 4.3). Temporal moment calculations for realizations with very large σ_d values and slow mean diffusion rates are consequently beset by a small degree of numerical error. A number of conventional transport simulations using such values for the multirate mass transfer parameters, coupled with manual calculations of the corresponding temporal moments, revealed that by lowering the cutoff concentration in the numerical integrations this effect is minimized and the values of T_{MSA} converge upon those for the other realizations. This sensitivity to imperfections in the concentration BTC is of little significance to the present work, but it does suggest that use of temporal moment methods to analyze experimental data - which are rarely collected to normalized concentrations as low as 10^{-7} , and which are often subject to appreciable measurement error - might be problematic.

4.5 Discussion

4.5.1 Deterministic Simulations

For a 1 m column length (Figures 32.a, 33.a, 34.a, and 35.a), solute is predicted by the A-D model to arrive at the end of the column very quickly; all input mass is recovered by 0.6 yr. In addition, the concentration BTC shows little dispersion, appearing very similar in form to the input pulse. This is due to the combination of short travel time and long pulse duration. For the case of no mass transfer, the standard deviation of a concentration BTC is given by (e.g., *Domenico and Schwartz, 1990*):

$$\sigma_{BTC} = \frac{2D_L t}{V_{pw}^2} \quad (\text{Eqn. 47})$$

where D_L is the longitudinal dispersion coefficient [L^2/T] (note that in the case of equilibrium mass transfer, V_{pw} is scaled by the retardation factor). As the time-scale is small and velocity is large, spreading of the plume is marginal. Moreover, as the time-scale of the experiment is almost equal to the duration of the square-wave input pulse, the small amount of dispersion that takes place results in little qualitatively apparent alteration of the plume shape from a square wave to a more Gaussian form.

In contrast, the LEA model for the 1 m column (Figures 32.a, 33.a, 34.a, and 35.a) predicts that solute arrives much more slowly (full mass recovery does not occur until 5.5 yr). Additionally, a much higher degree of dispersion is observed in the shape of the BTC in spite of the fact that the transport distance is identical to that of the A-D model described above. Eqn. 47 reveals this is due to the fact that the time required for solute to pass through the column is approximately an order of magnitude larger and the effective linear velocity, V_{pw}/R , is approximately two orders of magnitude smaller.

Moreover, tailing is observed in the concentration BTC for the LEA model. Such tailing is often taken to be an indication of the presence of rate-limited mass transfer, but this model invokes only equilibrium processes. Using temporal moment methods, *Valocchi (1985)* demonstrated that for a Dirac or pulse input, tailing is present in any arithmetic-space plot of a concentration BTC when the dispersion coefficient is large relative to the pore water velocity and the length scale of the experiment, in spite of the fact that the corresponding concentration profile is symmetric. A more intuitive understanding of this phenomenon may be obtained by considering macrodispersion to be a

simple measure of heterogeneity in hydraulic conductivity (e.g., *Quinodoz and Valocchi, 1993*). In this case, our results are simply reflective of the well-known fact that heterogeneity in conductivity can also result in skewing of the concentration BTC (e.g., *Li et al., 1994*). In addition, the inherent asymmetry of concentration BTCs in the presence of significant dispersion is suggested by Eqn. 47. Consider for simplicity a Dirac input pulse of solute, as in this case all mass initially enters the formation simultaneously. As it travels through the aquifer, this Dirac pulse will disperse; again for simplicity, let us assume that this results in a symmetric, Gaussian plume. Then allow the plume to travel farther. As spreading of the plume is a function of time (Eqn. 47), it follows that the later-arriving half of an initially symmetric plume will have undergone more dispersion by the time it reaches a given observation point some distance downgradient than its earlier-arriving half, resulting in tailing. Nonequilibrium mass transfer processes, then, simply give rise to a (potentially much) greater degree of tailing than would be seen otherwise.

The LEA model gives the slowest initial arrival of mass at the end of the 1m column of all the regimes considered because at equilibrium, all solute in the plume experiences mass transfer, effectively slowing the rate of advective-dispersive transport by a factor of 161 (the retardation factor used; see Section 4.2.2). However, the time required for recovery of 90% or more of the solute mass is shortest of all the models other than pure advective-dispersive transport, as mass is transferred from the matrix back into advective pathways instantaneously following passage of the input pulse.

For the 1 m column, the SR simulation yields concentration and mass BTCs similar but not identical to those from the LEA run (Figures 32.a, 33.a, 34.a, and 35.a). This result is consistent with a calculated DaI number of 12.5 for the parameters used, which suggests that mass transfer is rate-limited but not far from equilibrium. The initial arrival of solute occurs sooner than for the LEA model, which appears to be a frequent effect of rate-limited mass transfer (e.g., *Valocchi, 1985*). This is because the time-scale of mass transfer is comparable to that of solute transport across the

column: slower (rate-limited) matrix diffusion is less efficient than instantaneous mass transfer at removing mass from the mobile zone over the time available. However, greater tailing is observed in the concentration BTC and the time required for all mass to be recovered is longer, as the solute requires some finite amount of time to diffuse back out of matrix after the injection pulse has passed. Maximum concentration is lower than that seen in the LEA simulation (see also *Valocchi, 1985*) because mass has been shifted away from the peak to both the leading edge and tail of the plume. The combination of increased tailing and earlier initial solute arrival also results in increased longitudinal spreading of the plume. This effect was termed kinetic dispersion by *Quinodoz and Valocchi (1993)* and is clearly visible, for example, in the field data presented by *Roberts et al. (1986)*.

The MR simulation for the 1m column length shows a significantly faster initial breakthrough than that predicted by either the LEA or SR models (Figures 32.a, 33.a, 34.a, and 35.a). Higher degrees of tailing and dispersion are also observed, which are consistent with theoretical considerations (e.g., *Valocchi, 1990; Harvey and Gorelick, 1995; Cunningham and Roberts, 1998*). Late arrival of 90% or more of total mass is also seen. The time required for 99% of the input mass to be recovered is approximately 11.2 yr, about twice as long as for the LEA and SR models, and well over 100 yr is required for full mass recovery. A multirate model thus affects the concentration history in a manner qualitatively similar to, but more pronounced than, a single-rate regime.

Given that the SR simulation uses a rate identical to the geometric mean of the multirate distribution used in the MR simulation, and that this rate is observed to lead to near-equilibrium mass transfer for a 1 m column length (see above), diffusion rates in the multirate distribution faster than the mean are probably at or near LEA. Thus, some portion of the matrix porosity experiences instantaneous diffusion. However, the lognormal distribution used in this model is heavily skewed toward slow diffusion rates. Very slow rates of mass transfer imply that relatively little mass is removed from the advective porosity over the time-scale of the experiment. That is, such a

substantial proportion of the matrix operates at such slow diffusion rates that the total capacity coefficient is effectively reduced - some portion of the matrix porosity does not appear, from the plume's point of view, to exist. This leads to faster initial mass recovery. What mass is removed, however, is then returned to the mobile zone very slowly, resulting in extensive tailing and slow recovery of the full input mass. Peak concentration is higher than seen in the SR simulation because, although some mass is shifted into the tail, a substantial proportion effectively bypasses the mass transfer process and is not shifted away from the center of the plume. Redistribution of mass to the front and rear of the plume also results in the observed increase in dispersion relative to the single-rate model.

We turn now to an evaluation of the potential effects of time-scaling of μ_{dr} . The MR-S model predicts faster initial solute arrival at the end of the 1m solute column than seen with any other model incorporating mass transfer, but extreme tailing is also observed (Figures 32.a, 33.a, 34.a, and 35.a). Specifically, mass breakthrough is much faster relative to the other models for up to approximately 95% recovery and is then far slower, with 99% mass recovery not occurring until about 21 yr and full mass recovery occurring only after several hundred years. The explanation for this behaviour is similar to that for the distinctions between the SR and MR models, except that here the distribution of diffusion rate coefficients is shifted several orders of magnitude toward slower rates. As a result, it is unlikely that any of the rates are at LEA, a larger proportion of the solute in the advective porosity effectively bypasses mass transfer processes over the time-scale of the experiment, and what mass transfer occurs does so at very low rates, resulting in extremely slow return of solute to the advective pathways. The much higher observed peak concentration results from the fact that a sizable portion of the plume mass is travelling through the formation without being substantially affected by mass transfer.

Results of simulations conducted for a column length of 3000 m are qualitatively very similar to those for a 1 m travel distance, with two important exceptions (Figures 32.b, 33.b, 34.b, and 35.b). First, the concentration and mass BTCs given by the SR and LEA simulations are identical. This suggests that for the larger transport distance, the diffusion rate coefficient used in the SR model results in instantaneous mass transfer. This is consistent with the calculated DaI number of 3.76×10^4 , which is far in excess of the value of approximately 100 at which rate limitations no longer arise.

Second, results from the MR model are much more similar to those from the SR and LEA models. Although the distribution of diffusion rates used in the 3000 m simulation is broader (Section 4.2.2), the time-scale of the experiment has increased sufficiently relative to the time-scales of mass transfer described by the multirate distribution that a larger proportion of the rates are effectively at equilibrium. Thus, the multirate model more closely approaches the SR and LEA models, both of which are at equilibrium. More importantly, the rates of mass transfer lying at the slow end of the lognormal distribution and to which the distribution is heavily skewed grow more comparable to the time-scale of transport over a 3000 m distance. As a result, it is likely that no portion of the solute mass is passed through the system without encountering mass transfer processes, and the faster initial solute arrival seen for the MR model in the 1 m simulation is no longer apparent. Nonetheless, a large degree of tailing is still seen in the concentration BTC, reflecting the fact that much of the multirate distribution remains in the domain of nonequilibrium mass transfer.

4.5.2 Monte Carlo Simulations

In general, comparison of the SR and MR CDFs in Figures 36 through 41 to those from the SR-MT and MR-MT simulations indicates that for most of the output variables, the effects of variability in flow parameters overshadow those of uncertainty in the mass transfer parameters. This is to be expected, as the effective advective velocity of the plume is controlled largely by the pore

water velocity and the capacity coefficient, which determines the total amount of mass transfer that is capable of taking place and, therefore, the degree of retardation of the plume. Nonetheless, the effects of variation in mass transfer parameters are significant, particularly with respect to the amount of spreading and tailing in the concentration BTC.

For a 1 m column, peak concentrations in the concentration BTC are consistently somewhat lower for the SR-MT model than for the MR-MT simulations, which is consistent with the results from the scoping runs (Section 4.5.1). The difference between the models remains significant in the presence of uncertainty in V_{pw} and β_{tot} . For both mass transfer models, the distribution is fairly wide, indicating that the values of the mass transfer parameters are a significant control over observed C_{max} . For a 3000 m column length, however, maximum concentrations are similar for the two mass transfer models considered, which is again consistent with the results and interpretations of the scoping runs. The distribution of C_{max} is very narrow for the regional-scale MR-MT simulations, and is single-valued for the SR-MT run. This suggests that the values of the mass transfer parameters, regardless of the model used, are not critical for prediction of maximum concentrations at longer time-scales. This is only true, however, if time-scaling of the mass transfer parameters is not significant, as indicated by the large increase in peak concentration given by the MR-S scoping simulation (Section 4.5.1).

For a 1 m column length, $T_{M1\%}$ occurs significantly sooner for the multirate model than for the single-rate model, due to the earlier initial solute breakthroughs seen in Section 4.5.1. The same is true for a 3000 m transport distance, but the effect is more subtle. However, note that this still results in a difference in $T_{M1\%}$ between the single-rate and multirate models of several hundred years. The effect remains when uncertainty in the flow parameters is present. The $T_{M1\%}$ distributions are fairly broad in the case of a 1 m column for both mass transfer models, but the distribution predicted by the MR-MT simulation at 3000 m is very narrow and the distribution given by the corresponding

SR-MT run is single-valued. This suggests that selection of correct parameter values for a given mass transfer regime is important at short time- and space-scales, but of less significance at larger scales. Again, this is true only if μ_{dr} does not scale with experimental duration: the MR-S scoping simulation for a 3000 m column length (Section 4.5.1) shows anomalously fast recovery of the first 1% of input mass.

The $T_{M90\%}$ distributions are very similar for the single-rate and multirate models. This is seen for both 1 m and 3000 m column lengths. Although the more extensive tailing resulting from multirate mass transfer might be expected to give rise to larger $T_{M90\%}$ values, concentrations in the tail are low and represent a small proportion of the total mass. However, $T_{M90\%}$ does occur slightly sooner at 1 m for the single-rate model than for the multirate simulations because differences between the mass transfer models are greater at the smaller time-scale (Section 4.5.1). The $T_{M90\%}$ distribution is narrow at both column lengths for MR-MT and SR-MT, suggesting that $T_{M90\%}$ is insensitive to the values of the mass transfer parameters, as only a small proportion of the total mass is carried in the extended concentration tail predicted by either model. Nonetheless, the potential for time-scaling of μ_{dr} may again play an important role. As shown in Section 4.5.1, time to 90% mass recovery occurs significantly sooner for the MR-S simulation than for any other mass transfer model considered, and time to greater than 95% mass recovery occurs much more slowly.

The T_{MSA} distributions for a given column length are the same for both models and independent of the values of the mass transfer parameters within the numerical capabilities of the code, as expected (see Sections 4.3 and 4.4). The mean solute arrival time is thus controlled by the effective advective velocity (i.e., the combination of pore water velocity and capacity coefficient). Unlike the Monte Carlo results for the other output variables considered, this result was also confirmed to hold true within the numerical capabilities of the code in the case of time-scaling of μ_{dr} .

Spreading of the concentration BTC is far greater for the multirate model than for the single-rate model at both column lengths, which is also consistent with theoretical calculations (e.g., *Valocchi, 1990; Harvey and Gorelick, 1995; Cunningham and Roberts, 1998*). This reflects the fact that in the multirate model, tailing is more severe (corresponding to the presence of slower rate-limited diffusion than seen in the single-rate model), but some mass also passes through the system more quickly (corresponding to very slow diffusion rates, which are not operative over the time-scale of the experiment). This leads to increased spreading of the plume. For the 1 m transport distance, comparison of the MR-MT and SR-MT distributions to those from the MR and SR runs reveals that σ_{BTC} is controlled largely by the values of the mass transfer parameters rather than the flow parameters, particularly in the case of multirate diffusion. Uncertainty in the multirate parameters (MR-MT) also gives rise to a greater degree of potential variability in σ_{BTC} than uncertainty in the single-rate parameter (SR-MT).

Similar behavior is seen for a transport distance of 3000 m, but the σ_{BTC} distribution predicted by the SR-MT simulation is single-valued. This indicates that at the regional-scale, spreading of the concentration BTC is independent of the value of the diffusion rate used in the single-rate simulation, implying that the system is at equilibrium for all reasonable values of this parameter. This is consistent with the results of the deterministic simulations at 3000 m (Section 4.5.1), and with the fact that the output distributions for all other variables are also found to be single-valued for the regional-scale SR-MT simulations. That the MR-MT simulations continue to give rise to broad output distributions for this and other variables illustrates that the distribution of diffusion rates in the multirate model is generally not at equilibrium at the regional-scale. However, the CDF predicted by the MR-MT simulations does become single-valued and equal to that given by the SR-MT simulations for small values of σ_{BTC} . This region of the CDF was found to correspond to small values of σ_d and large values of μ_d . This indicates that at the regional-scale, for a fast, narrow distribution of diffusion rates, equilibrium is indeed reached by the entire multirate distribution (or

some dominant portion of it) and the effects of multirate mass transfer could simply be accounted for by use of the conventional advective-dispersive equation with the appropriate retardation factor.

The distribution of σ_{BTC} at both scales in the presence of variability in flow parameters (MR and SR runs) is observed to be wider than that predicted by the MR-MT and SR-MT simulations, because β_{tot} and V_{pw} control the duration of the experiment and therefore lead to further increases or decreases in the degree of dispersion beyond those resulting from variability in the mass transfer parameters alone (Eqn. 47). If time-scaling of μ_{dr} occurs, σ_{BTC} for either column length would increase accordingly due to both increased tailing and earlier initial solute breakthrough (Section 4.5.1)

Values of S_{BTC} given by the multirate simulations are greater than those predicted by a single-rate model, again consistent with theoretical considerations. Comparison of the MR and MR-MT simulations shows that in a multirate model, S_{BTC} is dominated by the mass transfer parameters rather than the flow parameters at both spatial scales, and the broadness of the distributions indicates that S_{BTC} is sensitive to the values of those parameters. The distribution of S_{BTC} is again single-valued for the SR-MT simulation at 3000 m because mass transfer is not rate-limited and the value of D_e/a^2 therefore does not affect the skewness, or any other properties, of the concentration BTC. The aforementioned general sensitivity of S_{BTC} to multirate mass transfer parameters, and the fact that the 3000 m, MR-MT CDF becomes single-valued and equal to the SR-MT CDF for small values of S_{BTC} (corresponding again to large values of μ_{dr} and small values of σ_d), together show that the multirate distribution is in most cases not at equilibrium at the regional-scale, but LEA is indeed attained for fast, narrow rate distributions.

As was the case with σ_{BTC} , a somewhat broader distribution of S_{BTC} is found when variability in flow parameters is incorporated into the simulations, because this results in variation in the

duration of transport and therefore the degree of tailing seen in the concentration BTC due to dispersion (see Section 4.5.1). If time-scaling in μ_{dt} occurs, skewness should increase significantly to reflect the greater degree of tailing (Section 4.5.1).

5. CONCLUSIONS

A range of effective diffusion coefficients, D_e , is implied by the high degree of pore-scale heterogeneity observed in core samples of the Culebra (dolomite) Member of the Rustler Formation, NM. Earlier field-scale tracer tests have suggested significant heterogeneity in diffusion rate coefficients (the combination of D_e and matrix block size); however, it has not been possible to separate the contribution to variability from each of the two parameters. In addition, the effects of such multirate matrix diffusion processes over large time- and space-scales, and of uncertainty in multirate mass transfer parameters, have not previously been ascertained.

In the first phase of this study, data from eight laboratory-scale diffusion experiments performed on five Culebra samples are examined for evidence of variability in effective diffusion coefficients. Modeling is performed under the assumption of a lognormal distribution of D_e . The estimated standard deviation (σ_d) of $\ln(D_e)$ within each sample ranged from 0 to 1, with most values lying between 0.5 and 1. The variability over all samples leads to a combined σ_d in the range of 0.9 to 1.2. Formation factors measured on Culebra samples are found to be well-described by a lognormal distribution with a standard deviation of approximately 0.7. As formation factor is linearly related to D_e , this implies the following: (1) the assumption of a lognormal distribution of D_e is appropriate; (2) our estimates of σ_d are reasonable; and (3) formation factors may provide an inexpensive means of characterizing variability in D_e . A comparison of our estimation results to other rock properties suggests that, at the lab-scale, the geometric mean of D_e increases with bulk porosity and the quantity of macroscopic features such as vugs and fractures. However, σ_d appears to be determined by variability within such macroscopic features and/or by micropore-scale heterogeneity. In addition, comparison of experiments at several spatial scales suggests that increasing sample volume results in an increase in σ_d .

In the second phase of the study, a suite of deterministic and stochastic simulations of one-dimensional advective-dispersive contaminant transport using a variety of diffusive mass transfer models are completed at the field- and regional-scales. Comparison of nonreactive, equilibrium, and single-rate nonequilibrium regimes yields results consistent with previous work. Most notably, rate-limited mass transfer results in increases in tailing and dispersion, a decrease in maximum plume concentration, and faster initial solute arrival relative to equilibrium processes. A distribution of diffusion rates is found to greatly accentuate these phenomena, and results in nonequilibrium mass transfer under conditions for which single-rate diffusion would approach equilibrium. These effects are generally present at greatly differing time- and space-scales and under statistically-described uncertainty in mass transfer and flow parameters, although for narrow distributions the multirate model behaves similarly to a single-rate model at the regional-scale, attaining LEA. Scaling of mean diffusion rate coefficients with experimental time-scale may result in both extreme tailing and initial solute arrival times approaching those found for nonreactive transport, with significant consequences to remediation design and waste repository risk assessment.

BIBLIOGRAPHY

- Armstrong, J. E., E. O. Frind, and R. D. McClellan, Nonequilibrium mass transfer between the vapor, aqueous, and solid phases in unsaturated soils during vapor extraction, *Water Resour. Res.*, 30(2), 355-368, 1994.
- Bahr, J. M., and J. Rubin, Direct comparison of kinetic and local equilibrium formulations for solute transport affected by surface reactions, *Water Resour. Res.*, 23(3), 438-452, 1987.
- Ball, W. P., and P. V. Roberts, Long-term sorption of halogenated organic chemicals by aquifer material, 1, Equilibrium, *Environ. Sci. Technol.*, 25, 1223-1237, 1991.
- Ball, W. P., and P. V. Roberts, Long-term sorption of halogenated organic chemicals by aquifer material, 2, Intraparticle diffusion, *Environ. Sci. Technol.*, 25, 1237-1249, 1991.
- Barber, L. B., II, E. M. Thurman, D. D. Runnells, Geochemical heterogeneity in a sand and gravel aquifer: Effect of sediment mineralogy and particle size on the sorption of chlorobenzenes, *J. Contam. Hydrol.*, 9, 35-54, 1992.
- Bear, J., *Dynamics of fluids in porous media*, Dover, New York, NY, 764 pp., 1972.
- Beauheim, R. L., and R. M. Holt, "Hydrogeology of the WIPP Site," *Geological and hydrological studies of evaporites in the northern Delaware Basin for the Waste Isolation Pilot Plant (WIPP), New Mexico, Field Trip #14 Guidebook, November 1-4, 1990*, SAND90-2035J, Dallas Geological Society, Dallas, TX, 1990.
- Brusseau, M. L., and P. S. C. Rao, Sorption nonideality during organic contaminant transport in porous media, *Crit. Rev. Environ. Control*, 19(1), 33-99, 1989.
- Christian-Freear, T. L., V. C. Tidwell, and L. C. Meigs, *Technical memorandum: Results of experimental methodology development for visualizing and quantifying matrix diffusion in the Culebra Dolomite*, Geohydrology Department, Sandia National Laboratories, Albuquerque, NM, 1997.
- Cunningham, J. A., and P. V. Roberts, Use of temporal moments to investigate the effects of nonuniform grain-size distribution on the transport of sorbing solutes, *Water Resour. Res.*, 34(6), 1415-1425, 1998.
- Curtis, G. P., P. V. Roberts, and M. Reinhard, A natural gradient experiment on solute transport in a sand aquifer, 4, Sorption of organic solute and its influence on mobility, *Water Resour. Res.*, 22(13), 2059-2068, 1986.
- Cussler, E. L., *Multicomponent diffusion*, Elsevier, Amsterdam, 176 pp., 1976.
- Cussler, E. L., *Diffusion mass transfer in fluid systems*, Cambridge University Press, Cambridge, 580 pp., 1997.
- Deans, H. A., and C. T. Carlisle, Single-well tracer test in complex pore systems, *Society of Petroleum Engineers/U.S. Department of Energy SPE/DOE 14886*, 61-68, 1986.
- de Hoog, F. R., J. H. Knight, and A. N. Stokes, An improved method for numerical inversion of Laplace transforms, *SIAM J. Sci. Stat. Comput.*, 3, 357-366, 1982.

Dykhuizen, R. C., and W. H. Casey, *An analysis of solute diffusion in the Culebra Dolomite*, SAND89-0750, Sandia National Laboratories, Albuquerque, NM, 1989.

Fetter, C. W., *Contaminant Hydrogeology*, Macmillan, New York, NY, 458 pp., 1993.

Fry, V. A., and J. D. Istok, Effects of rate-limited desorption on the feasibility of in situ bioremediation, *Water Resour. Res.*, 30(8), 2413-2422, 1994.

Gelhar, L. W., A. Mantoglou, C. Welty, and K. R. Rehfeldt, *A review of field-scale physical solute transport processes in saturated and unsaturated porous media*, Electric Power Research Institute EPRI EA-4190 Project 2485-5, 116 pp., 1985.

Gierke, J. S., N. J. Hutzler, and D. B. McKenzie, Vapor transport in unsaturated soil columns: Implications for vapor extraction, *Water Resour. Res.*, 28(2), 323-335, 1992.

Glueckhauf, E., Part 10. - Formulae for diffusion into spheres and their application to chromatography, *Transactions of the Faraday Society*, 51, 1540-1551, 1955.

Goltz, M. N., and M. E. Oxley, Analytical modeling of aquifer decontamination by pumping when transport is affected by rate-limited sorption, *Water Resour. Res.*, 27(4), 547-556, 1991.

Grathwohl, P., Influence of organic matter from soils and sediments of various origins on the sorption of some chlorinated aliphatic hydrocarbons: Implication on Koc correlations, *Environ. Sci. Technol.*, 24, 1687-1693, 1990.

Harmon, T. C., and P. V. Roberts, Comparison of intraparticle sorption and desorption rates for a halogenated alkene in a sandy aquifer material, *Environ. Sci. Technol.*, 28, 1650-1660, 1994.

Harmon, T. C., L. Semprini, and P. V. Roberts, Simulating groundwater solute transport using laboratory determined sorption parameters, *J. Env. Eng.*, 118(5), 666-689, 1992.

Haggerty, R., *Aquifer remediation in the presence of rate-limited mass transfer*, Ph.D. diss. (Diss. Abstr. 96-11968), Stanford University, Stanford, CA, 1995.

Haggerty, R., S. W. Fleming, L. C. Meigs, and S. A. McKenna, Convergent-flow tracer tests in a fractured dolomite, 3, Analysis of mass transfer in single-well injection-withdrawal tests, *Water Resour. Res.*, in preparation.

Haggerty, R., and S.M. Gorelick, Multiple-rate mass transfer for modeling diffusion and surface reactions in media with pore-scale heterogeneity, *Water Resour. Res.*, 31(10), 2383-2400, 1995.

Haggerty, R., and S. M. Gorelick, Modeling mass transfer processes in soil columns with pore-scale heterogeneity, *Soil Sci. Am. J.*, 62(1), 62-74, 1998.

Haggerty, R., and C. Harvey, A comparison of estimated mass transfer rate coefficients with the time-scales of the experiments from which they were determined, *EOS, Transactions*, 78(46), *AGU Fall Meeting Supplement*, p. F293, 1997.

Haggerty, R., and P. Reeves, *STAMMT-L (Solute Transport And Multirate Mass Transfer, Linear coordinates) User Guide, unpublished internal report*, Sandia National Laboratories, Albuquerque, NM, 1998.

- Handford, C. R., Marginal marine halite: Sabkhas and salinas, in *Evaporites, Petroleum, and Mineral Resources*, edited by J. L. Melvin, Elsevier, Amsterdam, 1991.
- Harvey, C. F., R. Haggerty, and S. M. Gorelick, Aquifer remediation: A method for estimating mass transfer rate coefficients and an evaluation of pulsed pumping, *Water Resour. Res.*, 30(7), 1979-1991, 1994.
- Harvey, C. F., and S. M. Gorelick, Temporal moment-generating equations: Modeling transport and mass transfer in heterogeneous aquifer, *Water Resour. Res.*, 31(8), 1895-1911, 1995.
- Harvey, J. W., B. J. Wagner, and K. E. Bencala, Evaluating the reliability of the stream tracer approach to characterize stream-subsurface water exchange, *Water Resour. Res.*, 32(8), 2441-2451, 1996.
- Holt, R. M., *Conceptual model for transport processes in the Culebra Dolomite Member, Rustler Formation*, SAND97-0194, Sandia National Laboratories, Albuquerque, NM, 1997.
- Holt, R. M., and D. W. Powers, *Facies variability and post-depositional alteration within the Rustler Formation in the vicinity of the Waste Isolation Pilot Plant, Southeastern New Mexico*, DOE/WIPP 88-004, Westinghouse Electric Corporation, Carlsbad, NM, 1988.
- Jensen, J. L., L. W. Lake, P. W. M. Corbett, and D. J. Goggin, *Statistics for Petroleum Engineers and Geoscientists*, Prentice Hall PTR, Upper Saddle River, NJ, 1997.
- Johansson, H., M. Siitari-Kauppi, M. Skalberg, and E. L. Tullborg, Diffusion pathways in crystalline rock - Examples from Aspo-diorite and fine-grained granite, in preparation.
- Jones, T. L., V. A. Kelley, J. F. Pickens, D. T. Upton, R. L. Beauheim, and P. B. Davies, *Integration of interpretation results of tracer tests performed in the Culebra Dolomite at the Waste Isolation Pilot Plant*, SAND92-1579, Sandia National Laboratories, Albuquerque, NM, 1992.
- Karickhoff, S. W., Organic pollutant sorption in aquatic systems, *J. Hydraul. Eng.*, 110(6), 707-735, 1984.
- Kelley, V. A., and G. J. Saulnier, Jr., *Core analyses for selected samples from the Culebra Dolomite at the Waste Isolation Pilot Plant Site*, SAND90-7011, Sandia National Laboratories, Albuquerque, NM, 1990.
- Knopman, D. S., and C. I. Voss, Behavior of sensitivities in the one-dimensional advection-dispersion equation: Implications for parameter estimation and sampling design, *Water Resour. Res.*, 23(2), 253-272, 1987.
- Kyle, J. R., Evaporites, evaporitic processes and mineral resources, in *Evaporites, Petroleum, and Mineral Resources*, edited by J. L. Melvin, Elsevier, Amsterdam, 1991.
- LaVenue, A. M., T. L. Cauffman, and J. F. Pickens, *Ground-water flow modeling of the Culebra Dolomite, Volume I: Model calibration*, SAND89-7068, Sandia National Laboratories, Albuquerque, NM, 1990.
- Li, L., D. A. Barry, P. J. Culligan-Hensley, and K. Bajracharya, Mass transfer in soils with local stratification of hydraulic conductivity, *Water Resour. Res.*, 30(11), 2891-2900, 1994.
- Li, Y., and S. Gregory, Diffusion of ions in sea water and in deep-sea sediments, *Geochim. Cosmochim. Acta*, 38, 704-714, 1974.

Lovera, O. M., M. T. Heizler, and T. M. Harrison, Argon diffusion domains in K-feldspar II: kinetic properties of MH-10, *Contrib. Mineral. Petrol.*, 113, 381-393, 1993.

Lovera, O. M., F. M. Richter, and T. M. Harrison, The $^{40}\text{Ar}/^{39}\text{Ar}$ thermochronometry for slowly cooled samples having a distribution of diffusion domain sizes, *J. Geophys. Res.*, 94(B12), 17,917-17,935, 1989.

Lucero, D. A., G. O. Brown, and C. E. Heath, *Laboratory column experiments for radionuclide adsorption studies of the Culebra Dolomite Member of the Rustler Formation*, SAND97-1763, Sandia National Laboratories, Albuquerque, NM, 1998.

Mann, U., An integrated approach to the study of primary petroleum migration, in *Geofluids: Origin, Migration and Evolution of Fluids in Sedimentary Basins*, Geological Society Special Publication No. 78, edited by J. Parnell, The Geological Society, London, 1994.

Marquardt, D., An algorithm for least-squares estimation of nonlinear parameters, *SIAM J. Appl. Math.*, 11, 431-441, 1963.

McKenna, S. A., L. C. Meigs, and R. Haggerty, Convergent-flow tracer tests in a fractured dolomite, 4, Double porosity, multiple mass-transfer rate processes in two-well convergent flow tests, *Water Resour. Res.*, in preparation.

Meigs, L. C., and R. L. Beauheim, Tracer tests in a fractured dolomite, 1, Experimental design and observed tracer recoveries, *Water Resour. Res.*, in preparation.

Meigs, L. C., and J. McCord, *Memorandum to file: Physical transport in the Culebra Dolomite*, WPO#37450/39167, Geohydrology Department, Sandia National Laboratories, Albuquerque, NM, 1996.

Pignatello, J. J., Slowly reversible sorption of aliphatic halocarbons in soils, 2, Mechanistic aspects, *Environ. Toxicol. Chem.*, 9, 1117-1126, 1990.

Qin, Z., F. Lu, and A. T. Anderson, Jr., Diffusive reequilibration of melt and fluid inclusions, *American Mineralogist*, 77, 565-576, 1992.

Quinodoz, H. A. M., and A. J. Vallochi, Stochastic analysis of the transport of kinetically sorbing solutes in aquifers with randomly heterogeneous hydraulic conductivity, *Water Resour. Res.*, 29(9), 3227-3240, 1993.

Rabideau, A. J., and C. T. Miller, Two-dimensional modeling of aquifer remediation influenced by sorption nonequilibrium and hydraulic conductivity heterogeneity, *Water Resour. Res.*, 30(5), 1457-1470.

Rao, P. S. C., D. E. Rolston, R. E. Jessup, and J. M. Davidson, Solute transport in aggregated porous media: Theoretical experimental evaluation, *Soil Sci. Soc. Am. J.*, 44, 1139-1146, 1980.

Roberts, P. V., M. N. Goltz, and D. M. MacKay, A natural gradient experiment on solute transport in a sand aquifer, 3, Retardation estimates and mass balances for organic solutes, *Water Resour. Res.*, 22(13), 2047-2058, 1986.

Ruthven, D. M., and K. F. Loughlin, The effect of crystalline shape and size distribution on diffusion measurements in molecular sieves, *Chem. Engng. Sci.*, 26, 577-584, 1971.

Shackelford, C. D., Laboratory diffusion testing for waste disposal-A review, *J. Contam. Hydrol.*, 7, 177-217, 1991.

Steinberg, S. M., J. J. Pignatello, and B. L. Sawhney, Persistence of 1,2-dibromoethane in soils: Entrapment in intraparticle micropores, *Environ. Sci. Technol.*, 21(12), 1201-1208, 1987.

TerraTek contractor's report, *Physical property characterization of miscellaneous rocks samples: Contract AA-2896, TR97-03*, TerraTek, Salt Lake City, UT, 1996.

Tidwell, V. C., and R. J. Glass, X ray and visible light transmission for laboratory measurement of two-dimensional saturation fields in thin-slab systems, *Water Resour. Res.*, 30(11), 2873-2882, 1994.

Tidwell, V. C., L. C. Meigs, T. Christian-Frear, and C. M. Boney, Effects of spatially heterogeneous porosity on matrix diffusion as investigated by X-ray absorption imaging, in preparation.

Tomich, J. F., R. L. Dalton, Jr., H. A. Deans, and L. K. Shallenberger, Single-well tracer method to measure residual oil saturation, *J. Petrol. Technol.*, 25(2), 211-218, 1973.

Valocchi, A. J., Validity of the local equilibrium assumption for modeling sorbing solute transport through homogeneous soils, *Water Resour. Res.*, 21(6), 808-820, 1985.

Valocchi, A. J., Use of temporal moment analysis to study reactive solute transport in aggregated porous media, *Geoderma*, 46, 233-247, 1990.

Weber, W. J., Jr., P. M. McGinley, and L. E. Katz, Sorption phenomena in subsurface systems: Concepts, models and effects on contaminant fate and transport, *Water Resour. Res.*, 25(5), 499-528, 1991.

Welty, J. R., C. E. Wicks, and R. E. Wilson, *Fundamentals of Momentum, Heat, and Mass Transfer*, John Wiley and Sons, New York, NY, 803 pp., 1984.

Wilson, J., Removal of aqueous phase dissolved contamination: Non-chemically enhanced pump and treat, in *Subsurface Restoration*, edited by C. H. Ward, J. Cherry, and M. R. Scalf, Lewis, Boca Raton, Fla., 1995.

Wood, W. W., T. F. Kraemer, and P. P. Hearn Jr., Intragranular diffusion: An important mechanism influencing solute transport in clastic aquifers?, *Science*, 247, 1569-1572, 1990.

Wu, S., and P. M. Gschwend, Numerical modeling of sorption kinetics of organic compounds to soil and sediment particles, *Water Resour. Res.*, 24(8), 1373-1383, 1988.

APPENDICES

APPENDIX 1: FORTRAN77 code MRSD

```

program MRSD

implicit none

c remember to change dimensions of mass and boundary conditions
c for each data set.

C procedure for SINGLE-RATE parameter estimations:
c - change dimensions in all variables from 2 to 1
c - change everything with SINGLE-RATE comment preceding it
c - no changes necessary for forward single-rate run, except in
c parameter file (input.prm)

c general variables:
double precision mu,sig,F,C0,Deff,l,M0,t,Dmax,Daq,Mdata(15)
double precision M,Mratio(15),time(15),C1(7),concin(7)
integer i,TN,inout,k,q,est,mode,TC,TNB,TCB
double precision timeC(7),sqerr

c inversion/statistics variables:
double precision xguess(2),xscale(2),fscale(15),serr(15)
double precision fjac(15,2),xf(2),rmse,mse
integer iparam(6),nx
double precision rparam(7)

c to deal with itinerant estimation routine (used by ERSET):
integer iersvr,ipact,isact

common/c/C0,C1,l,TN,TC
common/f/inout
common/g/time,timeC
common/h/Mdata
common/thing1/concin
common/thing2/mode
common/thing3/M0

c uncomment for SINGLE-RATE parameter estimations:
c common/z/sig

external massratio,obj,DU4LSF,DUNLSF,statistics
external ERSET

open(10,file='input.prm')
open(11,file='boundary.dat')
open(12,file='massratio.dat')
open(13,file='massratio.out')

C ** READING IN PARAMETERS: **

read(10,*) mu          !geometric mean of lognormal dist. of Deff

```

```

read(10,*) sig      !standard dev. of lognormal dist. of Deff
read(10,*) C0       !initial conc. in slab
read(10,*) l        !length of slab
read(10,*) TN       !number of (t,Mratio) data/output points
read(10,*) TC       !number of (t,C1) data points
read(10,*) inout    !inout=0: diffusion in; inout=1: diffusion out
read(10,*) mode     !1:continuous multirate; 2: single rate
read(10,*) est      !1:forward only; 0:parameter estimation

```

c ** READING IN TIME-VARIANT BOUNDARY (RESERVOIR) CONCENTRATIONS **

c There should be a (~arbitrary, but obviously reasonable) value for
c the boundary concentration at very small time. This first data point
c is to give Laplace transform a "place to start from". There should
c also be boundary concentrations at at least one very late time, because
c taking Laplace transform of boundary conditions requires (t,C1)
c pair at the next value of t [i.e., C1bar(n) requires value for C1(n+1)].
c timeC's need not correspond to time's and TN doesn't need to equal TC.

```

do 20,k=1,TC
  read(11,*) timeC(k),concin(k)
20  continue

```

C ** READING IN OBSERVED MASS CURVES **

c note: if Mdata(k) at the first or last time is =1, this may cause
c problems with the inversion routine for mass in; numerical error in
c the code calculations combined with the fact that 1-M/M0 is used
c can result in negative values in the mass breakthrough curve, which
c doesn't seem to be good.

```

do 22,k=1,TN
  read(12,*) time(k),Mdata(k)
22  continue

```

c ****START OF ESTIMATION SECTION ****

c ** Set number of unknown parameters: **

c change to nx=1 for SINGLE-RATE parameter estimation:
 nx=2

c set initial guesses for parameter values:

```

  if (est.eq.0) then
    xguess(1) = mu

```

c comment out following line if SINGLE-RATE parameter estimation:
 xguess(2) = log(sig)

c weighting parameters:

```

  do 40,i=1,nx
    xscale(i) = 1.d0

```

```

40  continue

```

c weighting data:

```

  do 70,i=1,TN
    fscale(i)=1.d0

```

70 continue

```
call DU4LSF(iparam,rparam)
iparam(2) = 4
```

c If you wish to force "convergence" (i.e. make the inversion stop gracefully
c at a certain point), set iparam(4) equal to the maximum number of
c iterations desired. One iteration is a forward run for a "base" set of
c parameters (initial parameters or the ones estimated in the last iteration)
c plus one forward "perturbation" run for each of the parameters
c being estimated. Note that parameter estimation statistics will not be
c calculated unless the inverse run stops gracefully (on its own).

```
iparam(4)=12
```

c making it so that inversion routine stops "nicely" when iparam(4)
c is reached:

```
iersvr=4
ipact=1
isact=0
call ERSET(iersvr,ipact,isact)
```

c calling inversion routine:

```
call DUNLSF(obj,TN,nx,xguess,xscale,fscale,iparam,rparam,xf,
& serr,fjac,TN)
```

```
mu = xf(1)
```

c comment out following line if SINGLE-RATE parameter estimation:

```
sig = exp(xf(2))
```

```
endif
```

C ***END OF ESTIMATION SECTION***

c ** CALCULATE MASS IN OR MASS REMAINING CURVE: **

```
call massratio(mu,sig,Mratio)
```

c ** COMPUTE RMSE: **

c Compute mean square error:

```
mse = 0.d0
do 110,k=1,TN
sqerr=log(abs(Mdata(k)/Mratio(k)))*log(abs(Mdata(k)/Mratio(k)))
mse = mse + sqerr
```

```
110 continue
```

```
rmse = sqrt(mse)
```

c ** COMPUTE PARAMETER ESTIMATION STATISTICS, IF APPLICABLE: **

```
if (est.eq.0) then
call statistics(fjac,nx,TN,rmse)
endif
```

c ** WRITE RESULTS TO FILE: **

```

if (inout.eq.0) then
  write(13,*) ''
  write(13,*) 'M(t)/M(t=infinity) (mass in curve):'
  write(13,*) ''
  write(13,160) 'M(infnty)=' ,M0
else
  write(13,*) ''
  write(13,*) 'M(t)/M(t=0) (mass remaining curve):'
  write(13,*) ''
  write(13,160) 'M(t=0)=' ,M0
endif
if (mode.eq.2) then
  write(13,160) 'Deff= ',exp(mu)
  write(13,160) 'RMSE = ',rmse
  write(13,*) ''
endif
if (mode.eq.1) then
  write(13,160) 'mu = ',mu
  write(13,160) 'sig = ',sig
  write(13,160) 'RMSE = ',rmse
  write(13,*) ''
endif
160 format(A,d12.5,A,d12.5)
   write(13,*) '1st column = time [I]'
   write(13,*) '2nd column = calculated mass ratio [-]'
   write(13,*) '3rd column = observed mass ratio [-]'
   write(13,*) ''
   do 200,k=1,TN
   write(13,180) time(k),Mratio(k),Mdata(k)
180   format(3e21.13)
200   continue
close(13)

stop
end

c *****
c ****Subroutine to calculate M/M(t=0) or M/M(t=infinity)*****
c *****(This subroutine also "drives" everything else) *****
c *****
subroutine massratio(mu,sig,Mratio)

implicit none
double precision mu,sig,F,C0,Deff,l,M0,t,Dmax,Daq,origC0
double precision M,Mratio(15),time(15),C1(7),concin(7)
double precision timeC(7),Dmin
integer i,TN,inout,k,q,TC,mode
c mu and sig can't be both an argument to the subroutine and within a
c a common block inside of it. Want mu and sig to be passed directly
c from main program and from objective function to massratio as a
c subroutine argument; but need mu and sig in common block to pass to
c function FdM, which can have as an argument only (Deff). So, define

```

c mus and sigs identical to mu and sig and use in common block:

```
double precision mus,sigs,pi
double precision Plow,Phigh,DNORIN
```

```
common/b/t,Dmax,Dmin
common/c/C0,C1,l,TN,TC
common/e/mus,sigs
common/f/inout
common/g/time,timeC
common/thing1/concin
common/thing2/mode
common/thing3/M0
external MASS,DNORIN
```

```
pi=3.141592654
```

```
mus=mu
sigs=sig
```

```
if(mode.eq.1) then
```

```
Plow=0.000000001
Phigh=0.999999999
Dmin=exp(mus+sigs*DNORIN(Plow))
Dmax=exp(mus+sigs*DNORIN(Phigh))
```

```
print*, 'mus=',mus,' sigs=',sigs
print*, 'Dmin=',Dmin,' Dmax=',Dmax
```

```
endif
```

c ** Calculate mass in slab at time = infinity or 0: **

c **NOTE: this causes serious problems when inverting diffusion-in data;
c however, code is retained (but commented out) because it can serve
c as a usefull check: M0 calculated by code should be equal to l, the
c length of the slab**

```
c    print*, 'starting mass calculations'
```

```
c
```

```
c    if (inout.eq.0) then
```

c for diffusion in, find mass at time=infinity:

```
c    do 15,q=1,TC
```

```
c        C1(q)=1.d0
```

```
c 15    continue
```

```
c    else
```

c for diffusion out, find mass at time=0 by finding mass at time =

c infinity for diffusion in problem. Store initial concentration in

c slab in origC0 variable, and temporarily set initial conc to 0. Setting

c all reservoir conc's to 1 ensures that as much mass as possible is

c stuffed into slab.

```
c    origC0=C0
```

```
c    C0=0.d0
```

```
c    do 17,q=1,TC
```

```

c      C1(q)=1.d0
c 17  continue
c      endif
c
c set time for which inverse Laplace transform will be calculated (i.e.
c time at which mass in slab is being evaluated):
c      t=time(TN)
c call subroutine to calculate total mass in slab:
c      call MASS(M0)

c Use maximum mass in slab = (porosity)*(C/Co)*l:
c porosity cancels out with porosity in the denominator for mass ratio
c C/Co=1 at t=0 for mass out and at t=infinity for mass in
      M0=l

c print update to screen and store info:
      if (inout.eq.0) then
          print*, 'M(t=infinity) / porosity =',M0
      else
          print*, 'M(t=0) / porosity =',M0
      endif

c ** Calculate mass in slab at time, t: **

c following commented-out section required only if routine to calculate
c M0 (above) is used:
c set boundary concentrations to those from input file:
c      if (inout.eq.1) then
c          C0=origC0
c      endif
c      do 25,k=1,TC
c          C1(k)=concin(k)
25  continue

c start loop to evaluate mass at successive times:

      do 30,i=1,TN

c set time for which inverse Laplace transform (i.e. mass in slab)
c will be evaluated:
          t=time(i)

          call MASS(M)
c calculating M/Minfinity (mass in) or M/M0 (mass remaining) at time, t:
          Mratio(i)=M/M0
c FOR MASS IN, USE 1-Mratio:
          if (inout.eq.0) Mratio(i)=1-Mratio(i)
c NOTE: FOR MASS IN, DATA MUST ALSO BE 1-Mratio

c print update to screen:
      if (inout.eq.0) then
          write(*,500) 'time, M(t)/M(infinity) =',t,Mratio(i)

```



```

        else
            write(*,500) 'time, M(t)/M(0) =',t,Mratio(i)
        endif
500  format(A,d14.5,d14.5)

30  continue

c print update to screen:
    print*, 'Finished computing mass ratios'

    return
end

C *****
C *****Subroutine to calculate mass, M, in slab at some time, t *****
C *****
    subroutine MASS(M)

        implicit none
        double precision M,FdM,t,Dmax,mus,sigs,Deffs,alpha
        double precision relerr,kmax
        double precision errabs,errrel,errest,Dmin
        complex*16 SMbar
        integer irule,mode,l,q,interv
        common/b/t,Dmax,Dmin
        common/e/mus,sigs
        common/thing2/mode
        common/a/Deffs
        external FdM,DQDAG,DINLAP,SMbar

c integration parameters for DQDAG (if continuous multirate):
        errabs=1.d-4
        errrel=1.d-2
        irule=2

c inverse Laplace transform parameters for DINLAP (if single rate):
        alpha=0.d0  !(set to 0 if unknown, according to IMSL literature)
        kmax=1000.d0  !maximum number of function evaluations
        relerr=1.d-3

c For single rate of diffusion:
        if (mode.eq.2) then
c single effective diff. coeff. from [ln(Deffs)-mus=0]:
            Deffs=exp(mus)
c call inverse Laplace transform function:
            call DINLAP(SMbar,1,t,alpha,relerr,kmax,M)
        endif

c For continuous multirate:
        if (mode.eq.1) then
c Integrate FdM from Deff=Dmin to Deff=Dmax, obtaining M:

```

```

call DQDAG(FdM,Dmin,Dmax,errabs,errrel,irule,M,errest)

endif

return
end

c *****
c *****Function to evaluate mass in slab at some time, for some value of
c *****Deff dictated by DQDAG*****
c *****
double precision function FdM(Deff)

implicit none
double precision Deff,F,dM,alpha,relerr,kmax,pi,t,Dmax
double precision mus,sigs,Deffs,Fpart1,Fpart2,Dmin
complex*16 SMbar
common/b/t,Dmax,Dmin
common/e/mus,sigs
c DQDAG automatically passes its dictated value of Deff on to the function which
c it is integrating (FdM), but a common statement is required to get this value
c of Deff (copied to Deffs) to the function which must be inverse Laplace transformed
c before the integration can be completed (dMbar):
common/a/Deffs

external SMbar,DINLAP

Deffs=Deff

alpha=0.d0 !(set to 0 if unknown, according to IMSL literature)
kmax=1000.d0 !maximum number of function evaluations
pi=3.141592654
relerr=1.d-2

call DINLAP(SMbar,1,t,alpha,relerr,kmax,dM)

Fpart1=1/(sqrt(2*pi)*sigs*Deff)
Fpart2=-((log(Deff)-mus)*(log(Deff)-mus))/(2*sigs*sigs)
F=Fpart1*exp(Fpart2)

c DEBUGGING:
c for 'dirac delta' with Deff=1.1d-5; use FdM=F*dM and result should be
c almost the same as for single-rate:
c F=0.5d6
c for lognormal distribution alone (comment out FdM=F*dM below); result
c should be very close to 1.0:
c FdM=F
c using a square wave for probability distribution:
c if ((Deff.lt.Dmin).or.(Deff.gt.Dmax)) then
c F=0.0d0
c else

```

```

c      F=1/(Dmax-Dmin)
c      endif

```

```

      FdM=F*dM

```

```

      return
      end

```

```

*****
***** Function for Laplace transform of mass in/out at some time ***
*****for a given single rate of diffusion *****
*****

```

```

      complex*16 function SMbar(p)

```

```

      implicit none
      complex*16 p,C1bar,aa,bb,cc,dd,ee
      double precision C0,l,C1(7),time(15),dc,dt,Deffs
      double precision timeC(7)
      integer i,j,TN,TC
      common/c/C0,C1,l,TN,TC
      common/g/time,timeC
      common/a/Deffs
      logical difnan
      external difnan

```

```

      C1bar = 0.d0

```

```

c take Laplace transform of boundary conditions at value of p handed
c by DINLAP:

```

```

      do 5,j=1,TC-1
         dc = C1(j+1)-C1(j)
         dt = timeC(j+1)-timeC(j)
         C1bar = C1bar + ((dc+C1(j)*dt*p)*exp(-p*timeC(j))
&   - (dc+C1(j+1)*dt*p)*exp(-p*timeC(j+1)))/(p*p*dt)
5      continue

```

```

c compute singlemass (mass diffused in/out by time t) bit by bit:

```

```

      aa=C1bar-(C0/p)
      bb=l*cdsqrt(p/Deffs)
      cc=cdsqrt(p/Deffs)
      ee=C0*l/p

```

```

c express hyperbolic tangent in terms of exponentials:

```

```

      dd=(cdexp(bb)-cdexp(-bb))/(cdexp(bb)+cdexp(-bb))

```

```

c alternate expression for small times; at large p and therefore large

```

```

c bb (for which dd and thus SMbar are nan), dd=tanh(bb)=(1,0):

```

```

      if (difnan(dd)) dd = (1,0)

```

```

      SMbar=((aa/cc)*dd)+ee

```

```

      return

```

```

end

c *****
c *****Objective function to be minimized by estimation routine*****
c *****
  subroutine obj(TN,nx,xf,serr)

    implicit none
    integer TN,nx,k,inout
    double precision mu,sig,xf(2),serr(15),Mratio(15),sqerr
    double precision Mdata(15),mse,rmse,time(15)
    double precision timeC(7)
    common/f/inout
    common/g/time,timeC
    common/h/Mdata

c uncomment for SINGLE-RATE inversions:
c   common/z/sig

    external massratio

c Copy param. est. variables to mu, sig for use in mass calculations:
    mu = xf(1)
c comment out for SINGLE-RATE inversion:
    sig = exp(xf(2))

c Perform mass calculations:
    call massratio(mu,sig,Mratio)

c Calculating mean errors:
    mse = 0.d0
    do 10,k=1,TN
      sqerr=log(abs(Mdata(k)/Mratio(k)))*log(abs(Mdata(k)/Mratio(k)))
      mse = mse + sqerr
      serr(k)=sqrt(sqerr)
10  continue
    rmse = sqrt(mse)

c writing intermediate results to file:
    open(41,file='progress.mss')
    if (inout.eq.0) then
      write(41,*) 'M(t)/M(t=0), parameter estimation:'
    else
      write(41,*) 'M(t)/M(t=infinity), parameter estimation:'
    endif
    write(41,160) 'mu = ',mu
    write(41,160) 'sig = ',sig
    write(41,160) 'RMSE = ',rmse
160  format(A,d12.5,A,d12.5)
    write(41,*) '1st column = time [T]'
    write(41,*) '2nd column = calculated mass ratio [-]'
    write(41,*) '3rd column = observed mass ratio [-]'

```

```

        do 200,k=1,TN
        write(41,180) time(k),Mratio(k),Mdata(k)
180    format(3e21.13)
200    continue
        close(41)

c Writing intermediate parameter estimates and residuals to file:
        open(30,file='progress.sts',access='append')
        write(30,*) 'mu,sig,rmse:'
        write(30,'(7d15.8)') mu,sig,rmse
        close(7)

        return
        end

c *****
c *****Subroutine to calculate parameter estimation statistics*****
c *****
        subroutine statistics(fjac,nx,TN,rmse)

        integer nx,TN
        double precision XTX(2,2),covariance(2,2),eigenval(2),
& fjac(15,2),numerator,denominator,corcoef(2,2),
& inverse(2,2),rmse

        open(29,file='estimation.sts')

c compute square of sensitivity matrix:
        call dmxtxf(TN,nx,fjac,TN,nx,XTX,nx)
c compute inverse of square of sensitivity matrix:
        call dlinrg(nx,XTX,nx,inverse,nx)
c calculate correlation coefficients:
        do 33,i=1,nx
        do 34,j=1,nx
            numerator=inverse(i,j)
            denominator=sqrt(inverse(i,i)*inverse(j,j))
            corcoef(i,j)=numerator/denominator
34    continue
33    continue
c compute covariance matrix:
        do 340,i=1,nx
        do 350,j=1,nx
            covariance(i,j)=rmse*rmse*inverse(i,j)
350    continue
340    continue
c compute eigenvalues of covariance matrix:
        call devlsf(nx,covariance,nx,eigenval)
c write stats to file:
        write(29,*) 'PARAMETER ESTIMATION STATISTICS'
        write(29,*) 'sensitivity matrix (Jacobian), X:'
        do 76,i=1,TN
            write(29,41) (fjac(i,j),j=1,nx)

```

```
76 continue
41 format(5e12.4)
   write(29,*) 'XtX (information matrix), square of sensitivity matrix:'
   do 77,i=1,nx
     write(29,41) (XtX(i,j),j=1,nx)
77 continue
   write(29,*) 'covariance matrix,(RMSE^2)*(inverse of XtX):'
   do 78,i=1,nx
     write(29,41) (covariance(i,j),j=1,nx)
78 continue
   write(29,*) 'correlation coefficients:'
   do 36,i=1,nx
     write(29,41) (corcoef(i,j),j=1,nx)
36 continue
   write(29,*) 'eigenvalues of covariance matrix:'
   do 79,i=1,nx
     write(29,*) eigenval(i)
79 continue

   close(29)

   return
end
```

APPENDIX 2: FORTRAN77 code STAMMTLMC

```

program STAMMTLMC

c Sean W. Fleming
c Department of Geosciences
c Oregon State University
c Corvallis, OR 97331
c March 1998

implicit none

c double precision meanmu,stdevmu,meansig,stdevsig,outmu,outsig
c double precision rannum(1),DNORIN
c integer NR

c The following comment block describes the meaning of the above variables
c IF a normal distribution of error about a mean value is used for
c the mass transfer parameters (e.g. confidence intervals about an estimate);
c this has been replaced with uniform distributions. Comment block and
c corresponding code operations (commented out below) are maintained here for
c future reference:
c - meanmu is the value of mu estimated by STAMMT-R or by MRSD (and converted
c to the geometric mean of *rate* coefficients) (input)
c - stdevmu is the uncertainty in the estimated value of mu (square root of the
c appropriate diagonal from the covariance matrix), assuming error in the
c estimate is normally distributed about the mean estimated value (input)
c - meansig is the natural logarithm of the value of sig estimated by
c STAMMT-R or MRSD (input)
c - stdevsig is the uncertainty in the estimated value of ln(sig) (i.e. the
c square root of the appropriate diagonal from the covariance matrix),
c assuming error is normally distributed about the mean estimated value;
c as the estimate is ln(sig), this is equivalent to a lognormal distribution
c of error about the estimated value of sig (input)
c - outmu is the value of mu which the Monte Carlo routine will feed to STAMMT-L
c - outsig is the value of sig which the Monte Carlo routine will feed to STAMMT-L
c - rannum(1),DNORIN used in pulling a value from the cdf.

double precision outmu,outsig
double precision advporos,PWvel,difporos,capcoef,Dvel

c - outmu is mu, pulled from its distribution and fed to STAMMT-L
c - outsig is sig, pulled from its distribution and fed to STAMMT-L
c - advporos is the advective porosity, pulled from its distribution
c - difporos is the diffusive porosity, pulled from its distribution
c - Dvel is the Darcy velocity, pulled from its distribution
c - PWvel is the pore water velocity, calculated from Dvel and advporos,
c and fed to STAMMT-L
c - capcoef is the capacity coefficient, Btot, calculated from advporos and

```

c difporos, and fed to STAMMT-L

```

double precision time(300),M(300),cncntrtn(300)
double precision Mten,Mfifty,Mninety,peakC,tpeakC
double precision tmpmnt3,tmpmnt0,tmpmnt1,tmpmnt2,tailt,Mone
double precision mss,mnrrvltm,stdBTC,skwnss
double precision stdBTC1,stdBTC2,skwnss1,skwnss2,skwnss3
integer i,j,count,TN,flag3,count0,k

common/moments/tmpmnt0,tmpmnt1,tmpmnt2,tailt

external STAMMTL,PERCENTILE,PEAKCONC
external MTDIST,TRANSPORTDIST

```

c For normal distributions of error about mean values, for mass transfer
c parameters; no longer used:

c external DNORIN,DRNUN

```

open(unit=12,file='montecarlo.MT-MR-3000.out',access='append')

```

c write header:

```

write(12,*) 'column 1 = count'
write(12,*) 'column 2 = mu'
write(12,*) 'column 3 = sig'
write(12,*) 'column 4 = advective porosity'
write(12,*) 'column 5 = pore water velocity'
write(12,*) 'column 6 = Darcy velocity'
write(12,*) 'column 7 = diffusive porosity'
write(12,*) 'column 8 = capacity coefficient'
write(12,*) 'column 9 = Mone, time at which 1% of mass is removed'
write(12,*) 'column 10 = Mten, time at which 10% of mass is removed'
write(12,*) 'column 11 = Mfifty, time at which 50% of mass is removed'
write(12,*) 'column 12 = Mninety, time at which 90% of mass is removed'
write(12,*) 'column 13 = peakC, maximum C/C0 in the BTC'
write(12,*) 'column 14 = tpeakC, time at which peakC occurs'
write(12,*) 'column 15 = tailt, simple tailing measure'
write(12,*) 'column 16 = mss, mass in the plume'
write(12,*) 'column 17 = mnrrvltm, mean arrival time of solute'
write(12,*) 'column 18 = stdBTC, standard deviation of the BTC'
write(12,*) 'column 19 = skwnss, BTC skewness coefficient;(+) = tailing'
close(12)

```

c For normal distribution of error about a mean value for mass transfer
c parameters; no longer used:

c setting values for MC simulation (see above):

```

c meanmu=-7.689d0
c meansig=1.271d0
c stdevmu=0.598d0
c stdevsig=0.1285

```

c for random number generator:

```

c NR=1

```

c initializing variables used to keep track of Monte Carlo simulation:


```

count=0
count0=0

do 20,i=1,10000

c For normal distribution of error about a mean value for mass transfer
c parameters (mean mu and mean ln(sig); no longer used:
c randomly pluck a value of mu from the cdf of errors about the estimate of mu:
c   call DRNUN(NR,rannum(1))
c   outmu=meanmu+stdevmu*DNORIN(rannum(1))
c randomly pluck a value of sig from the cdf of errors about the estimate of sig:
c   call DRNUN(NR,rannum(1))
c   outsig=exp(meansig+stdevsig*DNORIN(rannum(1)))

c OBTAINING VALUES FOR STOCHASTIC VARIABLES FROM THEIR CDFs:
  call MTDIST(outmu,outsig)
  call TRANSPORTDIST(advporos,PWvel,difporos,capcoef,Dvel)

c feed these values to modified STAMMT-L and get back a mass BTC, a concentration
c BTC, and a the value for TN (# of points in BTC; TNS in STAMMT-L) to be used in
c subroutine PERCENTILE:
  call STAMMTL(outmu,outsig,PWvel,capcoef,TN,time,M,cncntrtn)

c cleaning up numerical error in curves returned by STAMMT-L; results from
c forward scoping runs suggest results are not reliable below C/C0 or M/M0
c of ~1.0D-7:
  do 500,k=1,TN
    if (M(k).lt.(1.0d-7)) then
      M(k)=0.0d0
    endif
    if (cncntrtn(k).lt.(1.0d-7)) then
      cncntrtn(k)=0.0d0
    endif
  500 continue

c find times in the mass curve at which 1%, 10%, 50%, 90% of the mass is
c removed:
  call PERCENTILE(time,M,TN,Mone,Mten,Mfifty,Mninety,flag3)
c respond to bad numerical error in mass curve if present ("wavy" mass curves
c seen in some runs completed using weird input parameter values):
  if (flag3.eq.1) then
    print*,'This mass BTC does not monotonically increase'
    print*,'mu=',outmu
    print*,'sig=',outsig
    print*,'Skipping to next parameter combination'
    goto 20
  endif

c find peak concentration, time to peak conc., and temporal moments of BTC:
  call PEAKCONC(time,cncntrtn,TN,peakC,tpeakC,tmpmnt3)

c turn temporal moments into meaningful quantities, following Harvey and

```

```

c Gorelick, WRR 31(8), 1995:
c find contaminant mass in plume:
  mss=Dvel*(4.4d0)*(1.0d0)*tmpmnt0/advporos
c find mean arrival time of solute:
  mnrrvlm=tmpmnt1/tmpmnt0
c find standard deviation of BTC:
  stdBTC1=tmpmnt2/tmpmnt0
  stdBTC2=(tmpmnt1/tmpmnt0)*(tmpmnt1/tmpmnt0)
  stdBTC=sqrt(stdBTC1-stdBTC2)
c find skewness coefficient of BTC; positive skewness coefficient means tailing:
  skwnss1=tmpmnt3/tmpmnt0
  skwnss2=3*((tmpmnt1*tmpmnt2)/(tmpmnt0*tmpmnt0))
  skwnss3=2*(tmpmnt1/tmpmnt0)*(tmpmnt1/tmpmnt0)*(tmpmnt1/tmpmnt0)
  skwnss=(skwnss1-skwnss2+skwnss3)/(stdBTC*stdBTC*stdBTC)

c increment simulation counter:
  count=count+1

c write key input parameters and results from i th. simulation to a file:
  open(unit=12,file='montecarlo.MT-MR-3000.out',access='append')
  write(12,80) count,outmu,outsig,advporos,PWvel,Dvel,difporos,
    & capcoef,Mone,Mten,Mfifty,Mninety,peakC,tpeakC,tailt,mss,mnrrvlm,
    & stdBTC,skwnss
80  format(I7,18e13.5)
  close(12)

c keep track of simulation, write progress report every 100th iteration:
  if (count.eq.(count0+100)) then
    open(unit=15,file='MCprogress.MT-MR-3000.out')
    write(15,*) 'This is run # ',count,','
    write(15,*) 'mu=',outmu
    write(15,*) 'sig=',outsig
    write(15,*) 'advporos=',advporos
    write(15,*) 'PWvel=',PWvel
    write(15,*) 'Dvel=',Dvel
    write(15,*) 'difporos=',difporos
    write(15,*) 'capcoef=',capcoef
    write(15,*) 'Mone=',Mone
    write(15,*) 'Mten=',Mten
    write(15,*) 'Mfifty=',Mfifty
    write(15,*) 'Mninety=',Mninety
    write(15,*) 'peakC=',peakC
    write(15,*) 'tpeakC=',tpeakC
    write(15,*) 'tailt=',tailt
    write(15,*) 'mss=',mss
    write(15,*) 'mnrrvlm=',mnrrvlm
    write(15,*) 'stdBTC=',stdBTC
    write(15,*) 'skwnss=',skwnss
    close(15)
    count0=count
  endif
endif

```

20 continue

stop
end

```
c *****
c *****subroutines to randomly select values of mass transfer parameters*****
c *****from their cdfs*****
c *****
```

subroutine MTDIST(outmu,outsig)

implicit none
double precision rannum(1),outmu,outsig,amu,bmu,asig,bsig
integer NR

external DRNUN

NR=1

c Obtain a value for mu from its cdf:

c define uniform distribution of MU:

c minimum value = smallest estimated value of mu from field-scale studies,
c - 2 confidence intervals from parameter estimation statistics (H11 MW b3 R1
c "low", from McKenna et al., WRR, in prep.):

amu=-1.51d0

c maximum value = largest estimated value of mu from field-scale studies,
c excluding H19 SWIW results (probably contaminated by slow advection),
c - 2 confidence intervals (H19 MW b7 R1 "high", from McKenna et al., WRR,
c in prep.):

bmu=3.01d0

c generate a random number between 0 and 1:

call DRNUN(NR,rannum(1))

c pick a value off the cdf of mu:

outmu=(bmu-amu)*rannum(1)+amu

c Obtain a value for SIG from its cdf:

c define uniform distribution of sig:

c minimum value = smallest value of sig obtained from field-scale studies
c (H11 MW b3 R2 "high" from McKenna et al., WRR, in prep.):

asig=1.11

c maximum value = from steepest curve that can be fitted to (sampling volume
c vs. estimated sig) data; i.e., $\text{sig}=4.446+0.4574*\ln[\text{sampling volume in m}^3]$,
c from volume3.JNB on topaz. This uses best-fit sig values from parameter
c estimations performed on static diffusion-in/out, bulk static diffusion
c in/out, all SWIW tracer tests performed at H19 except 2nd preliminary
c test (Haggerty et al., WRR, in prep.), all MW tracer tests performed at
c H19 (McKenna et al., WRR, in prep.). Sampling volume is volume of slab,
c total volume of constitutive slabs (for bulk, $\pi*r*r*h$ for SWIW, and
c $0.5*\pi*r*r*h+r*p*h$ for MW (J. Ogintz fax, 3/11/98), where h is thickness of

c Culebra (4.4 m), and r is radial distance from injection well to point at
 c which $C/C_0 \sim 1e-5$ in end-of-pumping concentration profile files produced by
 c STAMMT-R (my SWIW runs, S. McKenna March 14/98 e-mail). Sig extrapolated to
 c regional scale using above empirical curve, taking regional sampling volume
 c to be [travel distance, 3000m] x [formation thickness, 4.4m] x [width of 1D
 c model column, 1m]:

bsig=8.79

c generate a random number between 0 and 1:

call DRNUN(NR,rannum(1))

c pick a value of sig off the cdf:

outsig=(bsig-asig)*rannum(1)+asig

return

end

c *****
 c ***** subroutine to randomly select values of pore water velocity *****
 c ***** and capacity coefficient from their constitutive cdfs *****
 c *****

subroutine TRANSPORTDIST(advporos,PWvel,difporos,capcoef,Dvel)

implicit none

double precision rannum(1),advporos,PWvel,difporos,capcoef,Dvel

double precision dp(7),pdp(7),dpslope,v(101),pv(101),vslope

double precision aap,bap

integer NR,i

external DRNUN

NR=1

c - porosity distributions come from Mike Wallace (samp.xls spreadsheet
 c attachment to March 24(but labelled 11th)/98 e-mail) in Sandia PA group;
 c originally produced by Sandia geohydrology group (M. Wallace, telephone
 c conversation, March 24/98; S. McKenna, April 1/98 e-mail -> memo from L.
 c Meigs and J. McCord, 7/11/96).

c - travel time distribution came from Mike Wallace (samp.xls spreadsheet
 c attachment to March 24(11)/98 e-mail) in Sandia PA group. He developed it
 c using a 2D particle-tracking GW flow code for the case of no mining and
 c no climate change (M. Wallace, March 24/98 telephone conversation, March
 c 26(13)/98 e-mails #1 and #2), and T-fields developed over the
 c years by Sandia and Interra (pilot point method of LaVenue et al.,
 c WRR 25(7), 1989) (M. Wallace, March 26(13)/98 e-mail #2; S. McKenna, April
 c 1/98 e-mail). Code called GRASP-INV was used to generate actual T-fields
 c (M. Wallace, March 26(13)/98 e-mail #2). Travel times are for mean travel
 c distance of 3682 metres, and use constant advective porosity of 0.16
 c (M. Wallace, March 26(13)/98 e-mail #1). I converted travel time dist. to
 c to pore water velocity dist. assuming 0.16 adv. poros. to Darcy velocity
 c dist. in Excel by: Darcy vel. = (3682m/travel time)*0.16 (procedure
 c confirmed by M. Wallace, March 26(13)/98 e-mail #1).

c in STAMMT-LMC3mt.f, only mass transfer parameters are varied in Monte Carlo
 c simulations; all transport parameters set equal to 50th percentile values
 c from aforementioned distributions:

```
Dvel=0.08154d0
PWvel=81.54d0
difporos=0.16d0
advporos=0.001
```

c calculate a value of CAPACITY COEFFICIENT:
 capcoef=difporos/advporos

```
return
end
```

```
c *****
c ***** finding ten and ninety percentile times of each mass BTC *****
c *****
```

```
subroutine PERCENTILE(time,M,TN,Mone,Mten,Mfifty,Mninety,flag3)
```

```
implicit none
double precision time(300),M(300),Mone,Mten,Mfifty,Mninety
double precision xdata(2),ydata(2),invslope,err
integer TN,flag1,i,flag2,flag3,flag4,flag5
```

c flags 1,2,4, and 5 have to do with whether the 10th, 50th, 90th, and 1st
 c percentile masses within the mass BTC have been reached.
 c flag 3 has to do with whether the mass BTC is screwed up by numerical
 c error.

```
flag1=0
flag2=0
flag3=0
flag4=0
flag5=0
```

```
do 200,i=1,TN
```

c testing for whether BTC monotonically increases (within some tolerance):

```
if (M(i).gt.0.075) then
err=M(i)-M(i-1)
```

c if M (mass removed) significantly increases with time, err=positive

```
if (err.lt.(-0.025)) then
flag3=1
goto 210
endif
endif
```

c finding times at which 1%, 10%, 50%, and 90% of the injected mass has been
 c removed from the system. Linear interpolation is used to find the
 c 'exact' time:

```
if ((M(i).gt.0.01).and.(flag5.eq.0)) then
xdata(1)=time(i-1)
```

```

    ydata(1)=M(i-1)
    xdata(2)=time(i)
    ydata(2)=M(i)
    invslope=(xdata(2)-xdata(1))/(ydata(2)-ydata(1))
    Mone=xdata(1)+invslope*(0.01-ydata(1))
    flag5=1
  endif
  if ((M(i).gt.0.10).and.(flag1.eq.0)) then
    xdata(1)=time(i-1)
    ydata(1)=M(i-1)
    xdata(2)=time(i)
    ydata(2)=M(i)
    invslope=(xdata(2)-xdata(1))/(ydata(2)-ydata(1))
    Mten=xdata(1)+invslope*(0.1-ydata(1))
    flag1=1
  endif
  if ((M(i).gt.0.50).and.(flag2.eq.0)) then
    xdata(1)=time(i-1)
    ydata(1)=M(i-1)
    xdata(2)=time(i)
    ydata(2)=M(i)
    invslope=(xdata(2)-xdata(1))/(ydata(2)-ydata(1))
    Mfifty=xdata(1)+invslope*(0.5-ydata(1))
    flag2=1
  endif
  if ((M(i).gt.0.90).and.(flag4.eq.0)) then
    xdata(1)=time(i-1)
    ydata(1)=M(i-1)
    xdata(2)=time(i)
    ydata(2)=M(i)
    invslope=(xdata(2)-xdata(1))/(ydata(2)-ydata(1))
    Mninety=xdata(1)+invslope*(0.9-ydata(1))
    flag4=1
  endif
200 continue
210 continue

return
end

c *****
c **** subroutine to find peak concentration, time to peak concentration, *****
c ****and tailing measure in each concentration BTC calculated by STAMMT-L ****
c *****

subroutine PEAKCONC(time,cncntrtn,TN,peakC,tpeakC,tmpmnt3)

implicit none
double precision time(300),cncntrtn(300),peakC,tpeakC,tmpmnt3
double precision integrand(300),tinitial,tend
double precision x1,x2,y1,y2,slope,lowC,tlowC,tailt
double precision tmpmnt0,tmpmnt1,tmpmnt2

```

```
integer TN,i,j,number,IERR,index
```

```
common/moments/tmpmnt0,tmpmnt1,tmpmnt2,tailt
```

```
external AVINT
```

```
c finding maximum concentration in BTC (peakC) and time at which it occurs
```

```
c (tpeakC):
```

```
peakC=0.0d0
```

```
do 200,i=1,TN
```

```
if (cncntrtn(i).gt.peakC) then
```

```
peakC=cncntrtn(i)
```

```
tpeakC=time(i)
```

```
index=i
```

```
endif
```

```
200 continue
```

```
c finding difference between tpeakC and the time at which concentration  
c decreases to 0.01% of peakC; a simple measure of tailing:
```

```
lowC=0.0001*peakC
```

```
do 204,i=index,TN
```

```
if (cncntrtn(i).lt.lowC) then
```

```
y1=time(i)
```

```
x1=cncntrtn(i)
```

```
y2=time(i-1)
```

```
x2=cncntrtn(i-1)
```

```
slope=(y2-y1)/(x2-x1)
```

```
tlowC=y1+slope*(lowC-x1)
```

```
goto 308
```

```
endif
```

```
204 continue
```

```
308 continue
```

```
tailt=tlowC-tpeakC
```

```
c Finding temporal moments:
```

```
c n.b. AVINT requires at least 3 abscissas between limits of integration
```

```
c lower limit of integration = 1st time in BTC:
```

```
tinitial=time(1)
```

```
c upper limit of integration = last time in BTC:
```

```
tend=time(TN)
```

```
c number of points=TN:
```

```
number=TN
```

```
c Finding 0th temporal moment of the BTC, a measure of mass under the BTC
```

```
c (i.e., duration of pulse if square wave input):
```

```
c calculating quantity to be integrated, C:
```

```
do 270,j=1,TN
```

```
integrand(j)=cncntrtn(j)
```

```
270 continue
```

```
c perform the integration:
```

```

      call AVINT(time,integrand,number,tinitial,tend,tmpmnt0,IERR)

c Finding 1st temporal moment of the BTC, a measure of the mean
c breakthrough time:
c calculating quantity to be integrated, C * t:
      do 280,j=1,TN
          integrand(j)=cncntrtn(j)*time(j)
280    continue
c perform the integration:
      call AVINT(time,integrand,number,tinitial,tend,tmpmnt1,IERR)

c Finding 2nd temporal moment of the BTC, a measure of its variance:
c calculating quantity to be integrated, C * t^2:
      do 275,j=1,TN
          integrand(j)=cncntrtn(j)*time(j)*time(j)
275    continue
c perform the integration:
      call AVINT(time,integrand,number,tinitial,tend,tmpmnt2,IERR)

c Finding 3rd temporal moment of the BTC, a measure of its skewness; gives
c an indication of how much tailing exists:
c calculating quantity to be integrated, C * t^3:
      do 210,j=1,TN
          integrand(j)=cncntrtn(j)*time(j)*time(j)*time(j)
210    continue
c perform the integration:
      call AVINT(time,integrand,number,tinitial,tend,tmpmnt3,IERR)

      return
      end

C*****
C*****SUBROUTINE AVINT (CALLED BY SUBROUTINE
PEAKCONC)*****
C***** performs numerical integration of discrete input *****
C*****

*DECK AVINT
      SUBROUTINE AVINT (X, Y, N, XLO, XUP, ANS, IERR)
C***BEGIN PROLOGUE AVINT
C***PURPOSE Integrate a function tabulated at arbitrarily spaced
C      abscissas using overlapping parabolas.
C***LIBRARY SLATEC
C***CATEGORY H2A1B2
C***TYPE SINGLE PRECISION (AVINT-S, DAVINT-D)
C***KEYWORDS INTEGRATION, QUADRATURE, TABULATED DATA
C***AUTHOR Jones, R. E., (SNLA)
C***DESCRIPTION
C
C Abstract
C AVINT integrates a function tabulated at arbitrarily spaced
C abscissas. The limits of integration need not coincide

```


C with the tabulated abscissas.
 C
 C A method of overlapping parabolas fitted to the data is used
 C provided that there are at least 3 abscissas between the
 C limits of integration. AVINT also handles two special cases.
 C If the limits of integration are equal, AVINT returns a result
 C of zero regardless of the number of tabulated values.
 C If there are only two function values, AVINT uses the
 C trapezoid rule.
 C
 C Description of Parameters
 C The user must dimension all arrays appearing in the call list
 C X(N), Y(N).
 C
 C Input--
 C X - real array of abscissas, which must be in increasing
 C order.
 C Y - real array of functional values. i.e., $Y(I)=FUNC(X(I))$.
 C N - the integer number of function values supplied.
 C N .GE. 2 unless XLO = XUP.
 C XLO - real lower limit of integration.
 C XUP - real upper limit of integration.
 C Must have XLO .LE. XUP.
 C
 C Output--
 C ANS - computed approximate value of integral
 C IERR - a status code
 C --normal code
 C =1 means the requested integration was performed.
 C --abnormal codes
 C =2 means XUP was less than XLO.
 C =3 means the number of X(I) between XLO and XUP
 C (inclusive) was less than 3 and neither of the two
 C special cases described in the Abstract occurred.
 C No integration was performed.
 C =4 means the restriction $X(I+1) .GT. X(I)$ was violated.
 C =5 means the number N of function values was .LT. 2.
 C ANS is set to zero if IERR=2,3,4,or 5.
 C
 C AVINT is documented completely in SC-M-69-335
 C Original program from "Numerical Integration" by Davis &
 C Rabinowitz.
 C Adaptation and modifications for Sandia Mathematical Program
 C Library by Rondall E. Jones.
 C
 C ***REFERENCES R. E. Jones, Approximate integrator of functions
 C tabulated at arbitrarily spaced abscissas,
 C Report SC-M-69-335, Sandia Laboratories, 1969.
 C ***ROUTINES CALLED XERMSG
 C ***REVISION HISTORY (YYMMDD)
 C 690901 DATE WRITTEN
 C 890831 Modified array declarations. (WRB)

```

C 890831 REVISION DATE from Version 3.2
C 891214 Prologue converted to Version 4.0 format. (BAB)
C 900315 CALLs to XERROR changed to CALLs to XERMSG. (THJ)
C 900326 Removed duplicate information from DESCRIPTION section.
C      (WRB)
C 920501 Reformatted the REFERENCES section. (WRB)
C***END PROLOGUE AVINT
C
  DOUBLE PRECISION R3,RP5,SUM,SYL,SYL2,SYL3,SYU,SYU2,SYU3,X1,X2,X3
  1,X12,X13,X23,TERM1,TERM2,TERM3,A,B,C,CA,CB,CC

  DOUBLE PRECISION X(300),Y(300),XLO,XUP,ANS

C***FIRST EXECUTABLE STATEMENT AVINT

  IERR=1
  ANS =0.0
  IF (XLO-XUP) 3,100,200
3 IF (N.LT.2) GO TO 215
  DO 5 I=2,N
  IF (X(I).LE.X(I-1)) GO TO 210
  IF (X(I).GT.XUP) GO TO 6
  5 CONTINUE
  6 CONTINUE
  IF (N.GE.3) GO TO 9
C
C  SPECIAL N=2 CASE
  SLOPE = (Y(2)-Y(1))/(X(2)-X(1))
  FL = Y(1) + SLOPE*(XLO-X(1))
  FR = Y(2) + SLOPE*(XUP-X(2))
  ANS = 0.5*(FL+FR)*(XUP-XLO)
  RETURN
  9 CONTINUE
  IF (X(N-2).LT.XLO) GO TO 205
  IF (X(3).GT.XUP) GO TO 205
  I = 1
  10 IF (X(I).GE.XLO) GO TO 15
  I = I+1
  GO TO 10
  15 INLFT = I
  I = N
  20 IF (X(I).LE.XUP) GO TO 25
  I = I-1
  GO TO 20
  25 INRT = I
  IF ((INRT-INLFT).LT.2) GO TO 205
  ISTART = INLFT
  IF (INLFT.EQ.1) ISTART = 2
  ISTOP = INRT
  IF (INRT.EQ.N) ISTOP = N-1
C
  R3 = 3.0D0

```

```

RP5= 0.5D0
SUM = 0.0
SYL = XLO
SYL2= SYL*SYL
SYL3= SYL2*SYL

```

C

```

DO 50 I=ISTART,ISTOP
X1 = X(I-1)
X2 = X(I)
X3 = X(I+1)
X12 = X1-X2
X13 = X1-X3
X23 = X2-X3
TERM1 = DBLE(Y(I-1))/(X12*X13)
TERM2 = -DBLE(Y(I)) / (X12*X23)
TERM3 = DBLE(Y(I+1))/(X13*X23)
A = TERM1+TERM2+TERM3
B = -(X2+X3)*TERM1 - (X1+X3)*TERM2 - (X1+X2)*TERM3
C = X2*X3*TERM1 + X1*X3*TERM2 + X1*X2*TERM3
IF (I-ISTART) 30,30,35
30 CA = A
   CB = B
   CC = C
   GO TO 40
35 CA = 0.5*(A+CA)
   CB = 0.5*(B+CB)
   CC = 0.5*(C+CC)
40 SYU = X2
   SYU2= SYU*SYU
   SYU3= SYU2*SYU
   SUM = SUM + CA*(SYU3-SYL3)/R3 + CB*RP5*(SYU2-SYL2) + CC*(SYU-SYL)
   CA = A
   CB = B
   CC = C
   SYL = SYU
   SYL2= SYU2
   SYL3= SYU3
50 CONTINUE
   SYU = XUP
   ANS = SUM + CA*(SYU**3-SYL3)/R3 + CB*RP5*(SYU**2-SYL2)
   1 + CC*(SYU-SYL)
100 RETURN
200 IERR=2
   write(28,*) 'AVINT error type',IERR
   RETURN
205 IERR=3
   write(28,*) 'AVINT error type',IERR
   RETURN
210 IERR=4
   write(28,*) 'AVINT error type',IERR
   RETURN
215 IERR=5

```

```

write(28,*) 'AVINT error type',IERR
RETURN
END

```

```

c *****
c ***** subroutine STAMMT-L to calculate breakthrough curves *****
c *****

```

```

subroutine STAMMTL(outmu,outsig,PWvel,capcoef,TN,time,M,cncntrtn)

```

```

c STAMMT-L = Solute Transport and Multirate Mass Transfer in Linear coordinates
c Version 1.0
c
c Roy Haggerty, November, 1997
c
c modified to subroutine for program STAMMT-LMC, Sean Fleming, February, 1998
c
c Dept. of Geosciences
c Oregon State University
c Corvallis, OR
c 97331-5506
c haggertr@ucs.orst.edu

```

```

implicit none
include "stammtL.incl"
integer i,j,kmax,opt,Ltime,Lz,TNS,idef,lcom,mrct,ic,
& bc,TNI,iparam(6),ocm
double precision rP,X,tfac,disc,relerr,Rm,btot,mse,rmse,tp,sig,
& derf,sum,dnorin,dnordf,mu,L,xx,alphaL,vx,Tmax,Tmin,ts,msin
double precision bet(nm),omega(nm),dp(nt),tdp(nt),
& xguess(nx),fjac(nt,nx),xscale(nx),fscale(nt),rparam(7),
& xf(nx),serr(nt),cov(nx,nx),invcov(nx,nx),T(nt),C(nt),
& eig(nx),tdi(ni),cdi(ni),Ms(nt),sim(nt)
character*40 parameterfile,datafileOUT,multirateseriesOUT,
& covariance_matrix,outconc,multirateseriesIN,datafileIN,
& outmass,lsq_progress
complex*16 fc0,fc1,fm0,fm1

```

```

c my change: declare input from Monte Carlo:
double precision outmu,outsig,PWvel,capcoef
c my change: declare output to Monte Carlo:
double precision time(300),M(300),cncntrtn(300)
integer TN

```

```

external fc0,fc1,obj,dnorin,dnordf,derf,fm0,fm1,msin
common/stuff/rP,X,Rm,tfac,bet,omega,btot,tp,vx
common/other/dp,tdp,relerr,disc
common/int/ kmax,TNS,lcom,idef,mrct,ic,bc,TNI,ocm,opt
common/cinit/ tdi,cdi
common/name/ lsq_progress

```

```

c*****
  mrct = 0

c Open necessary files:
  open(10,file='STAMMT-L.prj')
  read(10,10) parameterfile
  read(10,10) datafileIN
  read(10,10) datafileOUT
  read(10,10) multirateseriesIN
  read(10,10) multirateseriesOUT
  read(10,10) outconc
  read(10,10) outmass
  read(10,10) covariance_matrix
  read(10,10) lsq_progress
10 format (A)

  open(9,file='ERRORS')
  open(21,file=parameterfile)
  open(23,file=datafileIN)
  open(24,file=datafileOUT)
  open(25,file=multirateseriesOUT)
  open(26,file=multirateseriesIN)
  open(27,file=covariance_matrix)
  open(30,file=outconc)
  open(31,file=outmass)

c Read in initial variables and parameters:
  read(21,*) L           !Length of system
  read(21,*) xx         !Distance from Injection to Measurement
  read(21,*) alphaL    !Longitudinal dispersivity
  read(21,*) vx        !velocity
  read(21,*) Rm        !retardation factor for mobile zone
  read(21,*) btot      !total capacity coefficient
  read(21,*) mu        !nat. log of geometric mean of Da/a^2 (or alpha, if idef=2)
  read(21,*) sig       !std. dev. of logs of Da/a^2. Ignored if idef=1,2,or3
  read(21,*) Ltime     !use (t,C) input file to determine sim. times (set=0) or generate times
(set=1)
  read(21,*) Lz        !if Ltime=1: constant time (set=0) increment, or constant ln(time)
increment (set=1)
  read(21,*) Tmin      !if Ltime=1: min. sim. time (i.e., first simulated time)
  read(21,*) Tmax      !if Ltime=1: max. sim. time (i.e., last simulated time)
  read(21,*) ic        !Initial condition. Zero conc. (ic=0); Equilibrium, saturated (ic=1)
  read(21,*) bc        !Boundary condition. No input (bc=0); Dirac pulse (bc=1); Square pulse
(bc=2); Time-varying bdy. conc. (bc=3)
  read(21,*) tp        !If bc=1, then 0th temp. moment; If bc=2, then time (length) of conc.
pulse.
  read(21,*) TNI       !Number of input conc. data points (needed ONLY if bc=3). Max = 100.
  read(21,*) TNS       !number of time vs. conc. data points (or number of simulated times
desired). Max = 300
  read(21,*) idef      !idef, 0=Lognormal distribution of diffusion coefs;1=spherical
diffusion;2=single-rate first-order mass transfer; 3=Read in distribution of rate coefficients; 4=User-
defined distribution

```

```

read(21,*) disc !max. expected discontinuity in Laplace
read(21,*) kmax !max. number of iterations in Laplace
read(21,*) relerr !relative error desired
read(21,*) opt !run an optimization or simulation
read(21,*) ocm !compare concentrations (ocm=0) or mass (ocm=1)
read(21,*) lcom !compare arithmetic values (set = 0) or logs of values (set=1) in estimation

```

c my change: override input from input parameter file, replace with values
c sent from the calling program:

```

mu=outmu
sig=outsig
btot=capcoef
vx=PWvel

```

c Do some checks on parameters:

```

call error(xx,L,Ltime,Lz)

```

c Create nondimensional variables to be used later.

```

rP = L/alphaL
X = xx/L
tfac = vx/L

```

c Read in output concentration vs. time data if Ltime = 0

```

if (Ltime.eq.0) then
  do 20,i=1,TNS
    read(24,*,end=500),tdp(i),dp(i)
  20  continue
  goto 501
500  write(9,*)'Either the value of TNS is incorrect or the file',
&  'datafileOUT,' has an error. Apparently TNS should be',(i-1),
&  'If this number is not correct, please halt the simulation.
&  'Please correct TNS or the file before the next run.'
  TNS = i-1
501  continue
  elseif (Ltime.eq.1) then
    if (Lz.eq.0) then
      ts = (Tmax-Tmin)/dble(TNS-1)
      do 21,i=1,TNS
        tdp(i) = Tmin+ts*dble(i-1)
      21  continue
      do 22,i=(TNS+1),nt
        tdp(i) = Tmax
      22  continue
    elseif (Lz.eq.1) then
      ts = (log(Tmax)-log(Tmin))/dble(TNS-1)
      do 23,i=1,TNS
        tdp(i) = exp(log(Tmin)+ts*dble(i-1))
      23  continue
    else
      write(9,*)'Lz is neither 0 nor 1. Please set and restart.'
      stop
    endif

```

```

else
  write(9,*)'Ltime is neither 0 nor 1. Please set and restart.'
  stop
endif

c Fill in extra time-slots with the last time.
do 24,i=(TNS+1),nt
  tdp(i) = tdp(TNS)
24 continue

c Read in input concentration vs. time data if bc = 3
if (bc.eq.3) then
  do 520,i=1,TNI
    read(23,*,end=530),tdi(i),cdi(i)
520 continue
  goto 540
530 write(9,*)'Either the value of TNI is incorrect or the file',
& datafileIN,' has an error. Apparently TNI should be',(i-1),
& 'If this number is not correct, please halt the simulation.
& Please correct TNI or the file before the next run.'
  TNI = i-1
  if (TNI.le.1) then
    write(9,*)' '
    write(9,*)'There appears to be only',TNI,' input conc.'
    write(9,*)'There must be at least 2 input concentrations.'
    write(9,*)'Simulation stopped.'
    stop
  endif
540 continue
endif

c If an estimation run is being done, then set up the necessary
c arrays and do the estimation:
if (opt.eq.0) then

c Set up initial guesses for estimation in log-space:
xguess(1) = log(btot)
xguess(2) = mu
xguess(3) = log(sig)
xguess(4) = log(Rm)
xguess(5) = log(rP)

c Set up scaling and other optimization parameters (see
c IMSL):
do 27,i=1,nx
  xscale(i) = 1.d0
27 continue
do 28,i=1,nt
  fscale(i) = 1.d0
28 continue
call du4lsf(iparam,rparam)
iparam(2) = 4

```

```

c Write headers to least squares progress file:
  open(28,file=lsq_progress)
  write(28,'(6A15)')'btot','mu','sig','Rm','rP','Sum of Err^2'
  close(28)

c Go to nonlinear least squares routine:
  call dnlslf(obj,nt,nx,xguess,xscale,fscale,iparam,
  &          rparam,xf,serr,fjac,nt)

c  call dbclsf (obj,nt,nx,xguess, ITP, XLB, XUB, XS, FSCALE,
c  &          IPARAM, RPARAM, X, FVEC, FJAC, LDFJAC)

c Calculate values of covariance matrix and its eigenvalues
c (note that these are not yet covariances, and that when
c they are below, several important assumptions are involved):
  call dmxtxf(nt,nx,fjac,nt,nx,invcov,nx)
  call dlinrg(nx,invcov,nx,cov,nx)
  call devlsf (nx,cov,nx,eig)

  btot = exp(xf(1))
  mu = xf(2)
  sig = exp(xf(3))
  Rm = exp(xf(4))
  rP = exp(xf(5))
endif

c Set up the multirate series:
  call multirate(mu,sig)
  mrct = mrct+1

c Write out mass transfer rate coefs.
  write(25,'(3A15)') 'alpha(i) [1/T]','beta(i) [-]','Cum. Sum [-]'
  sum = 0.d0
  do 40,i=1,nm
    sum = sum + bet(i)
    write(25,45) omega(i)*tfac/Rm,bet(i),sum
40  continue
45  format(3d15.7)

c Make nondimensional times.
  do 64,i=1,nt
    T(i) = tdp(i)*tfac/Rm
64  continue
  do 65,i=1,ni
    tdi(i) = tdi(i)*tfac/Rm
65  continue

c Do inverse Laplace transform at times needed to calculate
c concentrations:
  if (ic.eq.0) then
    call dinlap (fc0,nt,T,disc,relerr,kmax,C)

```



```

else
  call dinlap (fc1,nt,T,disc,relerr,kmax,C)
endif

c Do inverse Laplace transform at times needed to calculate
c mass fraction:
  if (ic.eq.0) then
    call dinlap (fm0,nt,T,disc,relerr,kmax,Ms)
    do 300,i=1,TNS
      Ms(i) = Ms(i)/msin()
300  continue
  else
    call dinlap (fm1,nt,T,disc,relerr,kmax,Ms)
    do 310,i=1,TNS
      Ms(i) = 1.d0-Ms(i)
310  continue
  endif

c If optimization run:
  if (opt.eq.0) then

c Load the simulated values of mass OR concentration into
c an array called "sim". The array loaded in depends on
c whether the estimation was done from mass or concentration
c data.

  if (ocm.eq.0) then
    do 320,i=1,TNS
      sim(i) = C(i)
320  continue
  else
    do 330,i=1,TNS
      sim(i) = Ms(i)
330  continue
  endif

c Calculate mean squared error and root mse. Calculate final
c covariance values:
  mse = 0.d0
  if (lcom.ne.1) then
    do 70,i=1,TNS
      mse = mse + (dp(i)-sim(i))*(dp(i)-sim(i))
70  continue
  else
    do 72,i=1,TNS
      if ((dp(i).ne.0.d0).and.(sim(i).gt.0.d0)) then
        mse = mse + (log(dp(i)/sim(i)))**2
      endif
72  continue
  endif
  rmse = sqrt(mse/(dble(TNS-nx)))
  mse = rmse*rmse

```

```

    if (opt.eq.0) then
      do 76,i=1,nx
        do 74,j=1,nx
          cov(i,j) = cov(i,j)*mse
74      continue
76      continue
    endif

c Print out results on covariance matrix:
    write(27,80) 'RMSE = ',rmse
    write(27,'(/)')
    write(27,'(A9,2A15)')'Param.', 'Std. Error'
    write(27,80) 'btot = ',btot,sqrt(cov(1,1))
    write(27,80) 'u* = ',mu,sqrt(cov(2,2))
    write(27,80) 'sig = ',sig,sqrt(cov(3,3))
    write(27,80) 'Rm = ',Rm,sqrt(cov(4,4))
    write(27,80) 'rP = ',rP,sqrt(cov(5,5))
    write(27,'(//)')
80  format(A,2d15.5)
    write(27,'(A)') 'Covariance Matrix. nx x nx.'
    write(27,'(A)')'Diagonals contain the square of the std. error.'
    do 90,i=1,nx
      write(27,110) (cov(i,j),j=1,nx)
90  continue
110 format(7d15.5)
    write(27,'(/)')
    write(27,'(A)') 'Eigenvalues of Covariance Matrix'
    write(27,110) (eig(j),j=1,nx)

c Print out results on conc. and mass. Print data with
c the associated simulated values (i.e., if data are conc.,
c print with simulated conc.; if data are mass, print with
c simulated mass:
    if (ocm.eq.0) then
      write(30,80) 'RMSE = ',rmse
      write(30,80) 'btot = ',btot
      write(30,80) 'u* = ',mu
      write(30,80) 'sig = ',sig
      write(30,80) 'Rm = ',Rm
      write(30,80) 'rP = ',rP

      write(30,'(3A15)') 'Time','C/Co Sim.','C/Co Data'
      do 130,i=1,TNS
        write(30,120) tdp(i),C(i),dp(i)
120  format(3d15.5)
130  continue
      write(31,'(2A15)') 'Time','Mass Frac.'
      do 135,i=1,TNS
        write(31,120) tdp(i),Ms(i)
135  continue
    else
      write(31,80) 'RMSE = ',rmse

```

```

write(31,80) 'btot = ',btot
write(31,80) 'u* = ',mu
write(31,80) 'sig = ',sig
write(31,80) 'Rm = ',Rm
write(31,80) 'rP = ',rP
write(31,(3A15)) 'Time','M Frac. Sim.','Mass Frac. Data'
do 140,i=1,TNS
  write(31,120) tdp(i),Ms(i),dp(i)
140  continue
  write(30,(2A15)) 'Time','C/Co'
  do 145,i=1,TNS
    write(30,120) tdp(i),C(i)
145  continue
  endif

c If forward run only:
  else
    write(30,(2A15)) 'Time','C/Co'
    do 150,i=1,TNS
      write(30,120) tdp(i),C(i)
150  continue
      write(31,(2A15)) 'Time','Mass Frac.'
      do 160,i=1,TNS
        write(31,120) tdp(i),Ms(i)
160  continue
      endif

c my change: write calculated tdp(i),Ms(i),C(i) to time(i),M(i),cncntrtn,
c and TNS to TN:
      do 204,i=1,TNS
        time(i)=tdp(i)
        M(i)=Ms(i)
        cncntrtn(i)=C(i)
204  continue
      TN=TNS

close(10)
close(21)
close(23)
close(24)
close(25)
close(26)
close(27)
close(30)
close(31)
close(9)

return
end

```

c*****

c This subroutine calculates the residuals (the difference
 c between the data value and the model value) for a given
 c set of parameters.

c dinlap IMSL inverse Laplace routine
 c nd - dummy variable
 c np - dummy variable
 c sct - sum of squares of residuals

```

subroutine obj(nd,np,xf,serr)
implicit NONE
include "stammtL.incl"
integer kmax,np,nd,i,TNS,lcom,idef,mrct,ic,bc,TNI,ocm,opt
double precision rP,X,tfac,disc,relerr,Rm,btot,sct,tp,
& sig,mu,vx,msin
double precision sim(nt),T(nt),bet(nm),omega(nm),dp(nt),
& tdp(nt),xf(nx),serr(nt)
complex*16 fc0,fc1,fm0,fm1
logical difnan
character*40 lsq_progress
external fc0,fc1,fm0,fm1,dinlap,difnan,msin
common/stuff/rP,X,Rm,tfac,bet,omega,btot,tp,vx
common/other/dp,tdp,relerr,disc
common/int/ kmax,TNS,lcom,idef,mrct,ic,bc,TNI,ocm,opt
common/name/lsq_progress

```

c Set parameters to values called for by IMSL routine:

```

btot = exp(xf(1))
mu = xf(2)
sig = exp(xf(3))
Rm = exp(xf(4))
rP = exp(xf(5))
do 20,i=1,nt
  T(i) = tdp(i)*tfac/Rm
20 continue

```

c Set up the multirate series :

```

call multirate(mu,sig)
mrct = mrct+1

```

c Do inverse on mass or concentration? Do inverse Laplace transform
 c at times needed:

c If CONCENTRATION and zero initial conc., then:

```

if ((ic.eq.0).and.(ocm.eq.0)) then
  call dinlap (fc0,nt,T,disc,relerr,kmax,sim)

```

c If CONCENTRATION and equilibrium initial conditions, then:

```

elseif ((ic.eq.1).and.(ocm.eq.0)) then
  call dinlap (fc1,nt,T,disc,relerr,kmax,sim)

```

c If MASS and zero initial conc., then:

```

elseif ((ic.eq.0).and.(ocm.eq.1)) then
  call dinlap (fm0,nt,T,disc,relerr,kmax,sim)
  do 30,i=1,TNS
    sim(i) = sim(i)/msin()
30  continue

c If MASS and equilibrium initial conditions, then:
elseif ((ic.eq.1).and.(ocm.eq.1)) then
  call dinlap (fm1,nt,T,disc,relerr,kmax,sim)
  do 40,i=1,TNS
    sim(i) = 1.d0-sim(i)
40  continue

else
  write(9,*)'ic and ocm are not set properly. Must be 0 or 1.'
  stop
endif

c Calculate values of residuals and sum of squared residuals:
sct = 0.d0
if (lcom.ne.1) then
  do 70,i=1,TNS
    serr(i) = sim(i)-dp(i)
    if(difnan(serr(i))) then
      serr(i) = 1.d2
      write(9,*)'Simulation value #',i,' returned as NaN,'
&    'continuing'
    endif
    sct = sct + serr(i)*serr(i)
70  continue
else
  do 80,i=1,TNS
    if (dp(i).ne.0.d0) then
      serr(i) = log(sim(i))-log(dp(i))
    else
      serr(i) = 0.d0
    endif
    if(difnan(serr(i))) then
      serr(i) = 1.d2
      write(9,*)'Simulation value #',i,' returned as NaN,'
&    'continuing'
    endif
    sct = sct + serr(i)*serr(i)
80  continue
  endif
  do 90,i=(TNS+1),nt
    serr(i) = 0.d0
90  continue

c Write status of run to screen:
open(28,file=lsq_progress,access='append')
write(28,'(8d15.5)') btot,mu,sig,Rm,rP,sct

```

```

close(28)

return
end

c*****
complex*16 function fc0 (s)
implicit NONE
include "stammtL.incl"
integer i,kmax,TNS,lcom,idef,mrct,ic,bc,TNI,ocm,opt
double precision rP,X,Rm,tfac,bet(nm),omega(nm),btot,tp,tdi(ni),
& cdi(ni),dc,dt,vx
complex*16 s,cb0,r,rr,rnum,rden,front
common/stuff/rP,X,Rm,tfac,bet,omega,btot,tp,vx
common/int/ kmax,TNS,lcom,idef,mrct,ic,bc,TNI,ocm,opt
common/cinit/ tdi,cdi

c Laplace-domain initial conditions (Dirac input):
if (bc.eq.1) then
  cb0 = tp*tfac/Rm

c Laplace-domain initial conditions (step input):
elseif (bc.eq.2) then
  cb0 = (1.d0-exp(-s*tp*tfac/Rm))/s

c Laplace-domain initial conditions (general input):
elseif (bc.eq.3) then
  cb0 = 0.d0
  do 5,i=1,TNI-1
    dc = cdi(i+1)-cdi(i)
    dt = tdi(i+1)-tdi(i)
    cb0 = cb0 + ((dc+cdi(i)*dt*s)*exp(-s*tdi(i))
& - (dc+cdi(i+1)*dt*s)*exp(-s*tdi(i+1)))/(s*s*dt)
  5 continue
endif

c Calculate value of reaction term (r) and total reaction
c term (rr):
r = 0.d0
do 10,i=1,nm
  r = r + bet(i)*omega(i)/(s+omega(i))
10 continue
rr = sqrt(rP*(rP+4.d0*s*(1.d0+r)))

c Calculate value of Laplace-domain solution (f) for
c particular value of s. If the real part of rr is greater
c than 37.0, use approximation:
if (dble(rr).lt.37.d0) then
  rnum = rP*(exp(rr)-exp(rr*X)) + rr*(exp(rr)+exp(rr*X))
  rden = (exp(rr)-1.d0)*(rP+rr)*(rP+rr)
else
  rnum = rP*(1.d0-exp(rr*(X-1.d0))) +

```

```

&      rr*(1.d0+exp(rr*(X-1.d0)))
      rden = (rP+rr)*(rP+rr)
endif
front = cb0*2.d0*rP*exp((rP-rr)*X/2.d0)

fc0 = front*rnum/rden

return
end

```

```
c*****
```

```

complex*16 function fc1 (s)
implicit NONE
include "stammtL.incl"
integer i
double precision rP,X,Rm,tfac,bet(nm),omega(nm),btot,tp,vx
complex*16 s,r,rr,rnum,rden,front
common/stuff/rP,X,Rm,tfac,bet,omega,btot,tp,vx

r = cmplx(0.d0,0.d0)
do 10,i=1,nm
  r = r + bet(i)*omega(i)/(s+omega(i))
10 continue
rr = sqrt(rP*(rP+4.d0*s*(1.d0+r)))
front = 1.d0/s
if (dble(rr).lt.37.d0) then
  rnum = 2.d0*rP*(-(rP-rr)*exp((rP+rr)*X*0.5d0)
&      + (rP+rr)*exp(rr+(rP-rr)*X*0.5d0))
  rden = (rP-rr)*(rP-rr) - (rP+rr)*(rP+rr)*exp(rr)
else
  rnum = 2.d0*rP*((rP-rr)*exp(-rr+(rP+rr)*X*0.5d0)-
&      (rP+rr)*exp((rP-rr)*X*0.5d0))
  rden = (rP+rr)*(rP+rr)
endif
fc1 = front*(1.d0 + rnum/rden)

return
end

```

```
c*****
```

```

complex*16 function fm0 (s)
implicit NONE
include "stammtL.incl"
integer i,kmax,TNS,lcom,idef,mrct,ic,bc,TNI,ocm,opt
double precision rP,X,Rm,tfac,bet(nm),omega(nm),btot,tp,tdi(ni),
& cdi(ni),dc,dt,vx
complex*16 s,cb0,r,rr,rnum,rden,front
common/stuff/rP,X,Rm,tfac,bet,omega,btot,tp,vx
common/int/ kmax,TNS,lcom,idef,mrct,ic,bc,TNI,ocm,opt
common/cinit/ tdi,cdi

```

c Laplace-domain initial conditions (Dirac input):

```

if (bc.eq.1) then
  cb0 = tp*tfac/Rm

c Laplace-domain initial conditions (step input):
  elseif (bc.eq.2) then
    cb0 = (1.d0-exp(-s*tp*tfac/Rm))/s

c Laplace-domain initial conditions (general input):
  elseif (bc.eq.3) then
    cb0 = 0.d0
    do 5,i=1,TNI-1
      dc = cdi(i+1)-cdi(i)
      dt = tdi(i+1)-tdi(i)
      cb0 = cb0 + ((dc+cdi(i)*dt*s)*exp(-s*tdi(i))
&      - (dc+cdi(i+1)*dt*s)*exp(-s*tdi(i+1)))/(s*s*dt)
5    continue
    endif

c Calculate value of reaction term (r) and total reaction
c term (rr):
  r = 0.d0
  do 10,i=1,nm
    r = r + bet(i)*omega(i)/(s+omega(i))
10  continue
  rr = sqrt(rP*(rP+4.d0*s*(1.d0+r)))

c Calculate value of Laplace-domain solution (f) for
c particular value of s. If the real part of rr is greater
c than 37.0, use approximation:
  if (dble(rr).lt.37.d0) then
    rnum = rP*(exp(rr)-exp(rr*X)) + rr*(exp(rr)+exp(rr*X))
    rden = (exp(rr)-1.d0)*(rP+rr)*(rP+rr)
  else
    rnum = rP*(1.d0-exp(rr*(X-1.d0))) +
&    rr*(1.d0+exp(rr*(X-1.d0)))
    rden = (rP+rr)*(rP+rr)
  endif
  front = cb0*2.d0*rP*exp((rP-rr)*X/2.d0)

  fm0 = front*rnum/(rden*s)

return
end

c*****
complex*16 function fm1 (s)
implicit NONE
include "stammtL.incl"
integer i
double precision rP,X,Rm,tfac,bet(nm),omega(nm),btot,tp,vx
complex*16 s,r,rr,rnum,rden,front
common/ stuff/ rP,X,Rm,tfac,bet,omega,btot,tp,vx

```



```

r = cmplx(0.d0,0.d0)
do 10,i=1,nm
  r = r + bet(i)*omega(i)/(s+omega(i))
10 continue
rr = sqrt(rP*(rP+4.d0*s*(1.d0+r)))

front = 1.d0/(s*s*(1.d0+btot))
if (dble(rr).lt.37.d0) then
  rnum = 2.d0*rP*(-(rP-rr)*exp((rP+rr)*X*0.5d0)
&      + (rP+rr)*exp(rr+(rP-rr)*X*0.5d0))
  rden = (rP-rr)*(rP-rr) - (rP+rr)*(rP+rr)*exp(rr)
else
  rnum = 2.d0*rP*((rP-rr)*exp(-rr+(rP+rr)*X*0.5d0)-
&      (rP+rr)*exp((rP-rr)*X*0.5d0))
  rden = (rP+rr)*(rP+rr)
endif
fm1 = front*(1.d0 + rnum/rden)

return
end

```

c*****

c This subroutine defines the zeroth moment of the injected concentration,
c to be used in constructing the normalized mass fraction removed. This
c is only applicable in the case of a non-zero boundary condition (bc>0).

```

double precision function msin()
implicit NONE
include "stammtL.incl"
integer kmax,i,TNS,lcom,idef,mrct,ic,bc,TNI,ocm,opt
double precision rP,X,tfac,Rm,btot,tp,vx,dc,dt
double precision bet(nm),omega(nm),tdi(ni),cdi(ni)
common/stuff/rP,X,Rm,tfac,bet,omega,btot,tp,vx
common/int/ kmax,TNS,lcom,idef,mrct,ic,bc,TNI,ocm,opt
common/cinit/ tdi,cdi

msin = 0.d0
c If Dirac input or step input:
if ((bc.eq.1).or.(bc.eq.2)) then
  msin = tp*tfac/Rm

c If general input:
elseif (bc.eq.3) then
  do 5,i=1,TNI-1
    dc = cdi(i+1)+cdi(i)
    dt = tdi(i+1)-tdi(i)
    msin = msin + dc*dt/2.d0
5 continue
endif

return

```

```

end
c*****
c
c This subroutine fills in the multirate series. If ndef=0, the series
c corresponds to a lognormal distribution of diffusion rate coefficients.
c If ndef = 1, the series corresponds to spherical diffusion. If ndef = 2,
c the multirate series corresponds to single-rate first-order mass transfer.
c If ndef=3, the multirate series is read in from a file (unit 26). If
c ndef=4, the series definition is user-defined in the subroutine mrdef.

subroutine multirate(mu,sig)
implicit NONE
include "stammtL.incl"
integer kmax,i,j,TNS,lcom,ndef,mrct,ic,bc,TNI,ocm,opt
double precision rP,X,tfac,Rm,btot,tp,
& step,sig,dnorin,stepov,up,low,b,derf,sum,jjpp,sq2sig,
& jjpp4,mu,mud,vx
double precision bet(nm),omega(nm),alpha(nm)
external dnorin,derf
common/stuff/rP,X,Rm,tfac,bet,omega,btot,tp,vx
common/int/ kmax,TNS,lcom,ndef,mrct,ic,bc,TNI,ocm,opt

if (ndef.eq.0) then

mud = mu - log(tfac/Rm)

omega(nm)=Log(50.66059182d0)
omega(1) =mud+sig*dnorin(1.d-8)
step = (omega(nm)-omega(1))/dble(nm-1)
do 30,i=2,(nm-1)
omega(i) = omega(1)+step*dble(i-1)
30 continue
do 35,i=1,nm
omega(i) = pi*pi*exp(omega(i))
bet(i) = 0.d0
35 continue

step = exp(step*0.5d0)
stepov = 1.d0/step
sq2sig = 1.d0/(sqrt(2.d0)*sig)
do 50,j=1,1000
jjpp = dble(2*j-1)*dble(2*j-1)*pi*pi
jjpp4 = 4.d0/jjpp
do 40,i=2,(nm-1)
up = Log(jjpp4*omega(i)*step)
low = Log(jjpp4*omega(i)*stepov)
b = jjpp4*(dErf((mud-low)*sq2sig)-
& dErf((mud-up)*sq2sig))
bet(i) = bet(i) + b
40 continue
up = Log(jjpp4*omega(1)*step)
b = jjpp4*(1.d0 - dErf((mud-up)*sq2sig))

```

```

bet(1) = bet(1) + b
low = Log(jjpp4*omega(nm)*stepov)
b = jjpp4*(dErf((mud-low)*sq2sig) + 1.d0)
bet(nm) = bet(nm) + b
50  continue

sum = 0.d0
do 60,i=1,nm
  bet(i) = btot*bet(i)
  sum = sum+bet(i)
60  continue
bet(nm) = bet(nm)+btot-sum

elseif (idef.eq.1) then
mud = mu - log(tfac/Rm)
sum = 0.d0
do 70,i=1,nm
  omega(i) = exp(mud)*dble(i*i)*pi*pi
  bet(i) = 6.d0*btot/(dble(i*i)*pi*pi)
  sum = sum + bet(i)
70  continue
bet(nm) = bet(nm) + (btot-sum)

elseif (idef.eq.2) then
mud = mu - log(tfac/Rm)
do 80,i=1,nm
  omega(i) = exp(mud)
  bet(i) = btot/dble(nm)
80  continue

elseif ((idef.eq.3).and.(mrct.eq.0)) then
do 100,i=1,nm
  read(26,*,end=101) alpha(i),bet(i)
  omega(i) = alpha(i)*Rm/tfac
100  continue
goto 102
101  write(9,*)'It appears that the file containing the multirate'
  write(9,*)'series to be read in does not contain enough'
  write(9,*)'values. This file should contain',nm,' lines.'
  write(9,*)'Please either (1) correct this error; or (2)'
  write(9,*)'change idef such that the multirate series is'
  write(9,*)'not read in.'
  write(9,*)''
  write(9,*)'Simulation stopped.'
  stop
102  continue

elseif (idef.eq.4) then
  call mrdef(mu,sig)
endif

```

```

return
end

c*****
c
c This subroutine fills in the multirate series if the user wishes to
c define it. This allows for possibilities for any multirate series that
c the user wishes to define, and it may be defined on each iteration during
c estimation. If the user wishes to define a parametric distribution, the
c parameters mu and sig may be used (normally these are the parameters of the
c lognormal distribution, but they could be used to define, for example, a
c gamma distribution of first-order rate coefficients). This subroutine
c is only activated if ideo=2. Note that common blocks have already been
c set up to import some of the most important information - the Peclet
c number (rP), the rate of transport (tfac), the mobile-zone retardation
c factor (Rm), the total capacity coefficient (btot), the length of the
c input concentration pulse (tp), the vector of capacity coefficients (bet)
c and the vector of nondimensional rate coefficients (omega).

      subroutine mrdef(mu,sig)
      implicit NONE
      include "stammtL.incl"
      integer kmax,i,TNS,lcom,ideo,mrct,ic,bc,TNI,ocm,opt
      double precision rP,X,tfac,Rm,btot,tp,sig,mu,vx
      double precision bet(nm),omega(nm),alpha(nm)
      common/stuff/rP,X,Rm,tfac,bet,omega,btot,tp,vx
      common/int/ kmax,TNS,lcom,ideo,mrct,ic,bc,TNI,ocm,opt

c If ideo=4, the user must define the vectors bet(i) and one of either
c omega(i) or alpha(i). alpha(i) is dimensional (1/T) and omega(i) is
c nondimensional.

c An example of such definition is given here, where the
c values of alpha(i) and bet(i) are simply read in from file # 26.

      do 20,i=1,nm
         read(26,*) alpha(i),bet(i)
20    continue

c A second example of defining alpha(i) and bet(i) is given. In this case,
c we define all rate coefficients to be the same value (equal to the rate of
c solute transport, such that the Damkohler number is on the order of 1).
c Defining all rate coefficients with the same numerical value is equivalent
c to using a standard first-order model with a single rate coefficient:

c   do 30,i=1,nm
c     alpha(i) = tfac/Rm
c     bet(i) = btot/dble(nm)
c30  continue

```

```

c If the user defines alpha(i), the user MUST use the following loop to
c define omega(i):
  do 1000,i=1,nm
    omega(i) = alpha(i)*Rm/tfac
  1000 continue

  return
end

```

```

c*****

```

```

c This subroutine checks for errors and inconsistencies within the
c input file. If it finds an error it prints an error message. In
c some cases, it is possible to recover from the error; in other cases
c the simulation must be halted.

```

```

subroutine error(xx,L,Ltime,Lz)
implicit NONE
include "stammtL.incl"
integer kmax,TNS,lcom,idef,mrct,ic,bc,TNI,Ltime,Lz,ocm,opt
double precision xx,L,rP,X,Rm,tfac,bet(nm),omega(nm),btot,tp,vx
common/int/ kmax,TNS,lcom,idef,mrct,ic,bc,TNI,ocm,opt
common/stuff/rP,X,Rm,tfac,bet,omega,btot,tp,vx

```

```

if ((ic.eq.0).and.(bc.eq.0)) then
  write(9,*)'You have set the intitial conditions to zero'
  write(9,*)'(ic=0) AND have set the input boundary'
  write(9,*)'condition to have zero input (bc=0). The'
  write(9,*)'solution is therefore zero output.'
  write(9,*)' '
  write(9,*)'Simulation stopped.'
  stop
endif

```

```

if ((ic.eq.1).and.(bc.ne.0)) then
  write(9,*)'You have set the intitial conditions to'
  write(9,*)'equilibrium, saturated conditions (ic=1)'
  write(9,*)'and have requested a non-zero input at'
  write(9,*)'the boundary (bc>0). Currently these are'
  write(9,*)'not compatible options in STAMMT-L 1.0.'
  write(9,*)'Please choose either a zero initial condition'
  write(9,*)'(ic=0) or an input at the boundary of zero'
  write(9,*)'(bc=0) and restart.'
  write(9,*)' '
  write(9,*)'Simulation stopped.'
  stop
endif

```

```

if ((bc.eq.0).and.(tp.gt.0.d0)) then
  write(9,*)'You have requested a zero input boundary'
  write(9,*)'condition (bc=0), but you have chosen to'
  write(9,*)'make the length of the injection period'
  write(9,*)'greater than zero. (tp =',tp,').'

```

```
    write(9,*)'The simulation will ignore this value of
    write(9,*)'tp.'
    write(9,*)' '
    write(9,*)'Simulation continuing.'
endif

if (xx.gt.L) then
    write(9,*)'xx cannot be larger than L.'
    write(9,*)'Simulation stopped.'
    stop
endif

if ((ic.ne.0).and.(ic.ne.1)) then
    write(9,*)'ic not set properly. Must be 0 or 1.'
    write(9,*)' '
    write(9,*)'Simulation stopped.'
    stop
endif

if ((bc.gt.3).or.(bc.lt.0)) then
    write(9,*)'bc not set properly. Must be 0,1,2, or 3.'
    write(9,*)' '
    write(9,*)'Simulation stopped.'
    stop
endif

if ((Ltime.ne.0).and.(Ltime.ne.1)) then
    write(9,*)'Ltime not set properly. Must be 0 or 1.'
    write(9,*)' '
    write(9,*)'Simulation stopped.'
    stop
endif

if ((Ltime.eq.1).and.(Lz.ne.0).and.(Lz.ne.1)) then
    write(9,*)'Lz not set properly. Must be 0 or 1.'
    write(9,*)' '
    write(9,*)'Simulation stopped.'
    stop
endif

if ((TNI.gt.ni).and.(bc.eq.3)) then
    write(9,*)'TNI is',TNI,',. TNI must not be more than',ni,', '
    write(9,*)' '
    write(9,*)'Simulation stopped.'
    stop
endif

if ((TNI.le.1).and.(bc.eq.3)) then
    write(9,*)'TNI must be greater than 1.'
    write(9,*)' '
    write(9,*)'Simulation stopped.'
    stop
endif
```

```
endif

if (TNS.gt.nt) then
  write(9,*)'TNS is',TNS,'. TNS must not be more than',nt,'.'
  write(9,*)''
  write(9,*)'Simulation stopped.'
  stop
endif

if ((ocm.ne.0).and.(ocm.ne.1)) then
  write(9,*)'ocm not set properly. Must be 0 or 1.'
  write(9,*)''
  write(9,*)'Simulation stopped.'
  stop
endif

if ((lcom.ne.0).and.(lcom.ne.1)) then
  write(9,*)'lcom not set properly. Must be 0 or 1.'
  write(9,*)''
  write(9,*)'Simulation stopped.'
  stop
endif

if ((opt.ne.0).and.(opt.ne.1)) then
  write(9,*)'opt not set properly. Must be 0 or 1.'
  write(9,*)''
  write(9,*)'Simulation stopped.'
  stop
endif

if ((idef.gt.4).or.(idef.lt.0)) then
  write(9,*)'idef not set properly. Must be between 0 and 4.'
  write(9,*)''
  write(9,*)'Simulation stopped.'
  stop
endif

return
end
```